REPUBLIQUE ALGÉRIENNE DÉMOCRATIQUE ET POPULAIRE

Ministère de l'enseignement supérieur et de la recherche scientifique

UNIVERSITÉ AMAR TELIDJI LAGHOUAT

Faculté de technologie-Département d'Électronique

MEMOIRE DE MAGISTER

Présenté en vue de l'obtention du diplôme de magister en génie électrique
Option : Signaux et Télécommunication

Thème

Design of Metamaterial Agile Radiation Pattern Microstrip Antenna

Présenté par

Mr. Bensafieddine Djalal Eddine
Ingénieur d'état en électronique

Devant le jury composé de:

Mr. Ibn Khaldoun LEFKAIER	Professeur à l'Université de Laghouat	Président
Mr. Mouloud BOUZOUAD	Professeur à l'Université de Laghouat	Encadreur
Mr. Abdelkrim BENABDELKRIM	Maitre Assistant à l'Université de Laghouat	Co-encadreur
Mr. Tarek FORTAKI	Professeur à l'Université de Batna	Examinateur
Mr. Bachir BENTRIA	Professeur à l'Université de Laghouat	Examinateur

Année universitaire 2014-2015

ملخص

من بين تطبيقات مافوق المواد "metamaterial" الأكثر أهمية في مجال الهوائيات يمكن أن نذكر تحسين أداء الهوائي والتقليص من حجمه. ومع ذلك، تبقى السيطرة والتحكم على خصائص الهوائي من الأهداف رئيسية لإستخدمات مافوق المواد في هذا المجال. الغاية من هذا العمل هو تصميم هوائيات مرنة "agile" ، والتي يمكننا التحكم في خصائصها بإستعمال نظام تحكم خارجي نشط، مما يجعل أجهزة الاتصالات أكثر ذكاء و طواعية. كان إهتمامنا في هذه الدراسة بمرونة الهوائي و خاصةً مرونة مخطط إشعاعه. الغاية من ذلك هي التحكم في شكل مخطط إشعاع الهوائي بواسطة عدسة ما فوق مادية مرنة. لهذا الغرض قمنا بتصميم خلية ما فوق مادية مرنة تمتاز بسلوكيين مختلفين حسب الطلب: سلوك مادة معامل انكسارها قريب من الصفر و سلوك مادة معامل انكسارها أكبر من الوحدة. نظام التحكم الخارجي يمكننا من برمجة سلوك السطح الما فوق مادي من خلال التحكم في كل خلية على حدى. تستخدم هذه العدسة المرنة لتعزيز كسب الهوائي والسيطرة على نمط مخطط إشعاعه. أفضل النتائج التي تحصلنا عليها كانت بإستعمال عدسة ما فوق مادية مرنة كروية الشكل. حيث حققنا كسب أكبر من 12 ديسيبل مع تغير في زاوية توجيه مخطط الإشعاع ما بين -33° إلى 33° في المستوي E و-37° من إلى 37° في المستوي H. و تحصلنا أيضا على عرض نطاق الإشعاع الرئيسي يقدر ب 23° في المستوي E و19° في المستوي H.

الكلمات المفتاحية : مافوق المواد، مرونة مافوق المواد ، هوائيات مرنة ،التجانس.

Abstract

Among the most important metamaterial applications in the antenna field we can cite the antenna performances enhancement and size reduction. However, antenna characteristics control remains a major objective of metamaterial use in the antenna field. The goal is to design agile antennas, of which it is possible to change the characteristic using an external active control system. This makes the telecommunications systems more flexible. We are interested in this work, with the antenna agility and specially the radiation pattern agility. The aim is to control the antenna radiation pattern using an agile metamaterial lens. This agile lens is based on an agile metamaterial. For this purpose we design an agile unit cell which can flips between two different behaviors. The first one corresponds to an effective medium with a refractive index close to zero and the second one corresponds to an effective medium having a refractive index greater than unity. The external control system, allows us to program the metamaterial behavior by acting on each unit cell individually. This agile lens is used to enhance a microstrip antenna gain and control its radiation pattern. The best enhancements are obtained with the spherical cap metamaterial lens. It is optimized to obtain a realized gain up to 12 dB and radiation main lobe rotation from -33° to 33° in the E-plane and from -37° to 37° in the H-plane. We obtain also a main lobe beamwidth of 23° in the E-plane and 19° in the H-plane.

Key words: Metamaterial, Agile Metamaterial, Microstrip Antenna agility, Homogenization.

Résumé

Parmi les applications les plus importantes des métamatériaux dans le domaine antennaire, on peut citer l'amélioration des performances et la réduction de la taille. L'objectif est de concevoir des antennes agiles, dont il est possible de changer les caractéristiques en utilisant un système de contrôle actif externe. Ce qui rend les systèmes de télécommunications plus flexibles. Nous nous sommes intéressés dans ce travail, par l'agilité des antennes et plus précisément par l'agilité du diagramme de rayonnement. Le but est de contrôler le diagramme de rayonnement d'une antenne patch en utilisant une lentille métamatériau agile. Cette lentille agile est basée sur un métamatériau agile. Dans ce but, nous avons conçu une cellule agile qui peut basculer entre deux comportements différents. La première correspond à un avec un indice de réfraction proche de zéro et le second correspond à un milieu effectif à indice de réfraction supérieur à l'unité. Le système de contrôle externe, nous permet de programmer leur comportement en agissant individuellement sur chaque cellule élémentaire. Cette lentille agile est utilisée pour améliorer le gain de l'antenne microruban et de contrôler son diagramme de rayonnement. Les meilleurs résultats sont obtenus avec la lentille en forme de calotte sphérique. Elle a été optimisée pour obtenir un gain allant jusqu'à 12 dB et une rotation du lobe principale du diagramme de rayonnement allant de -33° à 33° dans le plan E et de -37 ° à 37 ° dans le plan H avec un angle d'ouverture de 23° dans le plan E et 19° dans le plan H.

Mots clés : Métamatériaux, métamatériaux Agile, Antenne patch agile, homogénéisation.

Acknowledgements

First I would like to express my gratitude to my supervisor Prof. Mouloud BOUZOUAD for his support and continuous encouragement throughout my research. I really appreciate his guidance, insights and suggestions on this research, which will be a valuable experience for my future career.

I would also like to thank Dr-Abdelkrim BENABDELKRIM for guiding my research for the past several years.

I gratefully acknowledge my thesis committee members Prof. Ibn Khaldoun LEFKAIER Prof. Tarek FORTAKI, and Prof. Bachir BENTRIA for their remarks and suggestions on my dissertation.

I also pass my sincere thanks to all my current technical colleagues and Metamaterials team at Telecommunications signal and system laboratory for their generous helps and constructive discussions.

The most and for most, my special appreciations go to my family for their extensive encouragements and continuous supports during this past three years, which gave me all the strength needed to successfully finish my magister. I deeply indebted to my mother and father for their understanding and all their unforgettable supports during whole of my career. I also express my sincere thanks to my brother for his encouragement and helps.

Bensafieddine DjalalEddine

Table of contents

Chapter 1

Chapter 2

Chapter 3

Chapter 4

List of figures

List of tables

Introduction

The advance of the wireless telecommunications networks ought to develop smart antenna systems. For a best quality of service, it is necessary to steer and control the radiation pattern of the antennas in desired directions.

This project examines the possibility of enhancement and controlling the antenna gain radiation pattern using agile metamaterial lens which is composed of two regions, the first one forms a focusing zone (FZ) and the second one, the lens body (host medium). The agile metamaterial is based on an agile metamaterial unit cell, which have two different behaviors .The first one where the unit cell is a disconnected cross, in which case metamaterial behaves like an effective medium with a refraction index n_1 higher than the unity. For the second one, where the unit cell is a connected cross and the metamaterial behaves like an effective medium with a positive and close to zero refraction index n_2.

The basic idea is to replace the planar agile metamaterial grid by a spherical one which envelops the antenna as a spherical cap shape. The refraction index (n_1 or n_2), the size, the shape and position of the FZ can be programmed by acting on the switching devices (state ON or OFF) of every unit cell. Modifying the FZ parameters (size, shape, position, and refraction index), allows us to control the antenna radiation pattern properties like the main lobe direction (pointing angle) and the beamwidth in both E and H-Planes of the radiation pattern.

Chapter one deals with the definition of metamaterials and their applications. The second chapter is devoted to the effective parameters extraction of homogenized metamaterials. It presents a brief overview of the homogenization of composite materials, and the different methods used for the extraction of the metamaterial effective electromagnetic constitutive parameters (dielectric permittivity magnetic permeability, and refraction index) using a finite element method based commercial simulation code. Chapter 3 concerns the agile antennas concept. Three types of antenna agility are treated: Frequency agility antennas, for which we can modify the antenna operating frequency, radiation pattern agility, for which we can change the antenna radiation pattern characteristics (pointing direction, main lobe beamwidth, etc.), and polarization agility when the antenna polarization can be changed dynamically.

Finally, the chapter 4 is centered on the control of the radiation pattern of a microstrip antenna, using an agile metamaterial lens. This later is constituted by a single/double layer planar lens or a spherical cap shape lens. The agile metamaterial lens is composed of two regions: the first one is the lens body and is made of connected cross type metamaterial. The

second one is made of disconnected cross type metamaterial and constitutes a focusing zone (FZ). This later can be situated anywhere in the lens body and can have an arbitrary shape. By acting on the unit cells switches one can modify the FZ parameters and then control the patch antenna's radiation-pattern parameters such as main-lobe beamwidth and pointing angle and can enhance the antenna gain.

1. Generalities

1.1 Introduction

There have been increasing interests in metamaterials in the past 10 years in the scientific communities. However, metamaterials are sometimes regarded as negative refractive index materials by a lot of people including researchers. In fact, the rapid development in this exciting area has shown that metamaterials are far beyond negative refractive index materials. In this chapter, we will clarify what metamaterial is and report the recent progress on metamaterials. We also summarize the potential applications in areas such as sub-wavelength imaging, antenna design, invisibility cloak, and biosensing.

1.2 Definition of metamaterials

Metamaterials are man-made materials, composed of artificially structured unit cells that are designed of conventional materials and usually (but not necessarily) arranged in periodic fashion [1]. The matter is constituted of atoms and molecules see figure 1-1, and is seen by the electromagnetic waves as electric and magnetic dipolar distributions, which are the microscopic sources of the polarization and magnetization phenomenon. Generally, we can cite three microscopic mechanisms of polarization. The first one is electronic polarization. It is related to the modification of the internal charges repartition of each atom or ion. It is constantly present whatever the state of the considered material. The second one is the atomic or ionic polarization. It concerns the displacements of atoms or ions compared to their equilibrium positions in the crystalline edifice where they belong. The third one is the orientation polarization. It arises when the atomic or molecular dipole moments are oriented under an electric field action. The origin of the microscopic magnetization is the magnetic moments of the microscopic electric currents resulting from the motion and spin of the charged particles present in atoms.

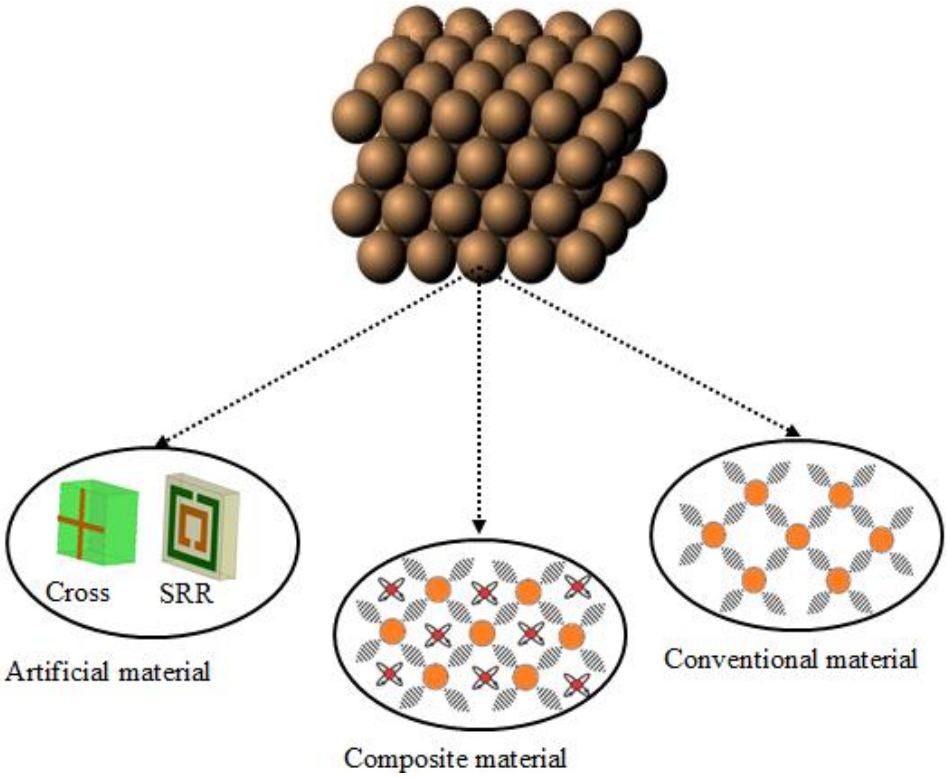

Figure 1-1: Unit cell types arranged in space compared to atomic scale in conventional materials.

1.3 Historical points for Metamaterials

The word ‘metamaterial’ first appeared in literature in 2000 when Smith et al. published their seminal paper on a structured material with simultaneously negative permeability and permittivity at microwave frequency. Other sources suggest that the term ‘metamaterial’ was first coined by Rodger M. Walser, a physics professor at the University of Texas in 1999.

There are three fundamental papers that should be mentioned in metamaterial history. The first one is Veselago’s paper on left handed materials [1]. This paper studied the unusual phenomena to be expected in a hypothetical left handed substance in which the field vectors $\vec{E}$, $\vec{H}$ and the wave vector $\vec{k}$ form a left handed system. The paper also explicitly presented the required material parameters to achieve the material simultaneously negative values of permittivity and permeability. The second one consists of the first experimental demonstration of a Veselago medium by Smith et al. which represents a passage from a theoretical prediction to an experimental validation [2]. The third paper is Pendry’s work on a perfect lens which represents the initial attempt to fill the gap between novel metamaterials and exciting applications[3].

1.4 Metamaterial characteristics

The structural units of metamaterials can be tailored in shape, size, and the composition. The inclusions composition and morphology can be designed and artificially tuned, and placed in a predetermined manner to achieve prescribed functionalities.

The dependence of metamaterial properties on the unit cell architecture provides great flexibility to control metamaterials electromagnetic responses which are described by the electric permittivity and the magnetic permeability. So, by varying the different unit cell geometry parameters, we can create an agile metamaterial which electromagnetic response is unavailable in nature and can be tailored in practice to a reach desired profile. Metamaterial tailoring is one of the important advantages of metamaterials.

1.5 Metamaterial classes

Permittivity ε and permeability μ are two parameters used to characterize the electric and magnetic properties of materials interacting with electromagnetic fields.

The permittivity is a measure of how much a medium changes to absorb electrical energy when it is subjected to an electric field [4-5]. It is defined as the ratio of the electric displacement $\vec{D}$ and the electric field $\vec{E}$. The common term dielectric constant is the ratio of permittivity of the material to that of free space ε_0. It is also termed as the relative permittivity. The permeability is also defined as the ratio of the magnetic induction $\vec{H}$ and magnetic field $\vec{B}$. The free-space permeability μ_0 is approximately 1.257×10^{-6} H/m. Recently, Ziolkowski [6-7] has categorized metamaterials by their constitutive parameters as shown in figure 1-2. Most of the materials in nature have positive permittivity and permeability, and hence, they are referred to as ‘double-positive’ (DPS’ medias or right-handed materials (RHM). In contrast, if both of these quantities are negative, these medias are called ‘double-negative’ (DNG) and are also referred to as left-handed materials (LHM). Finally, materials with one negative parameter are named ‘single-negative’ (SNG) and are further classified into two subcategories, namely, ‘epsilon-negative’ (ENG) an ‘mu-negative’ (MNG). Interestingly, natural materials such as cold plasma and silver exhibit negative permittivities at microwave and optical frequencies, respectively, and ferromagnetic materials exhibit a negative permeability behavior in the VHF and UHF regimes [6]. However, to date, no materials that exhibit simultaneous negative permittivity and permeability have been found in nature, and hence they must be produced artificially.

The first comprehensive review of the history of negative refraction and metamaterials was given by Moroz [8]. He indicated that some of metamaterial research started long before Veselago's work and went back to as far as 1905, when Lamb [9] suggested the existence of backward waves, which are associated with waves in which the phase propagates in a direction opposite to that of the energy flow. Moroz's on-line article first appeared in 2003, tracing the roots of research on backward waves, negative refraction, and LHM. Only recently, Veselago and Narimanov [10], Shivola [11], and Shamonina [12] have linked LHMs, and more generally metamaterials, to the earlier works.

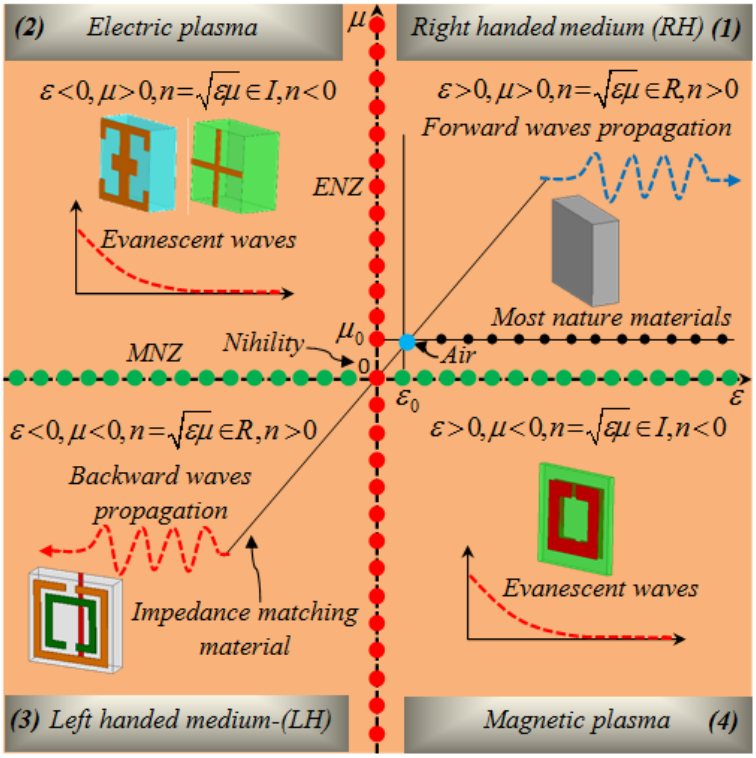

Figure 1-2: Metamaterial classes.

From figure 1-2 four possible quadrants can be taken:

- Quadrant 1: double-positive media or right-handed materials $\varepsilon > 0$ and $\mu > 0$.

This quadrant represents (RHM), which support the forward propagating waves. It is well know that the constitutive parameters ε and μ are related to the refractive index *n* by:

$$n = \sqrt{\varepsilon_r \mu_r} \qquad (1\text{-}1)$$

We have $\varepsilon > 0 \Rightarrow \varepsilon = |\varepsilon|$ and $\mu > 0 \Rightarrow \mu = |\mu|$.

From (1-1) we obtain:

$$n = \sqrt{|\varepsilon_r||\mu_r|} = +\sqrt{|\varepsilon_r||\mu_r|} \quad (1\text{-}2)$$

$$k = \omega\sqrt{|\varepsilon_r||\mu_r|} = k_0 n \quad (1\text{-}3)$$

$$\gamma = jk = j\omega\sqrt{|\varepsilon_r||\mu_r|} = \alpha + j\beta \quad (1\text{-}4)$$

$$\gamma = j\omega\sqrt{|\varepsilon_r||\mu_r|} = \alpha + j\beta \Rightarrow \alpha = 0 \text{ and } \beta = \omega\sqrt{|\varepsilon_r||\mu_r|} = \gamma \quad (1\text{-}5)$$

We have clearly propagating waves (propagating medium α = 0). The expression of a propagating plane wave in such media is written as:

$$\vec{E} = \overrightarrow{E_0}\exp(-jkz) = \overrightarrow{E_0}\exp(-jnk_0 z) \quad (1\text{-}6)$$

- Quadrant 2: epsilon-negative medium or electric plasma $\varepsilon < 0, \mu > 0$

In certain frequency regimes many plasmas exhibit this characteristic. For example, noble metals (e.g., silver, gold) behave in this manner in the infrared (IR) and visible frequency domains. This quadrant supports evanescent waves.

We have $\varepsilon < 0 \Rightarrow \varepsilon = -|\varepsilon|$ and $\mu > 0 \Rightarrow \mu = |\mu|$.

From (1-1) we have:

$$n = \sqrt{-|\varepsilon_r||\mu_r|} = j\sqrt{|\varepsilon_r||\mu_r|} \quad (1\text{-}7)$$

$$k = \omega j\sqrt{|\varepsilon_r||\mu_r|} = k_0 n \quad (1\text{-}8)$$

$$\gamma = jk = j\omega j\sqrt{|\varepsilon_r||\mu_r|} = \alpha + j\beta \quad (1\text{-}9)$$

$$\gamma = j\omega j\sqrt{|\varepsilon_r||\mu_r|} = \alpha + j\beta \Rightarrow \beta = 0 \text{ and } \alpha = -\omega\sqrt{|\varepsilon_r||\mu_r|} < 0 \quad (1\text{-}10)$$

And then from (1-7) the expression of a propagating plane wave in such media is written as:

$$\vec{E} = \overrightarrow{E_0}\exp(-\alpha z) \quad (1\text{-}11)$$

Since α is negative the term $\exp(-\alpha z)$ is divergente when $z \to +\infty$. The evanescent waves are amplified in an ENG media.

- Quadrant 3:double-negative media or left-handed materials $\varepsilon < 0, \mu < 0$

This third case was proposed by Veselago in 1968, supporting the backward propagating waves. We have:

$$\varepsilon_r < 0 \Rightarrow \varepsilon_r = -|\varepsilon_r| \text{ and } \mu_r < 0 \Rightarrow \mu_r = -|\mu_r|$$

From equation (1-1) we obtain:

$$n = \sqrt{-|\varepsilon_r| \times -|\mu_r|} = \sqrt{|\varepsilon_r||\mu_r|} \quad (1\text{-}12)$$

$$k = \omega\sqrt{\varepsilon_r \mu_r} = \omega\sqrt{|\varepsilon_r||\mu_r|} \quad (1\text{-}13)$$

Comparing equations (1-9) and (1-13), then we obtain :

$$\alpha = 0 \text{ and } \beta = \omega\sqrt{|\varepsilon_r||\mu_r|} = \gamma \quad (1\text{-}14)$$

Then, the expression of the electric field corresponds to the propagating waves and can be written as:

$$\vec{E} = \overrightarrow{E_0}\exp(-jkz) = \overrightarrow{E_0}\exp(-jkn_0 z) \quad (1\text{-}15)$$

- Quadrant 4: mu-negative medium or magnetic plasma $\varepsilon > 0, \mu < 0$.

In certain frequency regimes some gyrotropic materials exhibit this characteristic. This quadrant supports also evanescent waves.

$\varepsilon_r > 0 \Rightarrow \varepsilon_r = |\varepsilon_r|$ and $\mu_r < 0 \Rightarrow \mu_r = -|\mu_r|$

From equation (1-1):

$$n = \sqrt{-|\varepsilon_r||\mu_r|} = j\sqrt{|\varepsilon_r||\mu_r|} \quad (1\text{-}16)$$

$$k = \omega\sqrt{\varepsilon_r \mu_r} = j\omega\sqrt{|\varepsilon_r||\mu_r|} \quad (1\text{-}17)$$

Comparing equations (1-9) and (1-17), we find

$$\beta = 0 \text{ and } \alpha = -\omega\sqrt{|\varepsilon_r||\mu_r|} = \gamma \quad (1\text{-}18)$$

From equation (1-6), the expression of the propagating plane wave in such medium is :

$$\vec{E} = \overrightarrow{E_0}\exp(-\alpha z) \quad (1\text{-}19)$$

Metamaterials have much broader scope than LHM, as shown in figure 1-2. In the $\varepsilon - \mu$ domain, there are several special lines and points indicating special material properties. For example, the point $\mu = -\mu_0$ and $\varepsilon = -\varepsilon_0$ represents an antiair in the LHM region, which will produce a perfect lens; the point $\mu = 0$ and $\varepsilon = 0$ represents a nihility, which can yield a perfect tunneling effect; the line $\mu = -\varepsilon$ in both RHM and LHM regions represents impedance-matching materials, which have perfect impedance matching with air, resulting no reflections. Also, the vicinity of $\mu = 0$ is called as μ near zero (MNZ) material, and the

vicinity of $\varepsilon = 0$ is called as ε-near zero (ENZ) material, which has special properties applied in in perfect lens [33].

1.6 Artificial Dielectrics

Artificial dielectrics, the first known metamaterials, usually consist of artificially created molecules: dielectric or metallic inclusions of a certain shape [13]. These • molecules can be distributed and oriented in space see figure 1-3, either in a regular lattice or in a random manner.

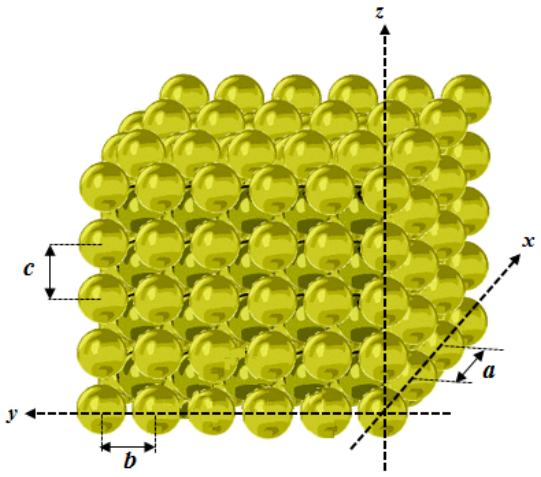

Figure 1-3: The geometry of a generic artificial dielectric.

The dimensions of the molecules and characteristic distances between neighboring ones are assumed to be very small, as compared to the wavelength.

The concept of artificial dielectrics was perhaps first introduced in [14], who used it to design low-weight dielectric lenses at microwave frequencies. The artificial dielectrics also find applications where we need to use a high-permittivity material, such as a titanate with $\varepsilon_r = 90$. Since these materials are usually expensive, an alternative is to use metallic inclusions of various shapes with sizes that are small compared to the wavelength to artificially produce a high-permittivity material, which is both low-cost and lightweight [15]. A very interesting example of artificial dielectrics is the wire medium [16-17], which has been known since 1950s. It is formed by a regular lattice of conducting wires.

1.7 The microscopic view of metal thin wire

Based on the effective medium theory, the metamaterials can be characterized by effective electric permittivity and magnetic permeability. Pendry realized the artificially electric plasma using a metallic wire whose permittivity is negative [18]. And the artificially

magnetic plasma whose permeability is negative [19]. Metamaterials open a door to realize all possible material properties (tailoring desired electromagnetic properties) by designing different unit cells and using different substrate materials [20]. Among the various, usual and unusual material parameters provided by metamaterials ($\varepsilon_{eff} > 0$, $\mu_{eff} > 0$, $\varepsilon_{eff} < 0$, $\mu_{eff} < 0$, ≈ 0 , μ_{eff} and $n \approx 0$ ...) they can lead to many interesting phenomena.

The metal thin wire medium, whose unit cell is presented in figure 1-4 (b), exhibits a plasmonic type permittivity frequency function of the form [22]:

$$\varepsilon_{reff}(\omega) = 1 - \frac{\omega_{pe}^2}{\omega^2 - j\Gamma_e\omega} \quad (1\text{-}20)$$

Equation (1-20) in real and imaginary parts becomes:

$$\varepsilon_{reff}(\omega)\ 1 - \frac{\omega_{pe}^2}{\omega^2 + \Gamma_e^2} + j\frac{\Gamma_e\omega_{pe}^2}{\omega(\omega^2 + \Gamma_e)} \quad (1\text{-}21)$$

The real and imaginary parts are plotted in figure 1-4 (c).

Analytic procedure is detailed in [21] from which the Drude parameters ω_{pe} and Γ_e are expressed in function of the geometric dimensions (the period a and the radius of the wire r) as:

$$\omega_{pe} = \sqrt{\frac{2\pi c^2}{a^2 \ln(a/r)}} \quad (1\text{-}22)$$

$$\Gamma_e = \varepsilon_0\left(\frac{a\omega_{pe}}{\pi\sigma r^2}\right) \quad (1\text{-}23)$$

Where c is the speed of light and σ the conductivity of the metal. We observe from (1-21) that $Re(\varepsilon_{reff}) < 0$ for $\omega < \sqrt{\omega_{pe}^2 - \Gamma_e^2}$.

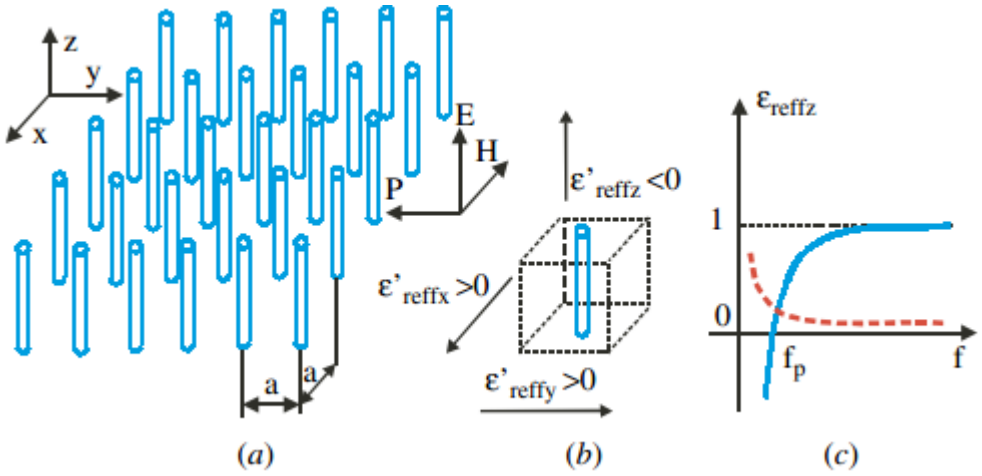

Figure 1-4: (a) 2D thin wires arrangement, (b) Thin wire unit cell, and. (c) Real (solid blue) and imaginary (dashed red) parts of effective permittivity of metamaterial (a) [23].

1.8 Artificial Magnetic Materials

Artificial magnetic materials are typically synthesized by using resonant elements, such as split-ring resonators or Swiss rolls as shown in figure 1-5. The split-ring resonators are more widely used than the Swiss rolls since they can be manufactured using printed circuit technology. Artificial magnetic materials were known as far back as the early 1950s, and a book by Schelkunoff and Friis [24] provides expressions that can be used to calculate the magnetic flux of a split metallic wire loaded with a small capacitor, formed by a pair of parallel metallic plates. Schneider et al in [25], used a split metallic tube to produce an NMR probe, and, in [26] Hardy proposed a Swiss roll resonator to achieve magnetic resonance at 200-2000 MHz. Kostin et al in [27], has synthesized an artificial magnetic material with frequency dependent positive permeability by using double circular ring resonators.

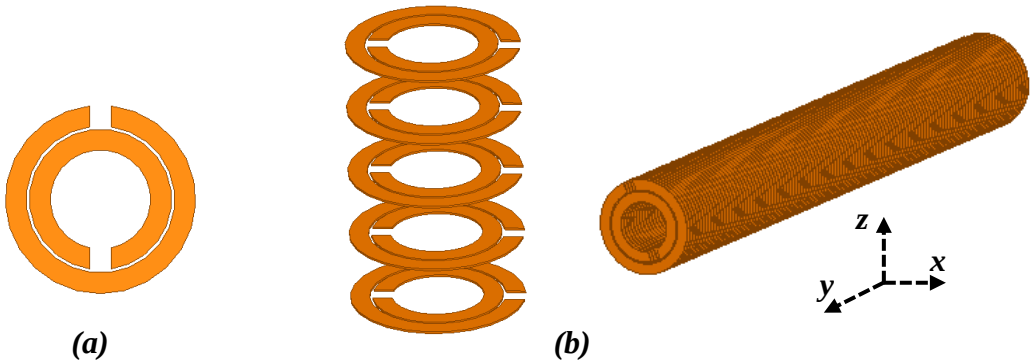

Figure 1-5: (a)- Split-ring resonator SRR(b)- Swiss roll resonator.

An artificial magnetic material, which is formed by split-ring resonators, possesses negative permeability within a frequency band (bandwidth is typically narrow) near the

resonant frequency of the single split-ring resonator; it is widely used to create LHMs. Metallic waveguides filled with such artificial magnetic materials support guided waves at frequencies below the cutoff frequency of hollow waveguides; hence such guides are also referred to as the sub-wavelength waveguides [28]. This effect can be used for miniaturization of guided wave structures [29], though they do introduce additional losses owing to the presence of high circulating currents in the inclusions when they are resonant.

1.9 Microscopic view of split ring resonator (SRR)

The SRR in figure 1-6-(b) exhibits a permeability frequency response of the form [22]:

$$\mu_{reff}(\omega) = 1 - \frac{\omega_{pm}^2}{\omega^2 - \omega_{0m}^2 + j\Gamma_m\omega} \quad (1\text{-}24)$$

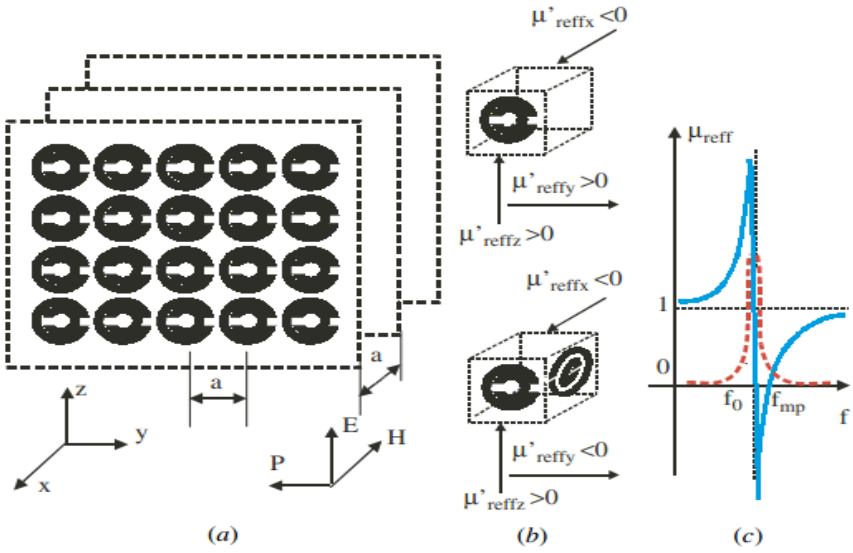

Figure 1-6:(a).Array of SRR.(b).SRR of 1D and 2D unit cells (c).Re(μ_{reff})(solid blue), Im(μ_{eff}) (dashed red) [11].

Equation (1-24) is divided in real and imaginary parts and presented in figure 1-6-(c):

$$\mu_{reff}(\omega) = 1 - \frac{F(\omega^2 - \omega_{0m}^2)}{(\omega^2 - \omega_{0m}^2) + (\omega\Gamma_m)^2} + j\frac{\Gamma_m\omega_{pm}^2}{(\omega^2 - \omega_{0m}^2) + (\omega\Gamma_m)^2} \quad (1\text{-}25)$$

Lorentz parameters are calculated in detail manner in [18]:

$$F = \sqrt{\pi\left(\frac{r}{a}\right)^2} \quad (1\text{-}26)$$

$$\omega_{0m} = c\sqrt{\frac{3a}{\pi \ln 2\left(2wr^3/\delta\right)}} \quad (1\text{-}27)$$

Where r, w and δ are the inner radius for the smaller ring, width of the ring and radial spacing between the rings.

We have also:

$$\Gamma_m = \frac{2aR'}{r\mu_0} \qquad (1\text{-}28)$$

R' is the metal resistance per unit length.

We observe from (1-25) that $\mu_{reff} < 0$ for $\omega_{0m} < \omega < \frac{\omega_{0m}}{\sqrt{1-F}} = \omega_{pm}$

1.10 Metamaterial applications

Due to the exciting and unusual features, metamaterials have found and are finding a lot of applications. Metamaterials can impact on telecommunications, sensing and susceptibility as shown in figure 1-7 , across all wave types, but especially electromagnetic and acoustic.

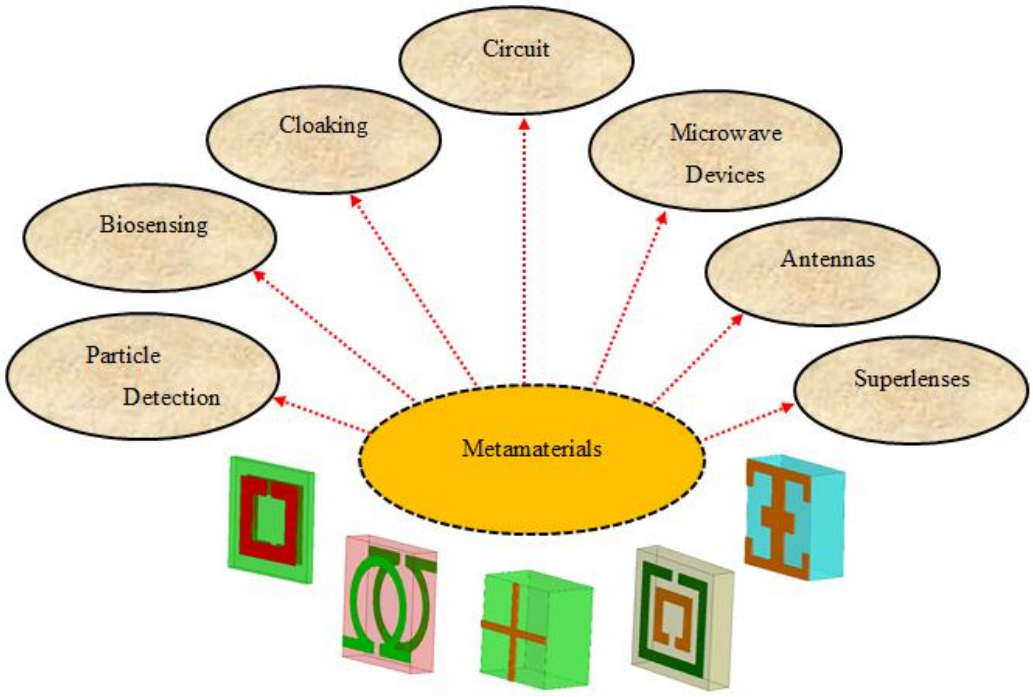

Figure 1-7: potential applications.

1.10.1 Superlenses

For left handed metamaterial, the most attractive feature is the superlens which can be widely used in super resolution medical imaging, optical imaging, and nondestructive detections [30]. A super lens or perfect lens is a lens which uses metamaterials to go beyond the diffraction limit [31]. The diffraction limit is an inherent limitation in conventional optical

devises or lenses. In 2000, a type of lens was proposed, consisting of a metamaterial that compensates for wave decay and reconstructs images in the near field and most importantly the both propagating and evanescent waves contribute to the resolution of the image. In 2004, the first superlens with a negative refractive index provided resolution three times better than the diffraction limits and was demonstrated at microwave frequencies. In 2005, the first near field superlens which exceeded the diffraction limit was demonstrated [32].The higher focusing resolution will be provided by flat LHM lens if compared to convex dielectric lens and elliptical reflector focusing system. The LHM lens has the potential to acquire higher imaging resolution and easy in-depth scanning, which will simplify the detection system design [32].

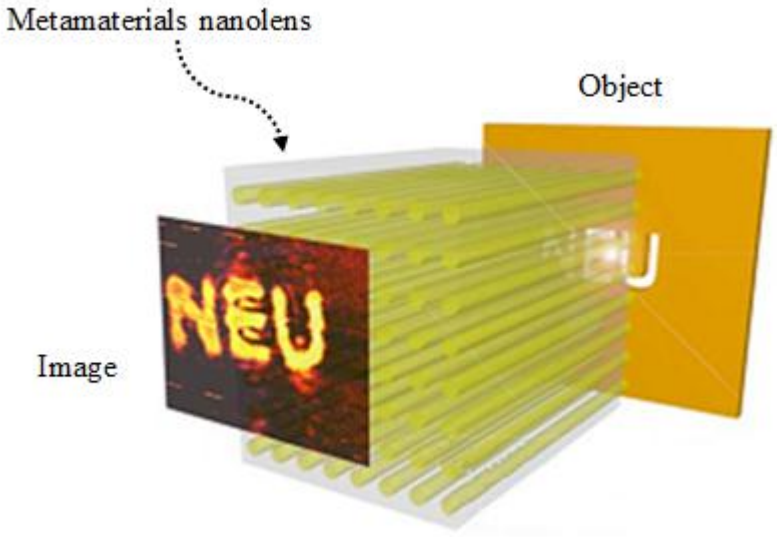

Figure 1-8:Super-resolution imaging using a three-dimensional metamaterials nanolens.

For example in biological domain, microwaves are used to destroy or ablate diseased soft-tissue by heating it to a temperature that causes cell death. This procedure is called hyperthermia. The generator produces microwave energy which is transmitted through the antennas into the patient. Elevating the temperature of tumor cells causes cell membrane damage, which leads to the destruction of the cancer cells. Hyperthermia treatment of cancer requires directing a carefully controlled dose of heat to the cancerous tumor and surrounding body tissue. The most prominent property of metamaterial lens is the ability of negative-refractive index (NRI) to focus the electromagnetic field of a source. Hence it can generate appropriate focusing spot in biological tissue as required in microwave hyperthermia treatment.

1.10.2 Antennas

Metamaterial antennas are a class of antennas which use metamaterials to enhance or increase the antenna performances. The metamaterial could enhance the radiated power of an antenna. Materials with negative magnetic permeability could possibly allow for properties such as an electrically small antenna size, high directivity, and tunable operational frequency. Furthermore, metamaterial based antennas can demonstrate improved efficiency and high bandwidth performance.

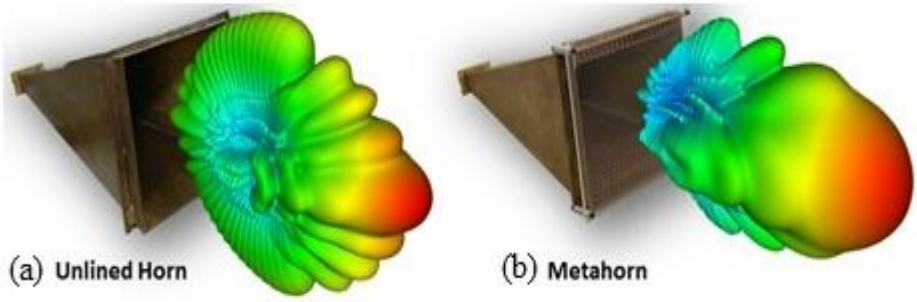

Figure 1-9: rectangular horn antenna (a)-alone (b)-with metamaterial.

Metamaterials employed in the ground plane surrounding antennas offers improved isolation between radio frequency or microwave channels of (multiple-input multiple-output) (MIMO) antenna arrays. Metamaterial, high-impedance ground planes can also be used to improve the radiation efficiency, and axial radio performance of low-profile antennas located close to the ground plane surface.

Metamaterials have also been used to increase the beam scanning range by using both the forward and backward waves in leaky wave antennas. Various metamaterial antenna systems can be employed to support surveillance sensors, communication links, navigation systems, command and control systems [33].

The gradient refractive index metamaterials are also utilized to produce beam-bending lens and beam-focusing lenses. Based on such properties, high-gain and broadband gradient planar lens antennas and Luneberg-like lens antennas have been proposed and realized [33]. The Industrial, Scientific and Medical (ISM) radio bands are portions of the radio spectrum reserved internationally for the use of radio frequency (RF) energy for industrial, scientific and medical purposes other than communications.

1.10.3 Microwave devices

The waveguided or planar metamaterials which are composed of complimentary structures like CSRR have been used to design microwave components like filters, power dividers, and phase shifters. Narrowband and broadband polarizers have been realized using three-dimensional (3D) anisotropic metamaterials [35].

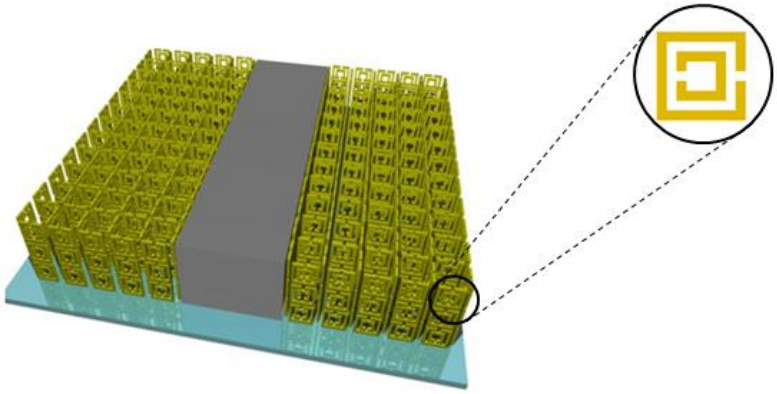

Figure 1-10: planar waveguides with double SRR metamaterials.

Superconducting metamaterials have been achieved in addition to superconducting split rings and wires. They have been utilized to realize a number of unique applications. The combination of left-handed and right-handed propagation media creates opportunities for new types of resonant structures. By laminating two materials with opposite sense of phase it is possible to create a new class of resonant structures [34]. For example, two flat conducting plates separated by a sandwich of left-handed and right handed metamaterials constitutes such a new resonator. A wave propagating in the direction normal to the plates will suffer a combination of forward and reverse phase windings before reaching the other reflecting boundary. Under these conditions the wave could undergo a net phase shift of 0 radians and still create a resonance condition. The net phase shift could also be a positive or negative multiple of 2π radians as well, each creating a resonant condition. The result is an ultra-compact resonator whose overall dimension is no longer constrained by the wavelength of the resonant wave.

Superconductors are particularly attractive for use in ultra-compact resonators and showed resonances with indices between +2 and -6, including zero, over the broad frequency range from about 5 to 24 GHz [36]. Quality factors of the negative order resonances were on the order of 3000 at 30 K, while those for positive order resonances were below 400.

1.10.4 Circuit Applications

SRR and CSRR-based transmission lines are useful for device miniaturization, and find their applications in microwave passive components such as impedance inverters, power dividers [37], couplers, and filters. SRRs are also useful particles in many other applications such as magneto inductive and electro inductive wave components [38] frequency selective surfaces [39].

1.10.5 Cloaking

Cloaking devices are advanced stealth technologies that can make objects partially or wholly invisible to some portions of the electromagnetic spectrum. Generally speaking, there are several major approaches to render objects invisible. For example, Alu and Engheta [40] proposed to use plasmonic coatings to cancel the dipolar scattering. But this technique is limited to the sub-wavelength scale of the object, and the coating depends on the geometry and material parameters of the object. Milton and Nicorovici [41] discovered that using a metamaterial coating would cloak polarizable line dipoles. But the coating is affected by the objects placed inside. Leonhardt [42] and independently Pendry, Schurig and Smith [43] discovered a coordinate transformation mechanism for electromagnetic cloaking.

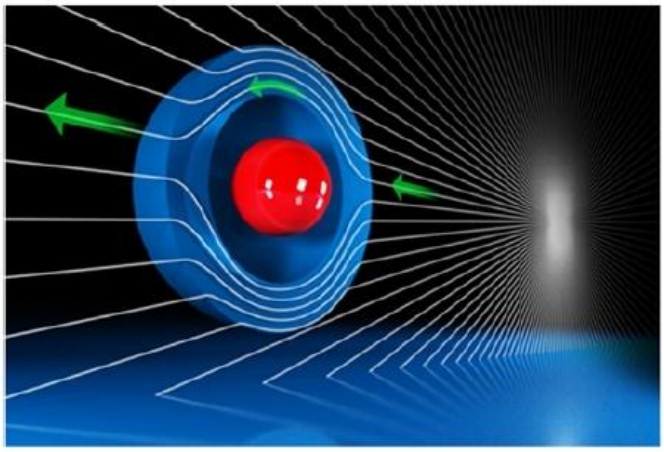

Figure 1-11: Invisibility cloaks.

Their mechanism was quite similar to that of Greenleaf et al. [44-45] introduced for conductivity. Their main idea is to guide electromagnetic wave around the cloaked region, and many later work has adopted this technique. In May 2006, the first full wave numerical simulations on cylindrical cloaking was carried out by Cummer et al. [46]. A few months later, the first experiment of such a cloak at microwave frequencies was successfully demonstrated by Schuriget al. [47], where the cloak surrounding a 25-mm-radius Cu cylinder

was measured. After 2006, numerous studies have been devoted to cloaking, mainly inspired by [46]. For example, in 2008, Liang et al [48] performed a time-dependent simulation for the cylindrical cloak using finite-difference time-domain method.

1.10.6 Biosensing

Another potential application field of metamaterials is on biosensing. Conventional biosensors (such as those based on electro-mechanical transduction, fluorescence, nanomaterials, and surface plasmon resonance) often involve labor-intensive sample preparation and very sophisticated equipment.

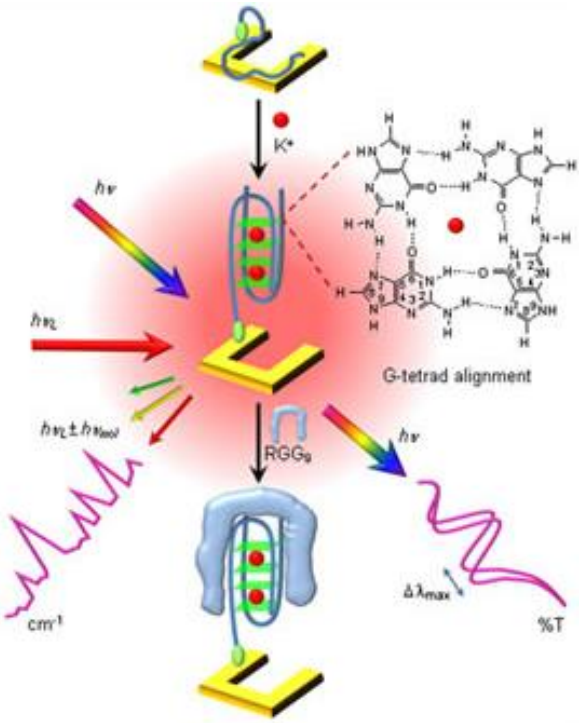

Figure 1-12: Schematic illustration of Vis-NIR SRR metamaterials as dual transducing mode nanosensor for the detection and identification of biomolecules.

In recent years, researchers have proposed to use metamaterials as candidates for detection of highly sensitive chemical, biochemical and biological analytes. For example, Lee et al. [49] studied the possibility of using split-ring resonators (SRRs) for biosensors. The basic principle is based on the fact that SRR can be considered to be a simple LC circuit with a response frequency of $f = 1/2\pi\sqrt{LC}$, which shows that the resonant frequency varies in terms of the changes in the inductance L and/or capacitance C. Hence the resonant frequency of the SRR shall be shifted before and after the introduction of biomaterials. Planar metamaterials were proposed to serve as thin-film sensors recently by O'Hara et al [50]. They

found that a resonant frequency response can be tuned through metamaterial designs. Though their metamaterial design can only detect thin films having a thickness less than 100 nm, their work presents a promising utlook for THz sensing technology.

1.10.7 Particle Detection

It is well known that when charged particles move in a medium with velocity larger than c/n (the phase velocity of light in the medium), Cherenkov radiation (CR) is emitted. Recall that c is the speed of light in vacuum, and n is the index of refraction of the medium. An example of CR is the blue glow seen in a nuclear reactor. Devices sensitive to Cherenkov radiation, called Cherenkov detectors, have been used extensively for detecting fast moving charged particles, and measuring the intensity of reactions etc.

Since the recently constructed metamaterials have negative refractive index, which results in the so-called reversed CR [1], a phenomenon can be used to improve the Cherenkov detectors. The reason is that in a conventional dielectric medium, the emitted radiation travels in the same direction as the particles, which will interfere with the detection of those photons. However, in metamaterials, photons and charged particles move in opposite directions so that their physical interference is reduced. Though great progress has been made in the past decade on theoretical, numerical and experimental study of reversed CR [51], many challenging issues need to be resolved before the reversed CR can be put in practical applications. Since the intensity of CR increases with frequency, the optical or ultraviolet spectrum is more useful for detection. However, fabrication techniques for creating low loss metamaterials at optical or ultraviolet frequencies [52] is far less mature.

1.11 Frequency Selective Surface (FSS)

Frequency Selective Surfaces are planar periodic structures of identical patches or apertures of conducting elements duplicate periodically in either a one or two-dimensional array on a dielectric substrate as shown in figure 1-13. Because of their frequency selective properties, FSS are incorporated in a wide variety of applications such as the realization of reflector antennas, radome design, making polarizers and beam splitters, and also as radar absorbing structure [55]. The frequency behavior of the FSS depends on the shape of the elements (apertures/patches), their size, spacing, and thickness of the metal screen. Generally FSS are employed in front of a grounded dielectric slab (substrate) to synthesize high-impedance absorbing surfaces.

Figure 1-13: Plane FSS with different unit cells [53- 54].

1.11.1 FSS Element Comparison

There are four different types of possible element-type FSS arrays: center connected, loop, solid interior and combination. See figure 1-14 for some examples of each element type [55].

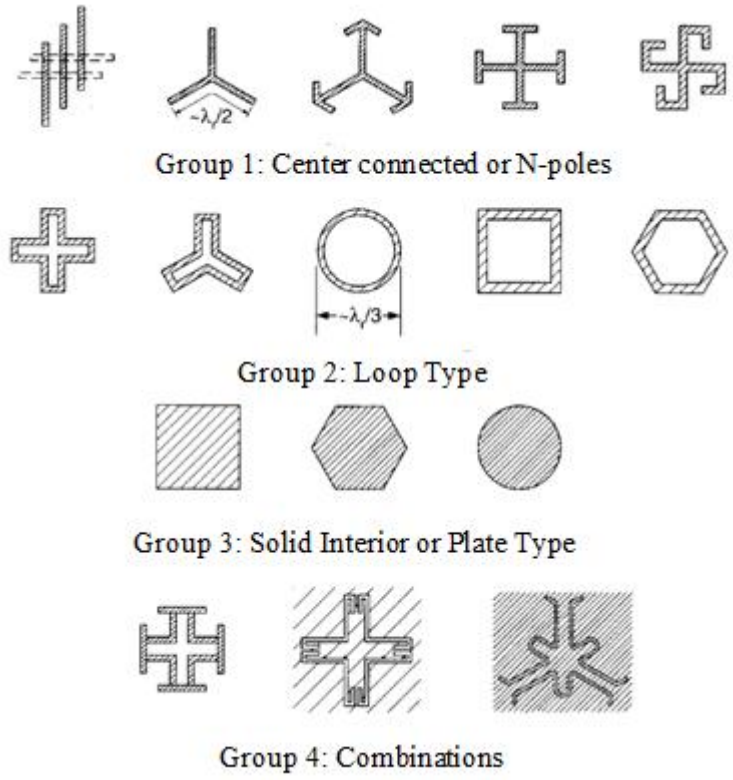

Figure 1-14: The four major groups of FSS elements [55].

The first group, the center connected elements, are a viable candidate for both radiating and non-radiating arrays. Perhaps the most recognizable from the center connected group is the dipole [55]. The loop elements are in general an excellent choice for non-radiating element FSS arrays. These elements are typically smaller in the *x* and *y* directions than the center connected elements with respect to a wavelength and thus can be spaced close to one another. Plate elements in general do not have very desirable characteristics. First the element

have *x* and *y* dimensions around a half of a wavelength, which limits how closely these elements can be placed next to one another. In addition plates are highly inductive elements with small capacitances between them, leading to issues with regard to achieving resonance. If the FSS never resonates, then it is impossible to achieve perfect reflection. This is due to the fact that at resonance, the FSS becomes a short circuit (assuming the materials are lossless) and thus acts as a perfect electric conductor (PEC) ground plane [55]. Finally combination elements are too diverse to generalize in any meaningful way. The possibilities in this group are as boundless as the imagination of the designer. Some possible examples of elements in this group have already been shown in figure 1-14 [55].

The FSS arrays effectively create low pass, high pass, band stop, and band pass filters respectively (see figure 1-15) to electromagnetic energy at their design frequency range. These types of filters are used in a wide variety of applications, including radomes, dichroic surfaces, and circuit analog absorbers [56].

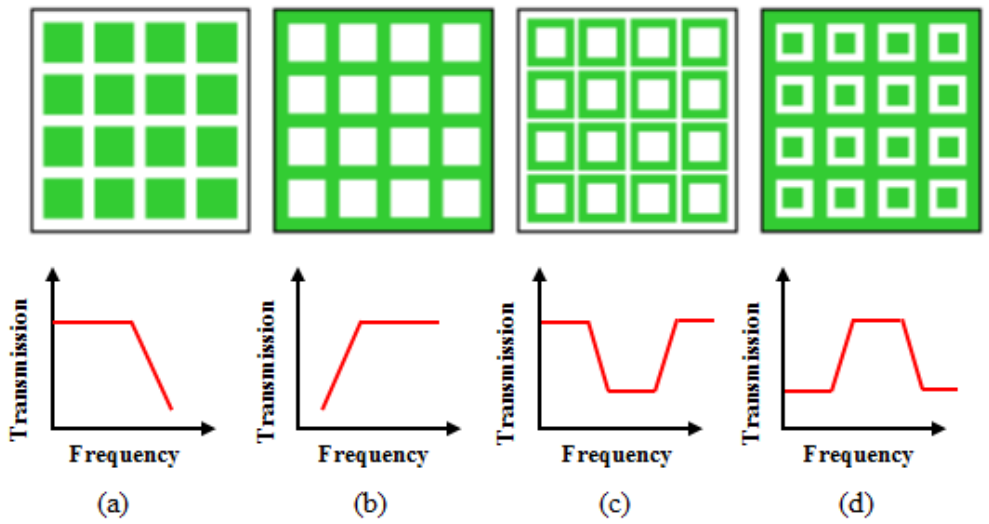

Figure 1-15: Filter types based on FSS (a)-low pass filter (b)-high pass filter(c)-band stop filter (d)-band pass filter [57].

1.11.2 FSS applications

The FSS found their application in:

1- Selective shielding of the electromagnetic interference from high power microwave heating machines adjacent to wireless communication base stations,

2- Selective shielding of frequencies of communication in sensitive areas (military installations, airport, police.),

3- Protection from harmful electromagnetic radiation especially in the 2-3 GHz band in domestic environment, schools, hospitals etc. arising externally (wireless communication base stations) or internally (microwave ovens),

4- Control of radiation at unlicensed frequency bands (Bluetooth applications, 2.45 GHz),

5- Pico-cellular wireless communications in office environments such as the Personal Handy phone System in offices where to improve efficiency each room needs to prevent leakage of radio waves into and of the room. This implies that windows, floor and ceiling need to be shielded. Kajima Research Institute is developing such a film to be applied to buildings,

6- Isolation of unwanted radiation. FSS windows can be incorporate in trains prevent mobile phone frequencies; around base station antennas to filter out unwanted radiation.

1.12 Conclusion

The metamaterials are artificial materials made of a periodic arrangement of unit cells with some unique properties. Such properties include a simultaneous negative or positive permittivity and/or permeability. Its properties can be tailored in a broader manner than with classical materials.

Metamaterials can be used for several interesting devices in microwave and terahertz engineering such as antennas, sensors, superlens, and biomedical applications.

2. Effective parameters extraction of homogenized metamaterials

2.1 Introduction

As presented in chapter 1, the metamaterials is an artificially structured material with sub-wavelength unit cells. Now we must ask two questions: Is a metamaterial structure with sub-wavelength unit cell equivalent to a homogenous effective medium? How to determine the effective medium parameters once the periodic structure is known? The answers to these questions are key points for the homogenization of artificial particles and effective medium theory.

This chapter is divided into two parts. In the first part we present a brief overview of the homogenization of composite materials. The second part deals with the effective electromagnetic parameters extraction methods. These methods use either the *S* parameters method or the field averaging method (field summation).

2.2 The effective media

All electromagnetic phenomena are governed by Maxwell's equations, which are a set of equations describing the interaction between fields, sources, and material properties. Impinging fields in a system can influence the organization of electric and magnetic dipoles in a medium. Fields can induce polarization and magnetization to some degree, depending on the particular material involved. The electromagnetic properties of a material are described by two material parameters: the dielectric permittivity ε and the magnetic permeability μ, which characterize the coupling between the material and the electric and magnetic field components, respectively. These two parameters, along with other values, which are the refractive index $n = \sqrt{\varepsilon\mu}$ and the impedance $Z = \sqrt{\mu/\varepsilon}$, are essentially macroscopic effective parameters .They are used to describe the overall average response of the material as a whole. Microscopically, a piece of crystal consists of atoms arranged in a periodic or non periodic manner with a lattice constant of a few angstroms. On the atomic scale, in each atom or molecule, tiny electric dipoles can be excited by the electric component of incident wave and subsequent radiation of the energy in the dipoles occurs with a certain delay in time. The excited dipoles create a periodic local field in the crystal, referred to as Lorentz local field; therefore the field distribution inside the crystal is certainly not uniform. However, the incident wave does not really feel the underlying inhomogeneity in the crystal, nor does it feel the processes of absorption and radiation. On the macroscopic scale, the detailed features and responses of the inhomogeneous structure are averaged, and relationships can be established

between the macroscopic field vectors in Maxwell's equations, namely the electric field $\vec{E}$, the magnetic field $\vec{H}$, the electric displacement field $\vec{D}$ and the magnetic flux density $\vec{B}$. This is the origin of the permittivity and permeability parameters of materials. At different frequency range, this complicated physics is usually described using the transmittance and reflectance of waves with a certain retardation (delay). In addition, absorbed waves account for losses in the material and can be related to the imaginary parts of the complex constitutive parameters that are electric permittivity, magnetic permeability, and refractive index.

Similarly, the scale of inhomogeneities in a metamaterial is much smaller than the wavelength of interest. The inhomogeneity scale corresponds to the lattice constant of the artificial structure for the case of periodic metamaterial as shown in figure 2-1.

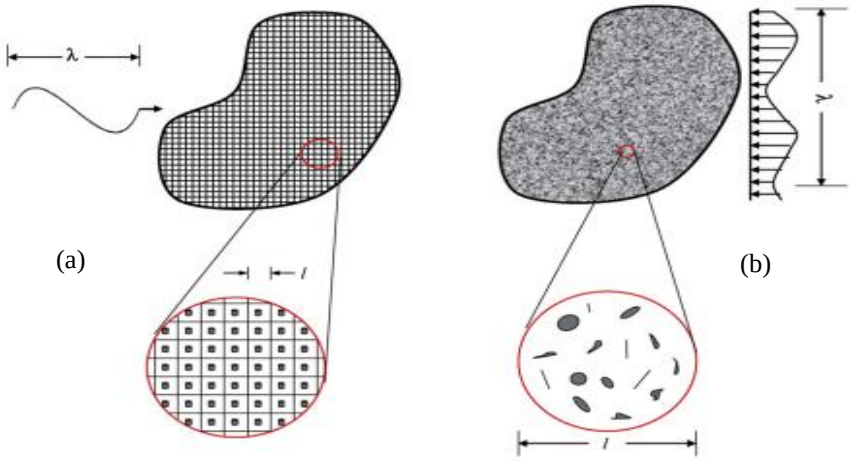

Figure 2-1: Composite material with (a) periodic (b) non-periodic structure

In figure 2-1, the largest heterogeneity length scale *l* should be small enough compared to the smallest length scale λ, that is of physical importance. For a periodic medium (in the left of the figure) *l* is the unit cell size while in a random medium (in the right of the figure) it should be the smallest size of a sphere which at any position is a statistical representative of the entire body.

Then the key of homogenization is when the size of the unit cell is much smaller than the operating wave length [58],[60]. This property is called the homogenization criterion. Since the metamaterial can be seen as an homogeneous medium, the effective parameters can be determined and the electromagnetic response is valid as shown in figure 2-2.

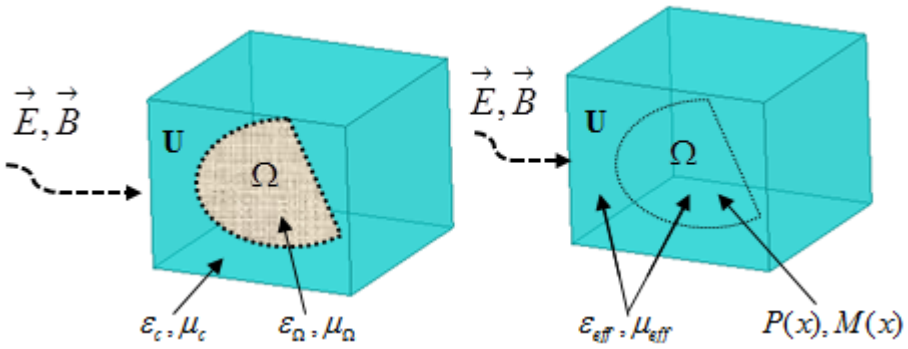

Figure 2-2:A two-phase heterogeneous unit cell (left) and its equivalent to homogeneous unit cell with the imposed polarization fields *P* and *M* (right)[59]

This fact explains again why metamaterials made from basic constituents are identified as materials instead of devices [61]. From the point of view of Maxwell's equations, a material is a collection of sub-wavelength units with global properties described by ε and μ. Through the dedicated design of meta-atoms, which is usually a delicate metal-dielectric structure, metamaterial research allows us to tailor the electromagnetic response of media in an unprecedented manner. Finally, there are cases such as bianisotropic media where the electromagnetic response is not sufficiently described with ε and μ tensors because of the complexity of the unit scatterers. Such structures may require additional material parameters like magnetoelectric coefficients, which link the electric field vectors and the magnetic ones. Although some important metamaterial elements like split-ring resonators are bianisotropic to some extent.

2.3 Effective parameters extraction

If the spacing between scattering elements is much smaller than the operating wave length, so we can consider that the metamaterial is homogenous and it responds to electromagnetic waves in a similar way [62]. It is possible to describe the metamaterials as continuous materials [63]. In these conditions, they can be characterized by effective parameters without considering the local field distribution. This part of the chapter treats classical and numerical homogenization approaches, which are the *S* parameters extraction method (Fresnel inversion method) and the field summation method which is an averaging approach.

2.3.1 Fresnel inversion extraction method

Smith et al [70] proposed a method to extract the constitutive parameters by using scattering parameters *S*, which is suitable to be applied for both numerical simulation and

experimental measurements. Several reports have been published [71]; most of them deal with the isotropic parameters of permittivity and permeability. However, it has already been demonstrated [64] that most metamaterials are intrinsically bianisotropic due to the asymmetry of the composite components such as split-ring resonators. For a bianisotropic metamaterial, the propagation wave vector is related not only to permittivity and permeability but also to the magnetoelectric coupling coefficient [64]. Moreover, there are some special metamaterial designs that take advantage of the property of bianisotropy. Consequently, in order to obtain a true picture for these metamaterials, it is important to present not only the effective parameters of permittivity and permeability but also some other important parameters, such as the magnetoelectric coupling coefficient ζ_0. Only then one can provide true data for the effective parameters. Figure 2-3 shows the schematics of a homogeneous bianisotropic material slab.

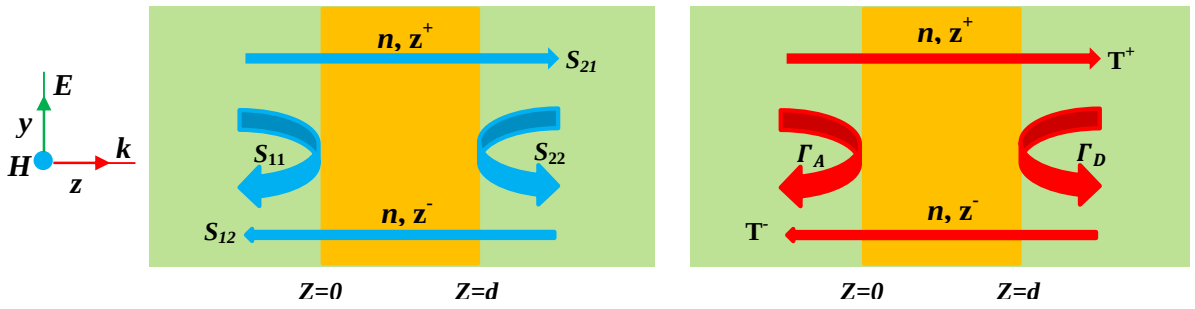

Figure 2-3: Transmission and reflection coefficients in bianisotropic metamaterial.

The metamaterial effective parameters extraction requires two steps [65]:

1- Computation of the homogenized metamaterial forward and backward wave impedance (z^+, z^-) and complex refractive index (n) (figure 2-3) which are expressed in terms of reflection and transmission coefficients (S_{ij}).

2- Retrieval of the electromagnetic constitutive parameters (permittivity, permeability and magnetoelectric coupling coefficient) from the S_{ij} parameters.

2.3.2.1 Metamaterial wave impedances and refractive index computation

In figure 2-3, a plane wave polarized in the y axis propagates along the z direction and is incident upon the structure. We suppose that the configuration in figure 2-3 has a bianisotropic property; the electric field in the y direction induces a magnetic dipole in the x direction, while the magnetic field in the x direction also induces an electric dipole in the y direction [66].

By assuming that the medium is reciprocal [67] and that the harmonic time dependence is $e^{-j\omega t}$, implying that $\varepsilon'' > 0$ and $\mu'' > 0$ simultaneously at all frequencies. We use primes and double primes for denoting real and imaginary parts of a complex quantity. The constitutive relations can be written ($\vec{E}$ - $\vec{H}$ or Tellegen representation [68]) as:

$$\vec{D} = \bar{\bar{\varepsilon}}.\vec{E} + \bar{\bar{\xi}}\vec{H} \qquad (2\text{-}1)$$

$$\vec{B} = \bar{\bar{\mu}}.\vec{H} + \bar{\bar{\varsigma}}.\vec{E} \qquad (2\text{-}2)$$

Where:

$$\bar{\bar{\varepsilon}} = \varepsilon_0 \begin{pmatrix} \varepsilon_{xx} & 0 & 0 \\ 0 & \varepsilon_{yy} & 0 \\ 0 & 0 & \varepsilon_{zz} \end{pmatrix} \qquad (2\text{-}3)$$

$$\bar{\bar{\mu}} = \mu_0 \begin{pmatrix} \mu_{xx} & 0 & 0 \\ 0 & \mu_{yy} & 0 \\ 0 & 0 & \mu_{zz} \end{pmatrix} \qquad (2\text{-}4)$$

$$\bar{\bar{\xi}} = \frac{1}{c} \begin{pmatrix} 0 & 0 & 0 \\ -\mathrm{j}\zeta_0 & 0 & 0 \\ 0 & 0 & 0 \end{pmatrix} \qquad (2\text{-}5)$$

$$\bar{\bar{\varsigma}} = \frac{1}{c} \begin{pmatrix} 0 & \mathrm{j}\zeta_0 & 0 \\ 0 & 0 & 0 \\ 0 & 0 & 0 \end{pmatrix} \qquad (2\text{-}6)$$

In equations (2-1) to (2-6) $\vec{E}$, $\vec{H}$, $\vec{D}$, and $\vec{B}$ are, respectively, the electric and magnetic field intensities and flux densities; and ε_0 and μ_0 are, respectively, the permittivity and permeability of the vacuum; *c* is the speed of light in vacuum; and ($\bar{\bar{\xi}}$, $\bar{\bar{\zeta}}$) are the tensors quantities of the magnetoelectric coupling coefficient. In the present study, we will only deal with the determination of forward and backward wave impedances entailed by ε_{yy}, μ_{xx}, and ζ_0, since other unknown four quantities ($\varepsilon_{xx}, \varepsilon_{zz}, \mu_{yy}$,and μ_{zz}) are not related to the bianisotropic structure in figure 2-3 when a plane wave with a polarization in the *y* direction is incident in the *z* direction.

From Maxwell's curl equations and using equations (2-3) to (2-6), we find:

$$\frac{\partial^2 E_y}{\partial z^2} + k_z^2 E_y = 0 \qquad (2\text{-}7)$$

$$\frac{\partial^2 H_x}{\partial z^2} + k_z^2 H_x = 0 \qquad (2\text{-}8)$$

$$Z^+ = \frac{-E_y^+}{H_x^+} = \frac{z_0 \mu_x}{(n + j\zeta_0)} \qquad (2\text{-}9)$$

$$Z^- = \frac{+E_y^-}{H_x^-} = \frac{z_0 \mu_x}{(n - j\zeta_0)} \qquad (2\text{-}10)$$

$$z^+ = Z^+ / z_0 \text{ and } z^- = Z^- / z_0 \qquad (2\text{-}11)$$

$$k_z = nk_0 \text{ and } n = \pm\sqrt{\varepsilon_y \mu_x - \zeta_0^2} \qquad (2\text{-}12)$$

Here, E_y and H_x are, respectively, the y and x components of $\vec{E}$ and $\vec{H}$; k_z and k_0 are, respectively, the wave number of the wave propagating in the z direction and in free-space; Z^+ and Z^- are, respectively, the wave impedances inside the medium for forward (+z) and backward (-z) propagations; z^+ and z^- are normalized wave impedances; z_0 is the wave impedance (or intrinsic impedance) in air; and n is the refractive index of the sample. It is seen from equations (2-9) and (2-10) that the important feature of a bianisotropic metamaterial is that wave impedances are different for waves propagating in forward and backward directions.

For the derivation of *S*-parameters, we utilize the schematics of a homogeneous bianisotropic material slab with thickness d suspending in air as shown in figure 2-3, we derive the forward and backward reflection and transmission *S*-parameters in compact form as:

$$S_{11} = \frac{\Gamma_A (1 - T^2)}{1 - \Gamma_B T^2} \qquad (2\text{-}13)$$

$$S_{21} = S_{12} = \frac{\Gamma_C T}{1 - \Gamma_B T^2} \qquad (2\text{-}14)$$

$$S_{22} = \frac{\Gamma_D (1 - T^2)}{1 - \Gamma_B T^2} \qquad (2\text{-}15)$$

Such as:

$$\Gamma_A = \frac{z^+ - 1}{z^+ + 1} \quad (2\text{-}16)$$

$$\Gamma_B = \Gamma_A \Gamma_D \quad (2\text{-}17)$$

$$\Gamma_C = 1 - \Gamma_B \quad (2\text{-}18)$$

$$\Gamma_D = \frac{z^- - 1}{z^- + 1} \quad (2\text{-}19)$$

$$T = e^{jk_0 nd} \quad (2\text{-}20)$$

Where Γ_A, Γ_D are the reflection coefficients in the reference planes $Z = 0$ and $Z = d$, respectively, Γ_B, Γ_C are related into Γ_A, Γ_D, and T is the transmission coefficient.

Substituting equations (2-13), (2-14) and (2-15) into equations (2-16), (2-17), (2-18), (2-19) and (2-20) to obtain the following variables:

$$z^+ = \frac{-\Lambda_2 \pm \sqrt{\Lambda_2^2 - 4\Lambda_1\Lambda_3}}{2\Lambda_1} \quad (2\text{-}21)$$

$$z^- = \frac{\Lambda_4 z^+ + 1}{z^+ + \Lambda_4} \quad (2\text{-}22)$$

Where

$$\Lambda_1 = S_{21}^2 - (1 - S_{11})(1 - S_{22}) \quad (2\text{-}23)$$

$$\Lambda_2 = 2(S_{11} - S_{22}) \quad (2\text{-}24)$$

$$\Lambda_3 = (1 + S_{11})(1 + S_{22}) - S_{21}^2 \quad (2\text{-}25)$$

$$\Lambda_4 = \frac{S_{11} + S_{22}}{S_{11} - S_{22}} \quad (2\text{-}26)$$

And

$$n = \frac{1}{k_0 d}\left[\mp(\ln T)'' \mp 2\pi m - j(\ln T)'\right] \quad (2\text{-}27)$$

Where (m = 1, 2, 3,…) denotes the branch index value. It is seen from equation (2-27) that the index n have multiple solutions depending on m values, the correct choice of m for unique retrieval of n can be realized by different technique [69].

Note that the correct sign of z^+, z^- and n corresponds to that for which the passivity conditions are satisfied: $(z^+)' > 0$, $(z^-)' > 0$, and $(n)'' \geq 0$.

2.3.2.2 Calculation of the constitutive electromagnetic parameters

From equations (2-21), (2-22), (2-27) and (2-16) (2-20).We deduce the effective parameters expressions:

$$\zeta_0 = \frac{(2-\Gamma_C)^2 - (4\Gamma_A^2 + \Gamma_C^2)}{4i\Gamma_A\Gamma_C / n} \quad (2\text{-}28)$$

$$\mu_x = \frac{\Gamma_C(n^2 + \zeta_0^2)}{n(2-\Gamma_C) - 2n\Gamma_A - i\Gamma_C\zeta_0} \quad (2\text{-}29)$$

$$\varepsilon_y = \frac{n^2 + \zeta_0^2}{\mu_x} \quad (2\text{-}30)$$

2.3.2 Validation of the *S* parameters inversion method

The validation of the *S* parameters inversion method is examined by extracting the constitutive parameters of metamaterial using a finite element method based commercial simulation code and compare the results with smith et al [70]

The metamaterial structure in [70] is composed of split-ring resonator (SRR) and wire as shown in figure 2-4 which consists of two types of conducting elements, a split ring and wire, both made of copper (thickness 17 µm). The split ring and the wire are positioned on opposite sides of the dielectric slab of thickness 0.25 mm.

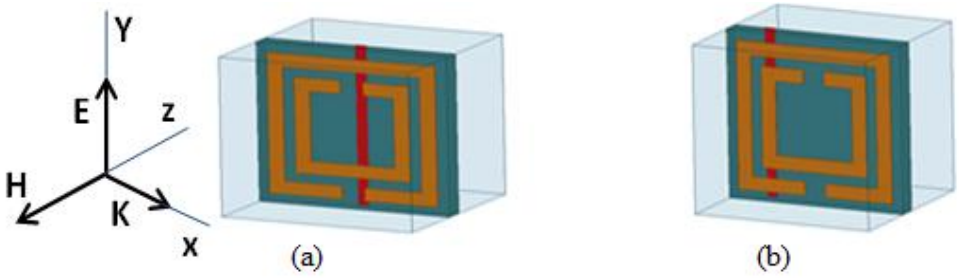

Figure 2-4: The split ring resonator SRR (a)-symmetric (b)-Asymmetric.

The extracted electromagnetic parameters of the symmetric and asymmetric unit cell are shown in figure 2-5 and figure 2-6 respectively.

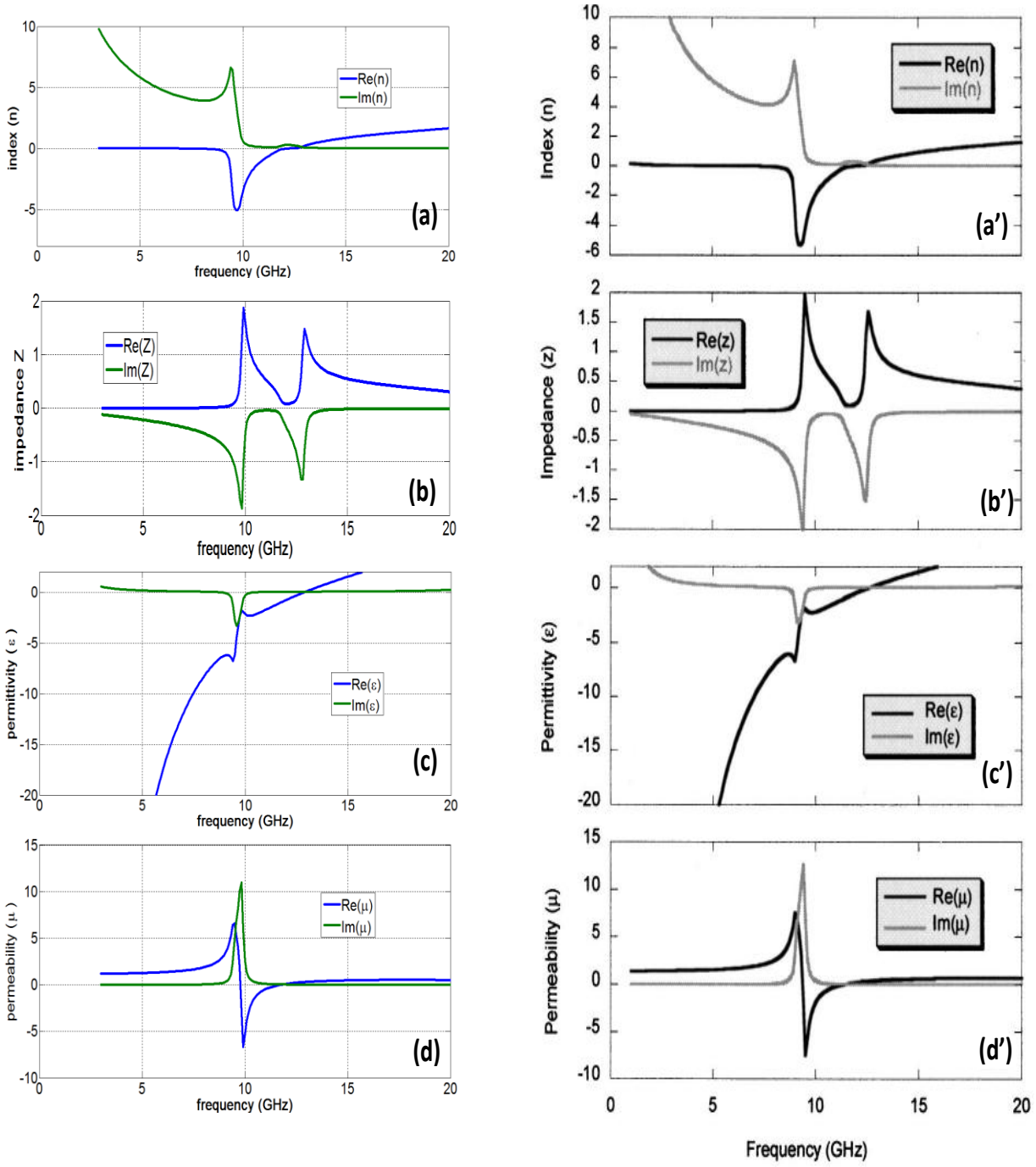

Figure 2-5: Comparison between our extraction program results (left: with colors) and those obtained from [70] (right) for symmetric unit cell: (a)-(a') Index (n); (b)-(b') Impedance (z); (c)-(c') relative dielectric permittivity(ε); (d)-(d') relative magnetic permeability (μ).

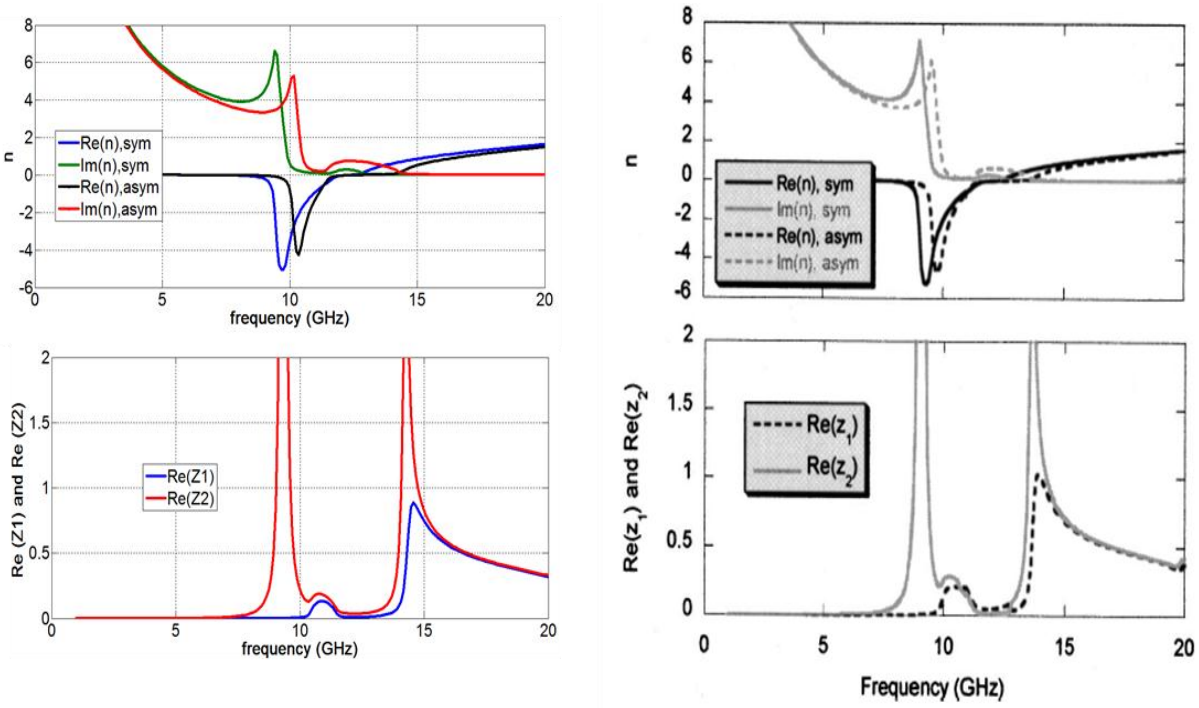

Figure 2-6: Comparison between our extraction program results in the left and smith's results [70] in the right for asymmetric unit cell (a)-(b) index *n* (c)-(d) impedance *z* .

We observe from figure 2-5 and figure 2-6 the good agreement between our results, if they are compared to those obtained in [70] for the symmetrical and asymmetrical unit cells. The asymmetrical unit cell is obtained by shifting the conductor wire 0.75 mm away from its centered position which corresponds to the symmetrical one.

2.3.3 Field summation extraction

In order to validate our simulated results we use another method called the field summation method which is based on the electromagnetic field distribution (field cards) of the unit cell.

We used the Maxwell's curl equation and the distributions $\vec{D}$ and $\vec{B}$ fields can then be calculated from those $\vec{E}$ and $\vec{H}$ fields by using this formulation:

$$\begin{aligned} \vec{\nabla} \wedge \vec{E} &= -j\omega \vec{B} \\ \vec{\nabla} \wedge \vec{H} &= j\omega \vec{D} \end{aligned} \qquad (2\text{-}31)$$

In the quasi-static regime when the size *d* of unit cell is small compared to the wavelength and the inclusion volume is small, it is possible to calculate the effective permittivity and permeability.

We start by integrating field variables over an appropriate volume and surface field variables. The constitutive relations for Tellegen representation in the equations (2-1) and (2-2) can now be written as:

$$\vec{D}_y = \varepsilon_0 \varepsilon_{yy} \vec{E}_y - j\zeta_0 \sqrt{\mu_0 \varepsilon_0}\, \vec{H}_x \qquad (2\text{-}32)$$

$$\vec{B}_x = \mu_0 \mu_{xx} \vec{H}_x + j\zeta_0 \sqrt{\mu_0 \varepsilon_0}\, \vec{E}_y \qquad (2\text{-}33)$$

Equations (2-32) and (2-33) involve three unknowns $(\varepsilon_{yy}, \mu_{xx}, \zeta_0)$, so we need one more equation to solve the system equation of three unknowns. The additional equation is obtained from the wave impedance in the backward and the forward directions given by equations (2-9) and (2-10). The constitutive parameters can be written as:

$$\varepsilon_{yy} = \frac{< D_y >_p}{\varepsilon_0 < E_y >_V} + j\zeta_0 \sqrt{\mu_0 \varepsilon_0}\, \frac{< H_x >_p}{\varepsilon_0 < E_y >_V} \qquad (2\text{-}34)$$

$$\mu_{xx} = \frac{< B_x >_V}{\mu_0 < H_x >_p} - j\zeta_0 \sqrt{\mu_0 \varepsilon_0}\, \frac{< E_y >_V}{\mu_0 < H_x >_p} \qquad (2\text{-}35)$$

Where:

$$\zeta_0 = \frac{j(F.z_0^2 + N^2.A)}{-2.N.z_0 + d.z_0^2 + N^2.b} \qquad (2\text{-}36)$$

$$F = \frac{< B_x >_V}{\mu_0 < H_x >_p}, z_0 = 120\pi, N = \frac{< E_y >_V}{< H_x >_p}, A = \frac{< D_y >_p}{\varepsilon_0 < E_y >_V} \qquad (2\text{-}37)$$

$$d = \frac{\sqrt{\mu_0 \varepsilon_0}}{\mu_0} \frac{< E_y >_V}{< H_x >_p}, b = \frac{\sqrt{\mu_0 \varepsilon_0}}{\mu_0} \frac{< H_x >_p}{< E_y >_V} \qquad (2\text{-}38)$$

For example, we calculate the effective permeability and permittivity of the SRR unit cell (Broadside-coupled SRR), represented in figure 2-7, using the field summation method. The overall electromagnetic material properties of the periodic composites are calculated from expressions (2-34), (2-35), and (2-36). The averaged $\vec{E}$ and $\vec{H}$ fields are calculated in the volume *V*, the other two electromagnetic fields $\vec{B}$ and $\vec{D}$ are averaged appropriately on the surfaces *S* normal and parallel to the common axis of the SRR (see figure 2-7). These average

fields are substituted in the constitutive equations, which are then solved together with the dispersion relation for the bianisotropic medium.

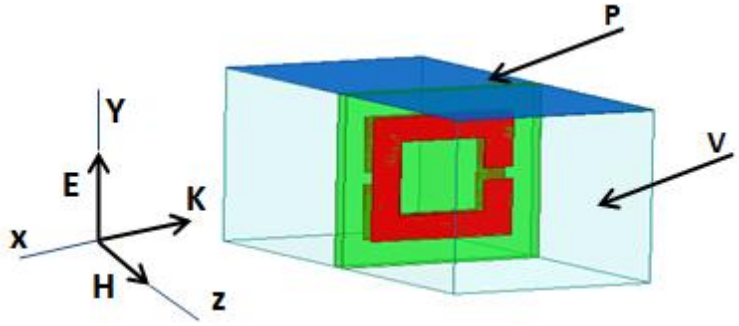

Figure 2-7: The split ring resonator SRR type (Broadside-coupled SRR)

Using the procedure discussed above, the extracted effective parameters of broadside coupled SRR cell are shown in figure 2-8, 2-9, and 2-10.

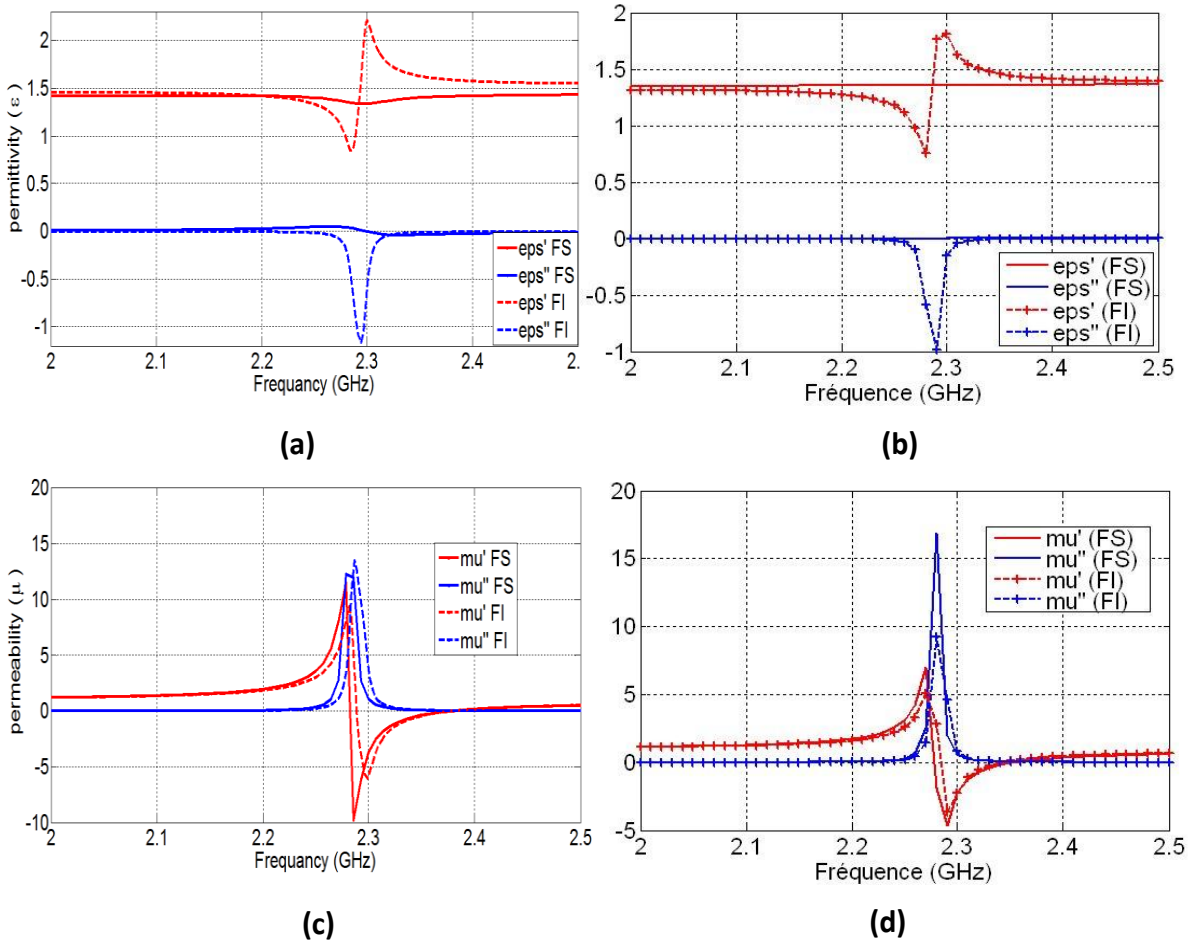

Figure 2-8: Results comparison between our extraction programs in the left and [71] in the right using Fresnel inversion (FI) and field summation (FS) methods.

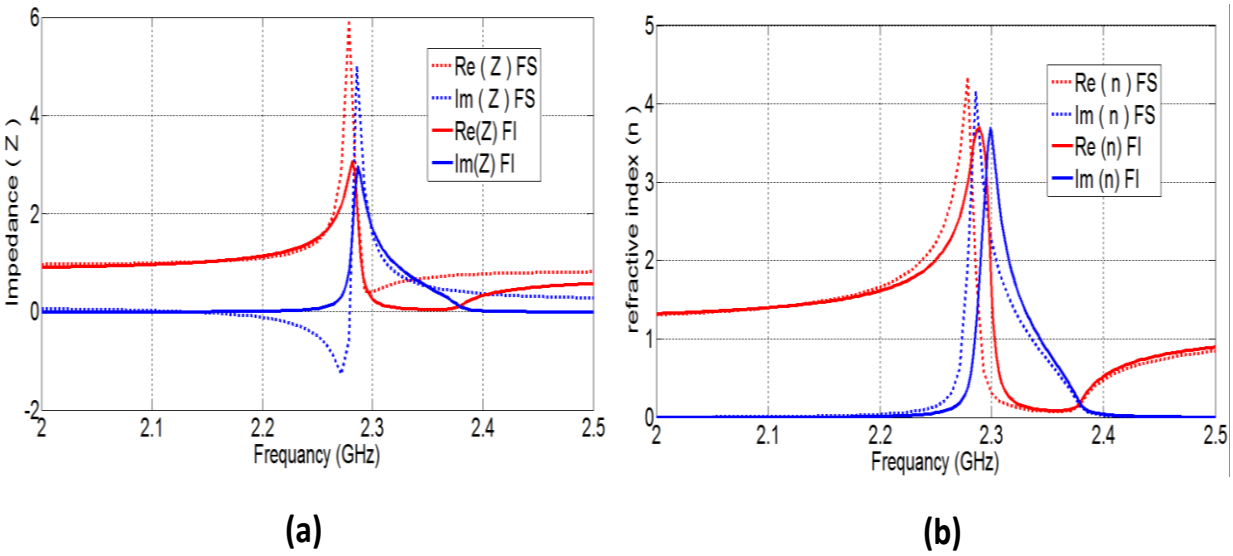

Figure 2-9: (a) impedance *z*, (b) refractive index *n*, by Fresnel inversion (FI) and field summation methods (FS)

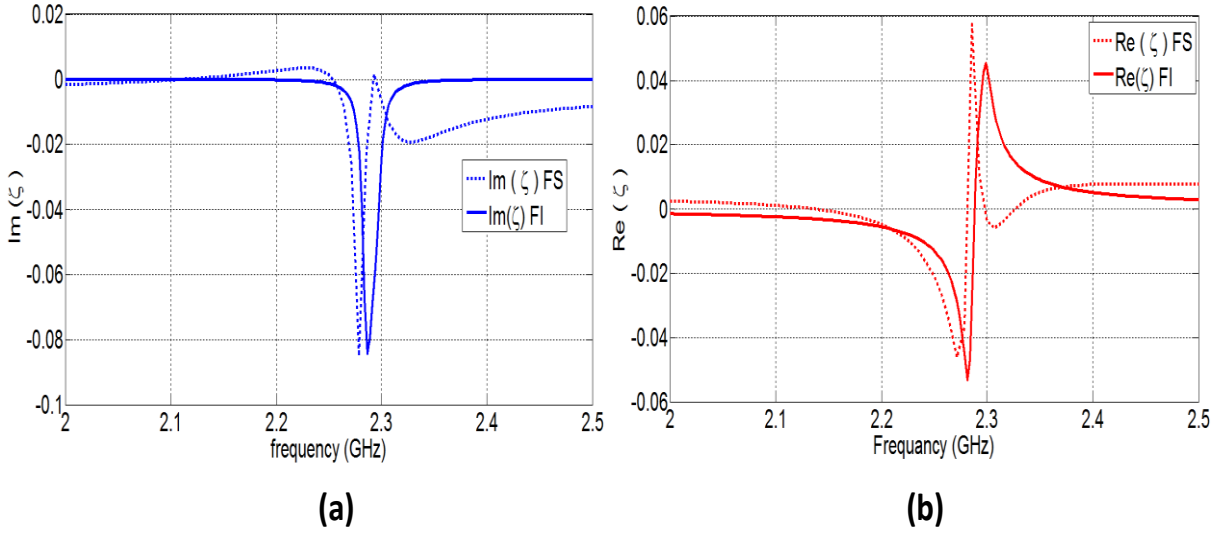

Figure 2-10: Result for the magnetoelectric coupling coefficient ζ , by Fresnel inversion (FI) and field summation methods (FS).

From figure 2-8, We note the same behaviors in the results obtained by the Fresnel inversion and the field summation method for the extraction permittivity and permeability with those obtained in [71]

From figure 2-9 and 2-10, the complex index, impedance, and the magnetoelectric coupling parameter ζ obtained by Fresnel inversion (FI) and field summation method (FS) have the same behaviors.

2.4 Symmetric and asymmetric cross unit cell

The difference between the symmetric and asymmetric cross cells can be shown in the scattering parameters *S*. The scattering parameters are the means of characterizing the artificially structured metamaterial.

This section gives a comparative study of parameters of symmetric and asymmetric metamaterial structures.

We have seen early, the method used to calculate all the material parameters for a general bianisotropic structure based on numerical simulation of wave propagation in periodic media. We can easily verify the bianisotropic character of a structure, if there reflection scattering parameters are different ($S_{11} \neq S_{22}$).

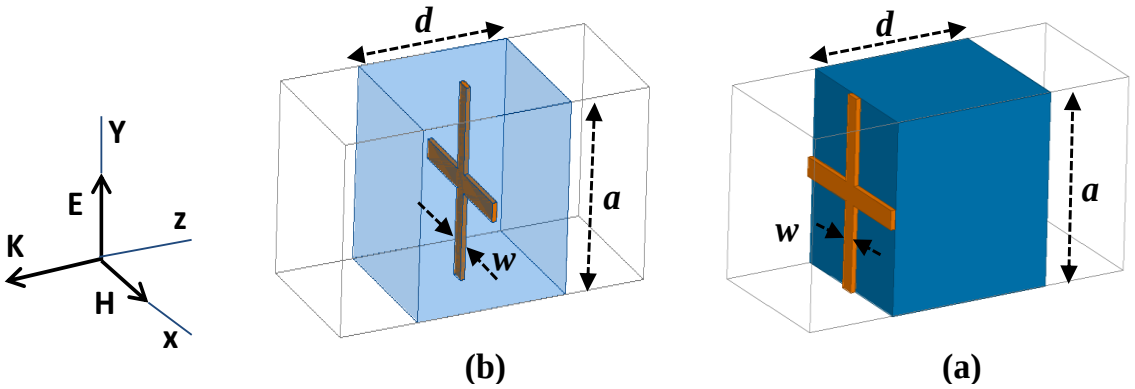

Figure 2-11: Cross metamaterial (a) - Asymmetric unit cell (b)-Symmetric unit cell.

2.4.1 Effective parameters extraction of the symmetric and asymmetric unit cell

The incident wave in the figure 2-11 is a plane wave with its wave vector $\vec{k}$ in the *z*-direction and the $\vec{E}$ field polarized in the *y*-direction, while the magnetic field vector $\vec{H}$ oriented along *x*-direction. The dimensions of the symmetric cross unit cell are the same as for the asymmetric structure, where the period a = 1 mm, the thickness d = 1.168 mm, the conducting strip width w = 0.1 mm, and the metallization thickness t = 0.035 mm.

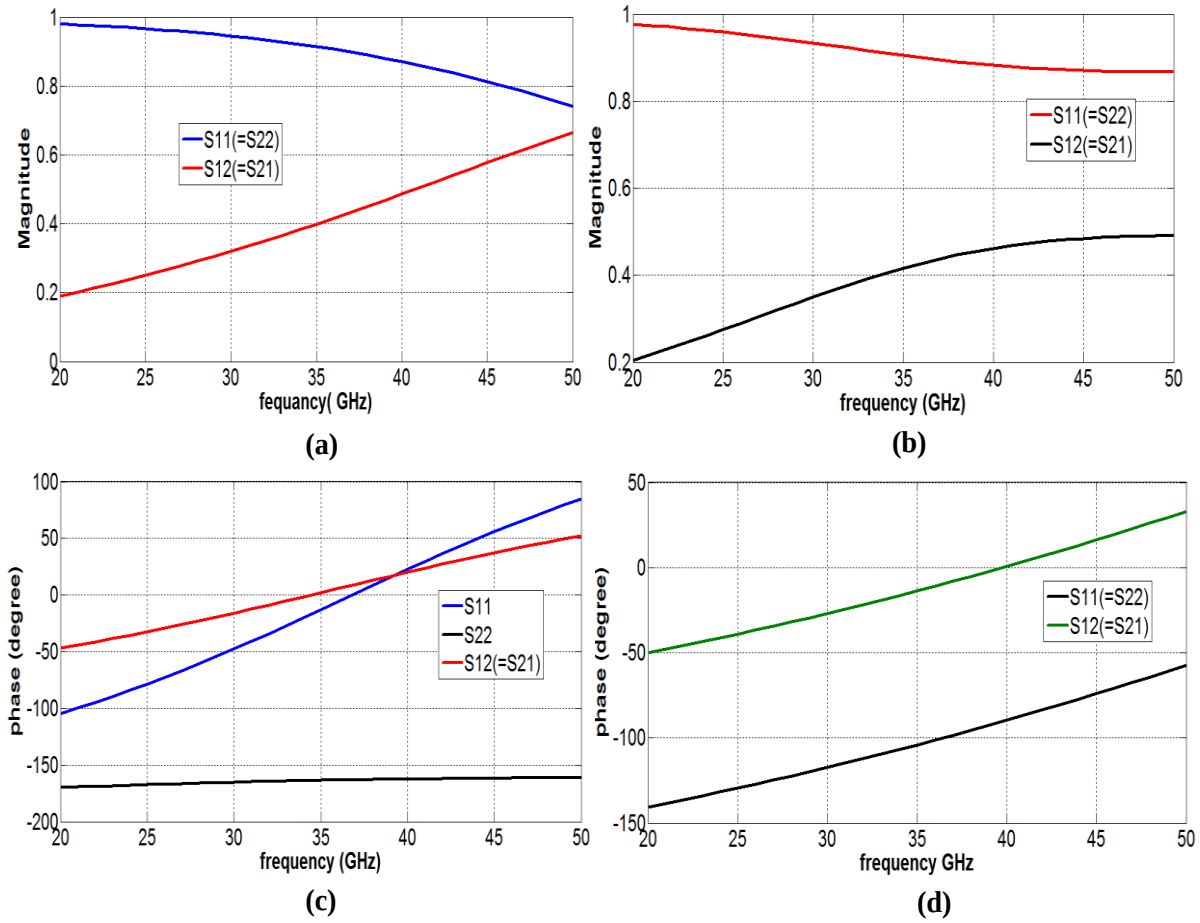

Figure 2-12: (a) Magnitude and (b) phase of the calculated *S* parameters for the symmetric unit cell (c) Magnitude and (d) phase of the calculated *S* parameters for the asymmetric unit cell.

Figure 2-12, shows the amplitude and the phase information of the calculated *S* parameters for the symmetric and asymmetric cross type metamaterial obtained by a finite element method based commercial simulation code. It can be seen that S_{11} is equal to S_{22} and S_{12} is equal S_{21} for the symmetric cell. However, for the asymmetric structure there is a great contrast in the phase of S_{11} and S_{22}.

2.4.2 Comparison between the symmetric and asymmetric unit cell

The extracted electromagnetic parameters of the symmetric and asymmetric unit cell for different values of the thickness *d* are shown in figure 2-13 and 2-16.

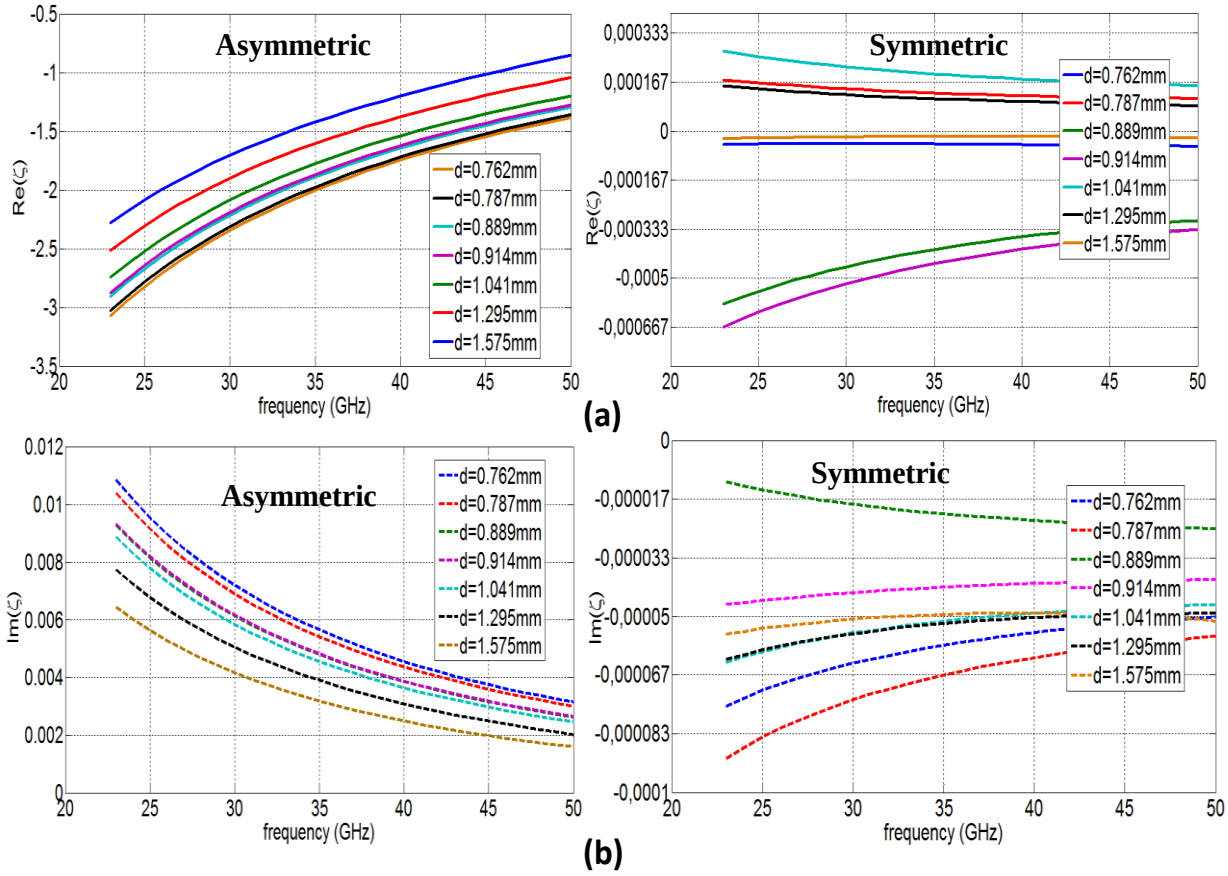

Figure 2-13: Symmetric and asymmetric unit cell magnetoelectric coupling coefficient ζ for different values of *d* (a)-real parts (b)-imaginary parts.

Evidently ζ of symmetric unit cell is close to zero, while ζ of asymmetric structure shows great variations. Indeed, in general the values of ζ depend strongly on how the surface of the composite is terminated.

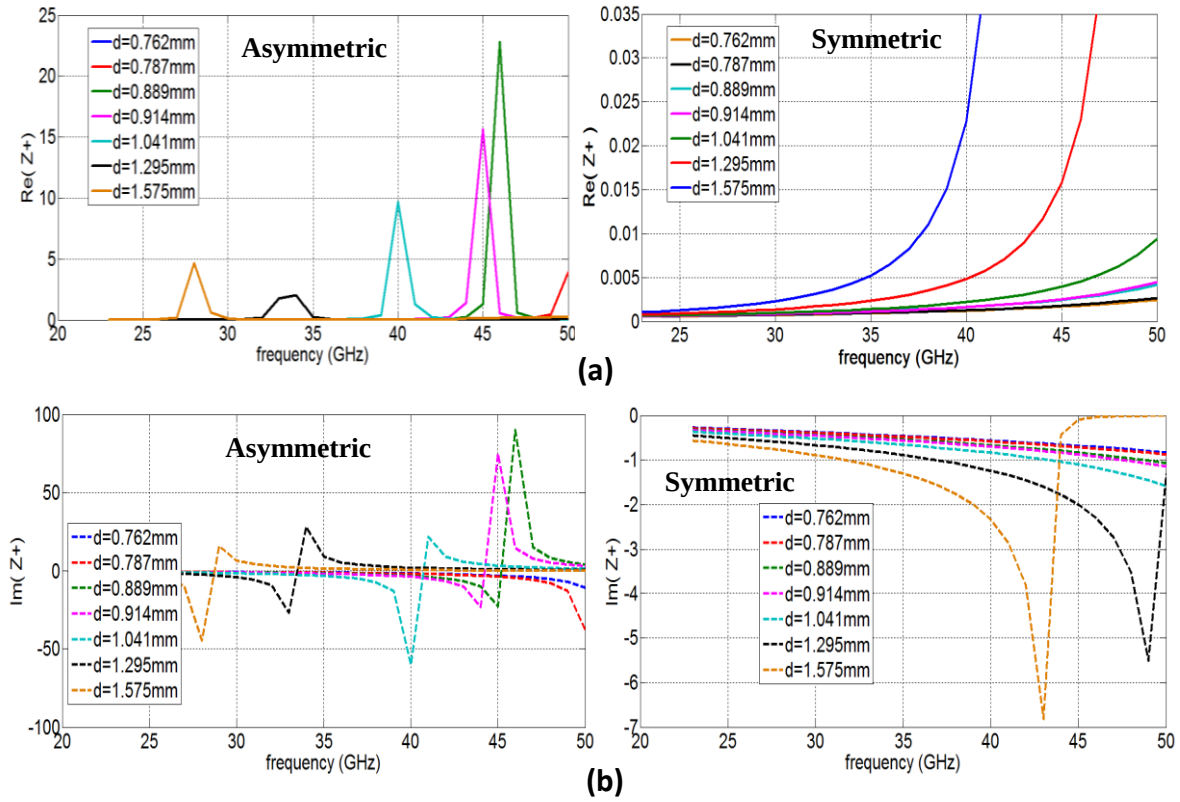

Figure 2-14: Forward impedance z^+ for the symmetric and asymmetric unit cell for different values of d (a) real part (b) imaginary part.

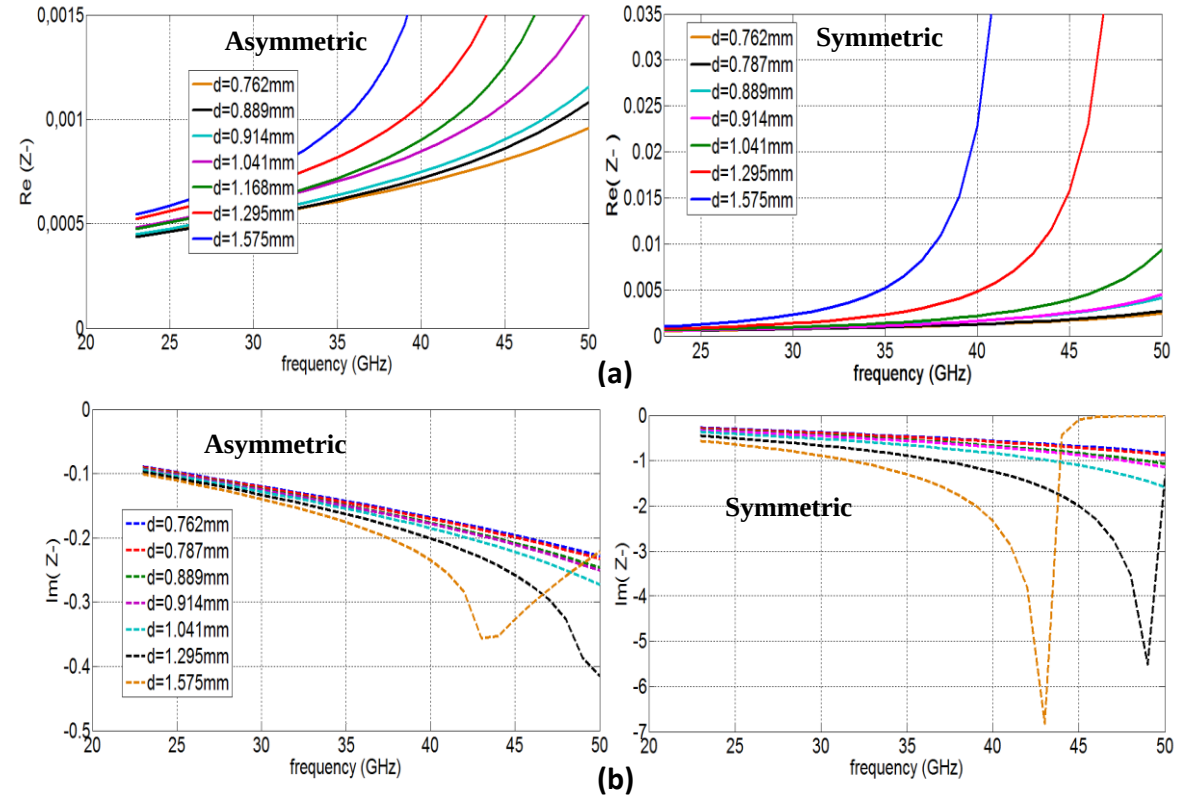

Figure 2-15 : Backward impedance z^- for the symmetric and asymmetric unit cell for different values of d (a) Real part (b) imaginary part.

The impedance is clearly different, as shown in figure 2-14 and 2-15. Obviously the symmetric unit cell presents the same impedance for the forward and backward propagation ($z^{+} = z^{-}$). However, the asymmetric unit cell presents different wave impedances for the forward and backward propagation.

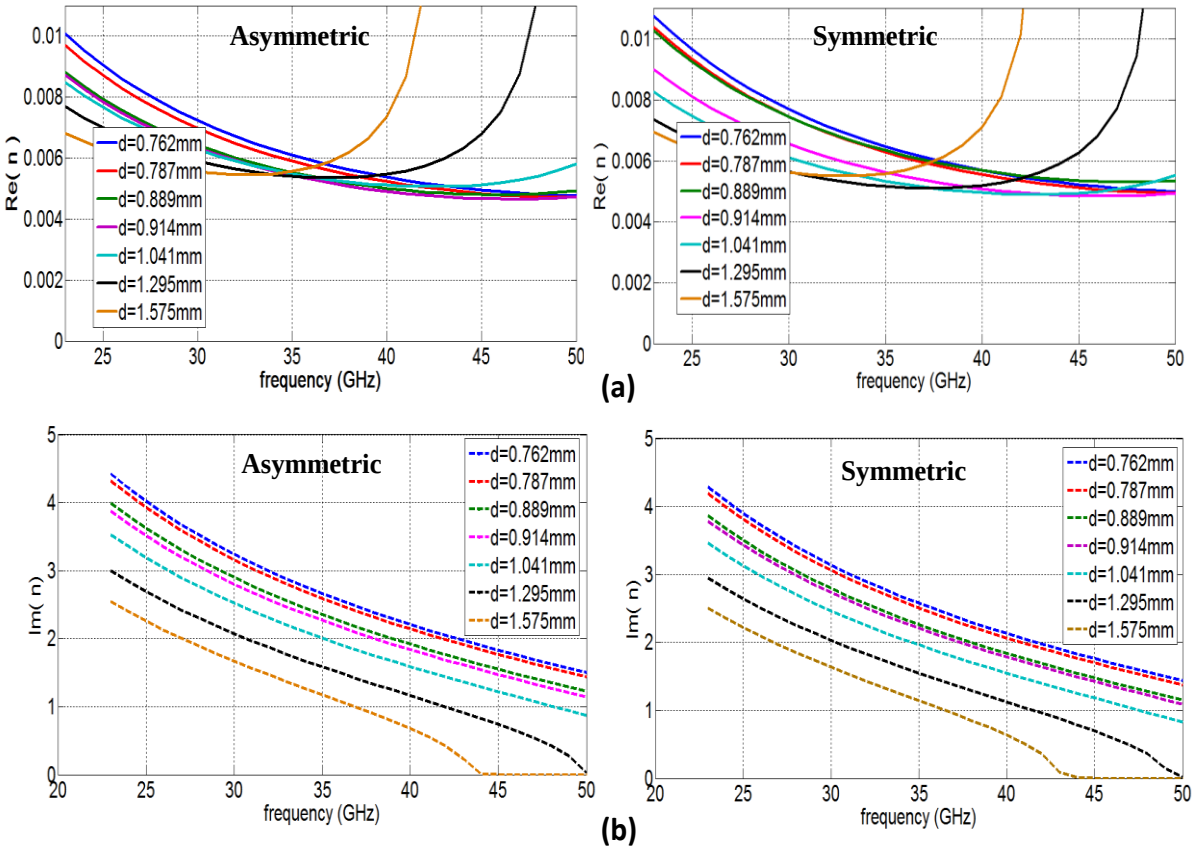

Figure 2-16: Refractive index *n*, of the symmetric and asymmetric unit cell for different values of *d* (a)-real part (b)-imaginary part .

The refraction index *n* in figure 2-16 is nearly the same for the symmetric and asymmetric structures.

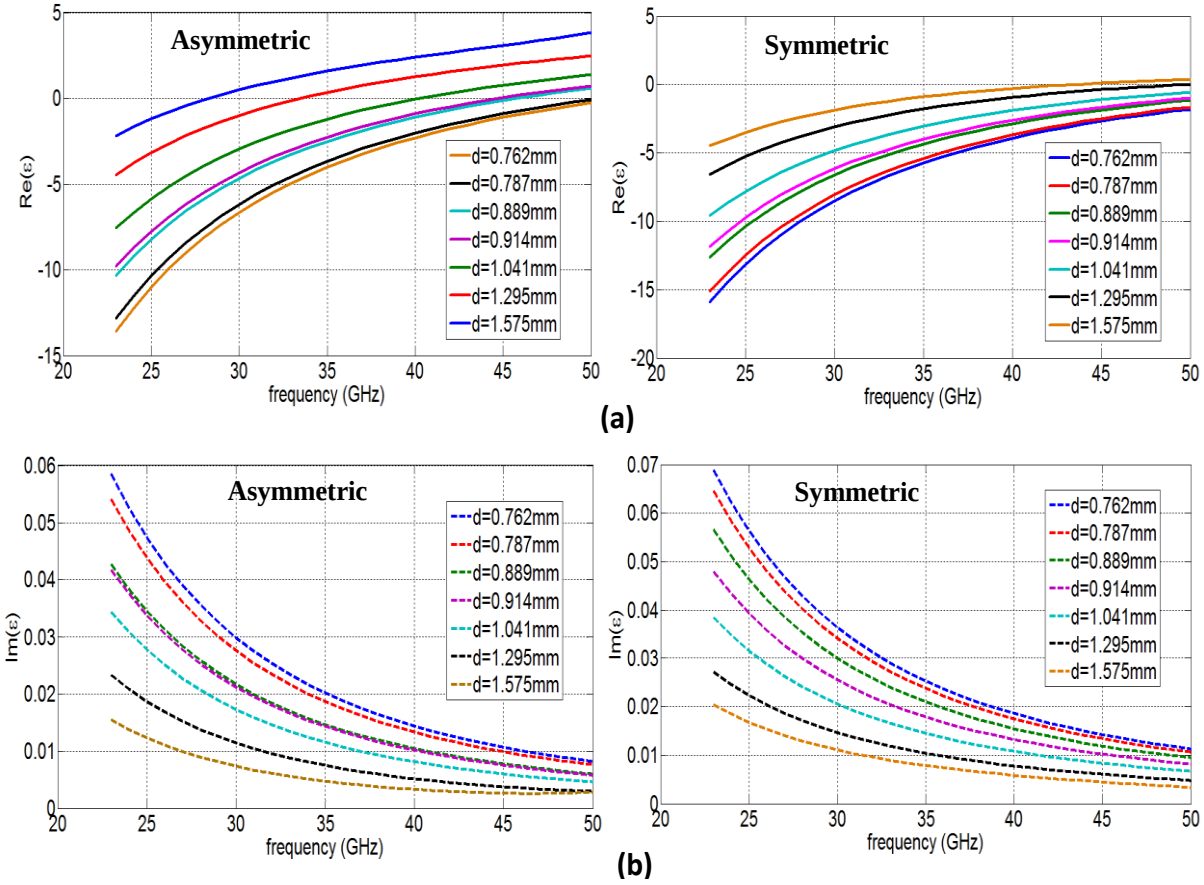

Figure 2-17: Effective permittivity ε of the symmetric and asymmetric structures for different values of *d* (a) Real part (b) Imaginary part.

From figure 2-17, it can be seen that the plasma frequency shifts to lower values when *d* increase. The plasma frequency shift in is not surprising, as there is likely an interaction between the substrate and the conductor that leads to somewhat different material properties depending on their relative positions.

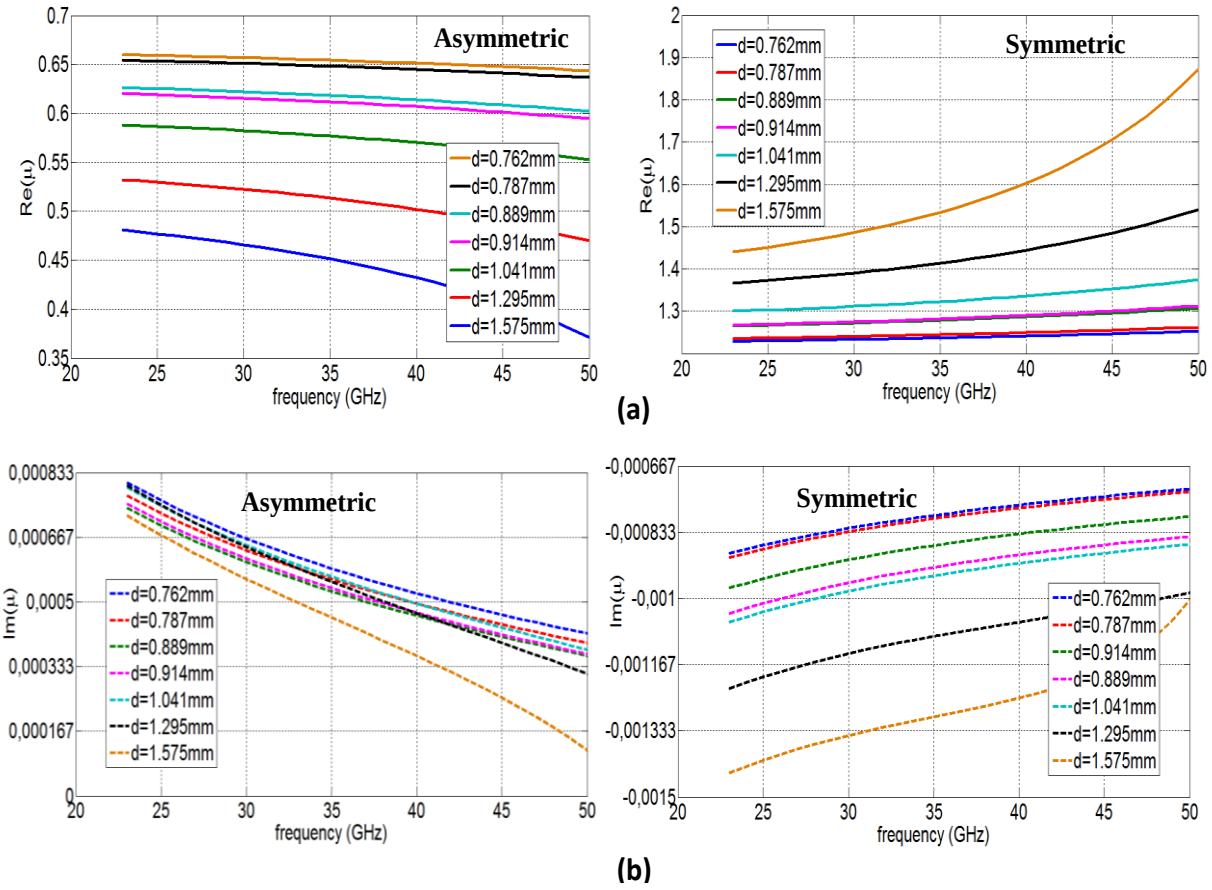

Figure 2-18: Effective permeability μ of the symmetric and asymmetric structures for different values of *d* (a) real part (b) imaginary part.

We note in figure 2-18 a great contrast in the permeability between the symmetric and asymmetric structures. As we know a straight current carrying conductor produces circular magnetic field lines around itself at all points along its length. The direction of rotation of this magnetic field depends upon the direction of current flow through the conductor, the "*left hand*" rule.

The real part of permeability in the symmetric unit cell is greater than in the asymmetric cell. Due to the magnetic field lines in the symmetric structure are more than number and intensity of which are in the asymmetric structure as shown in figure 2-19.

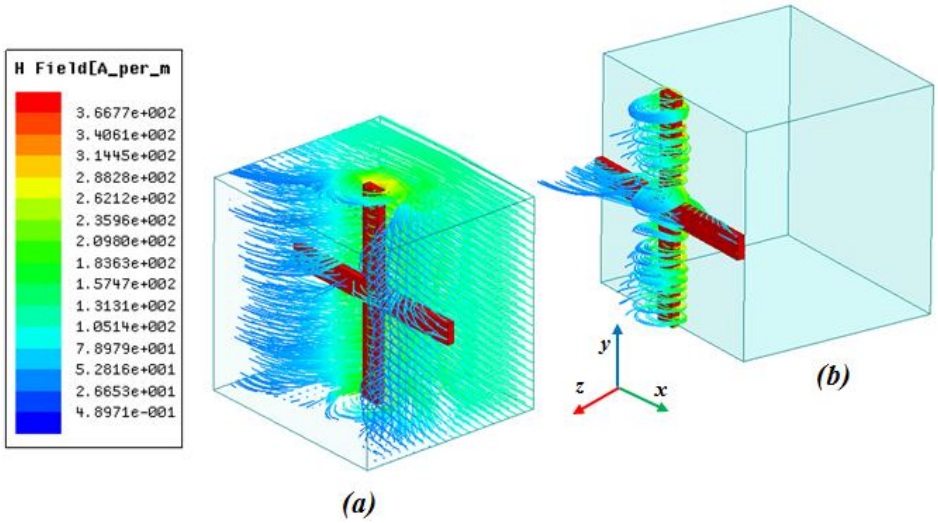

Figure 2-19: Pattern of magnetic field lines around a conductor in (a)-Symmetric unit cell (b)-Asymmetric unit cell.

The refractive properties of the two structures are very similar. The refractive index is nearly the same for the two structures, as it can be seen in figure 2-16. From figure 2-12, it is clear that the magnitude of S_{11} and S_{22} for the two structures are very close. However, their phases are very different. The position of the cross within the dielectric slab affects the S_{ij} parameters phase, which lead to great difference between the backward and the forward impedances of the asymmetric structure as shown in figure 2-14 and 2-16.

The imaginary parts ε'', μ'' and n'' account for losses in the structure caused by the electric and magnetic damping and the finite conductivity of conductors. Note that ε'', μ'' and n'' must be positive in a passive medium due to the conservation of energy [72].

Due to their passive nature, we observe from figure 2-16, 2-17, and 2-18 that the constitutive parameters (permeability, permittivity and refractive index) of the symmetric and asymmetric unit cells have positive imaginary parts. Except for the symmetric unit cell which presents a permeability with a negative but very close to zero imaginary part.

2.4.3 Transition from the symmetric to the asymmetric unit cell

The passage from the symmetric to the asymmetric unit cell is shown in figure 2-20, which represent the different positions of the cross like conductor in the dielectric slab.

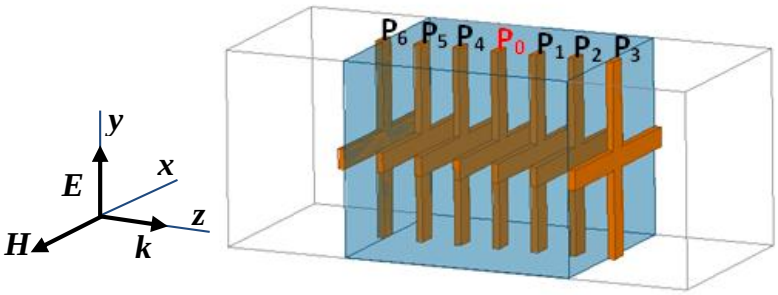

Figure 2-20: different positions of the conductor.

Figure 2-21-(a-b) shows the results for the magnetoelectric coupling parameter ζ and the effective permittivity when we shift the conductor from position P_0 to P_3 and from P_0 to P_6

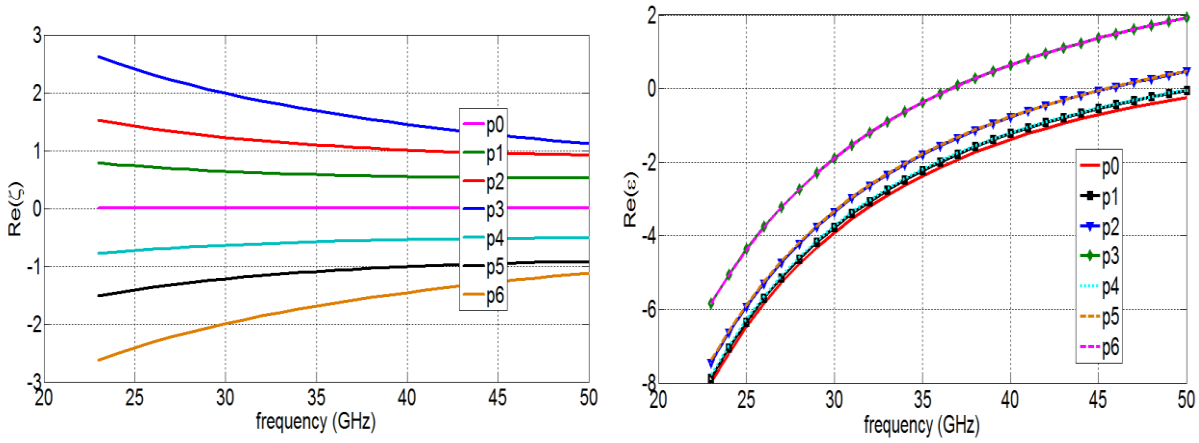

(a) **(b)**

Figure 2-21: Results for (a)-real magnetoelectric coupling parameter ζ (b)-real permittivity for different values of positions *P*.

From figure 2-21-b, we note that the plasma frequency shifts to the lower frequencies range when the conductor cross position shift away from the center (P_0). The shift in the plasma frequency depends only on the distance between the conducting strip position and the center of the dielectric slab (P_0). And is independent from the shift direction (backward or forward). Hence, for positions which are symmetric to the medium position P_0, such as P_1 and P_4, P_2 and P_5, P_3 and P_6, the unit cell has the same behavior: It presents the same plasma frequency and the forward and backward impedances are equal. For the central position P_0, which correspond the symmetric unit cell, the magnetoelectric coupling coefficient is null as it can be seen in figure 2-21-a.

The symmetric and asymmetric unit cells have the same refractive index, as is clearly shown in figure 2-16. From the point view of fabrication process, it is clear that the

asymmetric structure with the conductor cross printed in the top face of a printed circuit board, is easier to fabricate. For this reason, we have chosen to use in our design the asymmetric unit cell.

As it can be seen in figure 2-13, 2-14, 2-16, 2-17, and 2-18, that for $d = 0.914$ mm the metamaterial presents a plasma frequency close to 43 *GHz* which correspond to our antenna operating frequency.

2.5 Conclusion

Homogenization theories are typically valid when the unit-cell size is much small compared to the wavelength.

To extract the electromagnetic properties of metamaterials two methods have been applied. The first one based on *S*-parameter which is suitable to be applied for both numerical simulation and experimental measurements. The second one is based on the electromagnetic field distribution within the unit cell (field cards). It is known as the field summation method. We have compared each method with different published litterateur. From the comparison, we note that the field summation and *S*- parameters extraction methods are in good agreement comparing to the published litterateur.

3. Agile and programmable metamaterial

3.1 Introduction

This chapter gives a comprehensive review of the agility concept in microwave system design in general and antenna field in particular.

Agile antennas can be classified into three categories: i) frequency agile antennas, for which we can modify the operating frequency of antenna, ii) radiation pattern agile antennas, for which we can change their radiation pattern characteristics (pointing direction, main lobe beamwidth, etc.), and iii) polarization agile antenna, for which we can change the polarization. In this study, we are interested in antenna's radiation pattern agility. The aim is to steer the radiation pattern using a lens based on an agile metamaterial (programmable), which have two different behaviors: the first one where the metamaterial behaves like an effective medium with a refraction index n_1 higher than the unity, for the second one the metamaterial behaves like an effective medium with a positive and close to zero refraction index n_2.

Active devices such as PIN diodes, varactor diodes, and MEMS have been used in many novel designs for agility purpose. Other techniques have also been used such as controlling the unit cell characteristics using a liquid crystal as will be discussed later.

3.2 Agile antennas

The term of agile antennas is referred to any radiation structure in which either one or some of its fundamental operating characteristics are controlled by means of electrical or mechanical approaches. Indeed, the key principle in designing these antennas are based on the theory of conventional antennas, and by tailoring the radiator structure, controlling the current distribution, or changing the electrical parameters of the antenna, their desired radiation characteristics are tuned.

Agile antennas are able to independently alter their operating frequency, bandwidth, polarization, and radiation pattern to accommodate changing operating requirements. For instance, the ability to tune the frequency could be utilized to change the operating band filter out the interfering signals, or tune the antenna to account for new environments [73]. On the other hand, the polarization of the antenna can be reconfigured to separate or distinguish desired signals and hence forming a space filter for the unwanted signals [74],[76]. In addition, radiation-pattern agility can also be used as a space filtering or effectively send the

signals to a desired direction [77-78]. This increases the sensitivity of the receiver or the maximum transmitting range of the system.

Changing more than one property of the antenna at the same time is another feature that is highly demanded in the modem communication systems [79-80-81]. However, the reconfiguration on one property, for instance frequency, has direct consequence on the radiation pattern. Likewise, reconfiguration that results in radiation-pattern will also alter the frequency response of antennas. This linkage is one of the largest challenges faced by reconfigurable antenna developers who would usually prefer the characteristics to be separable. This research topic is called "compound antennas agility" which can also be classified as multi-functional antennas.

In this chapter, three fundamentals of antenna agility are described in more details witch are: frequency agile antennas, polarization agile antennas, and radiation pattern agile antennas.

3.2.1 Frequency agile antennas

In modem communication systems, different operating bands are required to perform the relevant tasks. Therefore, in except of using one antenna for each task, a dynamic frequency antenna can be applied to carry out all functions. This also reduces the system cost and may increase its overall performances. The frequency agile antenna is the only candidate that can be used to meet the system requirements. In these types of antennas, since the size relative to the wavelength is kept constant, almost the same characteristics are obtained by changing the frequency.

The antenna frequency alterations can be performed continuously or discontinuously (by means of switch). By using continuous variation, the frequency of the antenna can be reconfigured smoothly over a specific frequency range; while, for discontinuous cases, reconfiguration is realized by switching between different frequencies. The main difference between these two methods is the means that are used to change the effective electrical length or current distribution of the antenna. Electrical or mechanical switch including optical switches, PIN-Diodes, FETs, and radio-frequency micro-machined (RF-MEMS) switches are some kind of methods classified as discontinuous frequency reconfigurable approaches. Mechanically changing the antenna structure and material properties are other approaches, which can continuously change the frequency of the antenna. However, each method has its

own advantages and drawbacks and is chosen according to their potentials for the desired application.

3.2.2 Polarization agile antennas

A polarization-agile antenna is a type of antenna the polarization state of which can be changed dynamically, i.e., it can have either linear (vertical or horizontal) or circular polarization (left hand or right hand), depending on the requirements of its specific application. This special characteristic offers great flexibility for antenna systems, because a single antenna could be used to satisfy the different requirements of several systems.

Agile polarization is, potentially, able to introduce immunity to the interfering signals in unpredictable environments as well as creating an additional degree of freedom to enhance link quality by means of antenna diversity. Basically, the direction of the current distribution on the antenna dictates the polarization of the radiated electric fields in the far zone regions. Therefore, the polarization agile reconfiguration is realized by managing the direction of the current distribution usually by changing the antenna structure, material properties, and/or feed configuration. However, it is important to maintain an efficient polarization reconfiguration while keeping the desired radiation pattern and matching. This is because by changing the polarization, other antenna radiation characteristics may significantly change. This is the main consideration point in designing this type of reconfiguration property. Although, the key principle of polarization diversity is similar to the one of frequency diversity, the available reported research shows that the switching methods are the most popular approach for polarization reconfigurations.

3.2.3 Agile radiation pattern antenna

Agile radiation pattern is another interesting topic in the antennas agility, which is usually used as space filtering for increasing the link quality by effectively focusing the radiated signals to the desired direction (figure 3-2). This can be achieved even by changing the amplitude and phase of the electric or magnetic currents on the structure. However, because of changing in the current distribution, it is expected to have some variation in the frequency response of the antenna as well. This is the main technical point that should be considered in the design process to minimize the effect of pattern/gain reconfiguration on the frequency response and hence matching bandwidth.

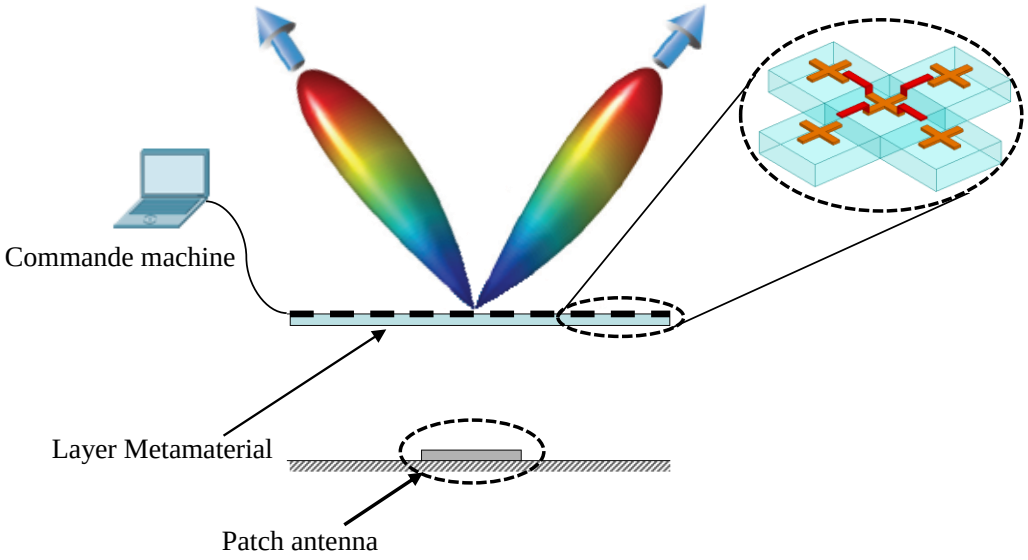

Figure 3-1: Agile antenna.

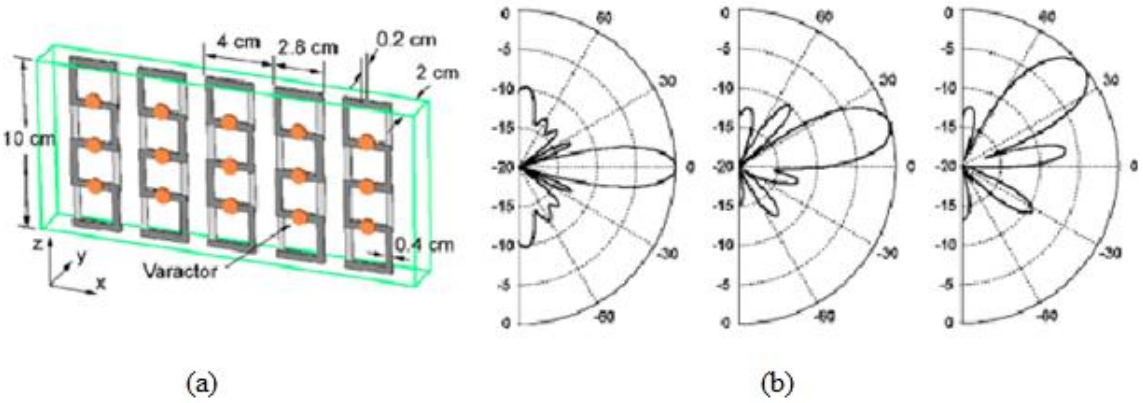

Figure 3-2: (a)-S-ring structure loaded with varactores (b)-normalized radiation patterns gain control [82].

Depending on the antenna structure, frequency of operation, and fabrication technology, different types of tunable approaches have been proposed for agile radiation pattern. For instance, structural changing by means of electrical or mechanical actuators is one of approaches in changing the radiation-pattern shape. As an electrical method, MEMS switches have been applied into the antenna structure to change the current distribution and therefore its radiation-pattern [75],[83]. Similar to the frequency reconfiguration, controlling material properties is another method that has been suggested to manage the radiation-pattern. However, applying this method, especially using ferromagnetic materials, introduces the main constraints of losses, higher cross polarization, being bulk and needing a particular biasing structure [84-85]. Using parasitic elements around the primary antenna is another approach, which has been proposed to change the direction of the radiation-pattern. This method

possesses attractive qualities, including isolation from the driven element, potentially wide frequency bandwidth, and a range of available topologies and functionalities [86- 87]. In one other approach, the pattern reconfiguration can be achieved by an array of tunable elements in which phase of each element can be adjusted to focus the radiated energy in a particular direction [88]. As it can be deduced, in all radiation-pattern reconfiguration mechanism, by tailoring the antenna structure to different shapes or by changing the electrical parameters of the antenna structural embodiment, the radiation-pattern is reconfigured. In the next sub-section, some of the commonly used reconfiguration mechanisms are described.

3.3 Agility techniques

Several studies show that agility can usually be achieved by means of mechanical or electrical approaches [80]. In the mechanical methods, the structure of the radiator is moved by electromechanical actuators in order to reshape the antenna structure. Piezo-electric actuators, see figure 3-3, or micro-machined plastic deformation are some kinds of recently proposed methods to achieve the frequency and radiation-pattern agility. These methods deliver a wide range of operation frequencies limited by the practical constraints. Agility can continuously sweeps the desired property through a bandwidth or switches between different regimes. In addition, it provides low loss, linear behavior at high frequencies, which are remarkable merits to attenuate the inter-modulation (IMD) harmonic problem. However, needing to a specific complex actuation system and being low speed are the main drawbacks of this approach.

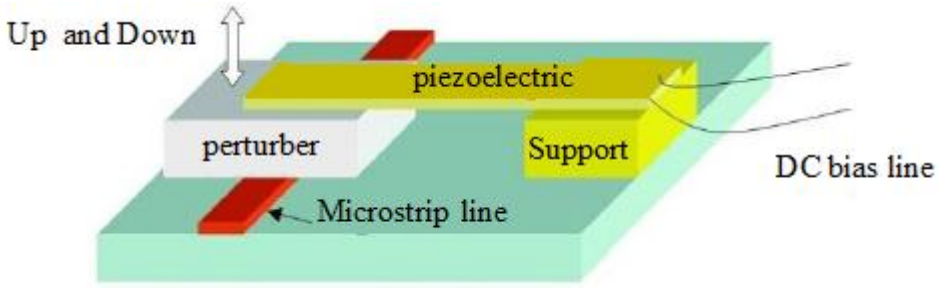

Figure 3-3: Piezoelectric actuators.

On the other hand, in the electrical methods there is no any movement in the configuration and the changes in the overall shape is electronically achieved. Indeed, this is realized by connecting/disconnecting different parts of the structure, changing the elements of the equivalent electrical circuit model of the antenna via variable capacitors or by changing the material properties. Optical switches, high frequency PIN-Diodes (figure 3-4), FETs, and radio frequency micro-mechanical switches (MEMS) (figure 3-5) are some kinds of

commonly used means applied to connect or disconnect different parts of the antenna. These components are applicable to reconfigure frequency, polarization, or radiation pattern.

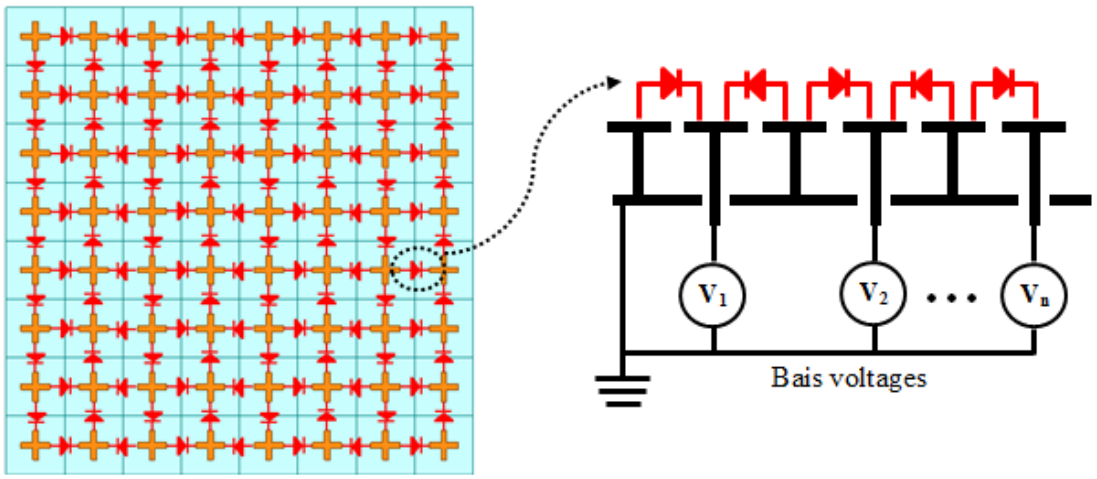

Figure 3-4: Electrically tunable surface, with varactor diodes.

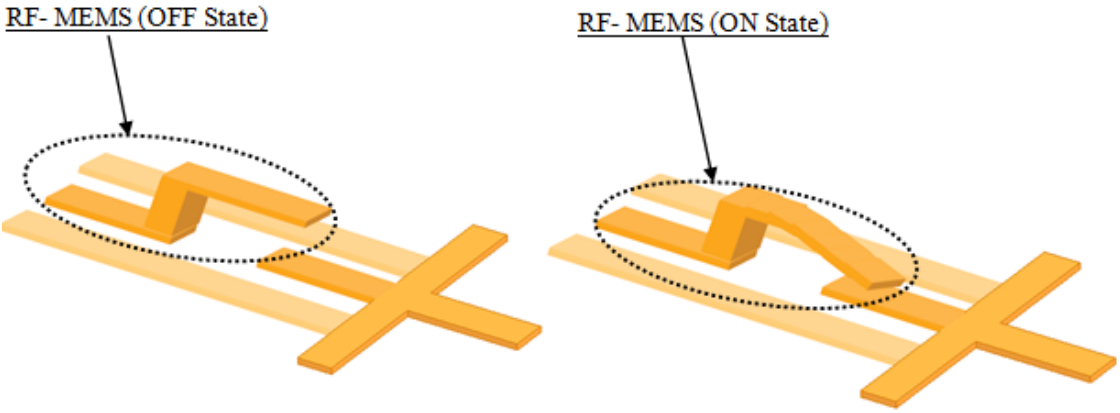

Figure 3-5: RF-MEMS ON and OFF states.

The variable capacitors are other components that are usually used to continuously reconfigure the frequency response of the antenna over a specific bandwidth. This can be realized by chip variable capacitors integrated into the structure. These capacitors are usually based on the semiconductor or MEM technologies. However, because of packaging parasitic elements and losses, the application of these components is limited, especially for the components based on the semiconductor technologies.

Changing the material properties is another interesting approach, which mainly is applied to reconfigure the radiation-pattern and frequency response [89-90]. Liquid crystals (LC), ferroelectric and ferromagnetic materials are some kind of these materials, which have been utilized as means of agility. In these methods, by applying a DC voltage or magnetic field, the electrical properties of the dielectrics are changed, leading to alter the EM response of the

structure. Ferromagnetic materials and LCs are bulkier and create more losses than ferroelectric materials. Moreover, creating higher cross polarization level in ferromagnetic is another reason to not widely apply these materials directly as radiators in the antenna applications.

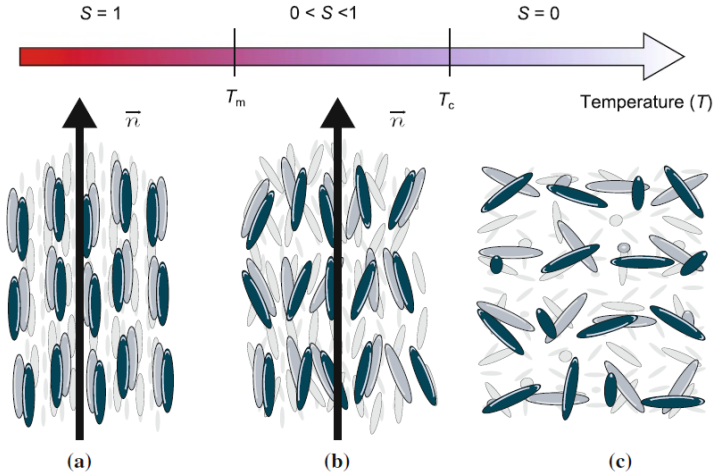

Figure 3-6: Schematic of a nematic liquid crystal material depending on the temperature (a)-Crystalline solid state with perfect alignment (b)-Nematic phase (c)-Liquid phase.

Figure 3-6 shows the schematic representation of a nematic liquid crystal. In an LC bulk, the molecules are aligned parallel to their long axes because of the shape anisotropy. In the macroscopic scale, the time-averaged direction of the molecules is denoted by a director $\vec{n}$, which is along the long axes of the molecules. Such a preferred direction is not defined for the short axes since the nematic liquid crystals are usually uniaxial [91]. In the both solid and nematic phases, a director can be assigned whereas the level of molecular ordering is different. This is quantitatively defined by an order parameter S [92]. At temperature T_c, so called the clearing point, the transition into the liquid phase occurs and the opacity clears. A well-known commercially available LC is 5CB1, which is frequently used in the LC display applications.

The arrangement of the LC molecules in a bulk is determine quantitatively by using the order parameter S [93]. Figure 3-7 shows a snapshot of a single rod-like shape LC molecule. The single molecule points in $\vec{u}$ direction at the moment of observation and the director is parallel to the z axis. This means that the average direction of the molecules is in the z direction or the molecules spend more time when pointing in the z direction than other directions [94].

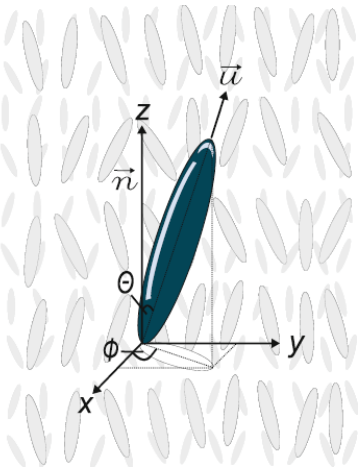

Figure 3-7: The coordinate system for a single liquid crystal molecule.

In summary, the above mentioned agility technical has been compared in different technical standpoints in table 3-1.

Table 3-1: Comparison of different reconfigurable approaches.

	Technology	Bias	Speed	IMD
Semiconductors	Schottky (GaAs)	< 5V	< 1 ns	Poor
	HBV(GaAs)	< 20 V	< 5 ns	Poor
	Abrupt p-n junction (Si)	< 30 V	< 10 ns	Poor
	PIN-Diode	< 10 V	< 1μs	Poor
Magnetic	YIG (Variable Permeability ferromagnetic resonance)	current (Coil)	< 5 ms	-
	Remnant magnetization	current (Coil)	< 5 ms	-
	Magneto-static (spin) wave	-	< 5 ms	-
Ferroelectric	Thin film	< 30 V	< 1 ns	Low
	Thick film	< 1000 V	< 10 ns	Low
	Bulk	< I5KV	< 1 μs	Low
Liquid crystal	Cavity/Bulk	< 40 V	< 10 ms	-
Optical	Photoconductivity	current (LD,LED)	10 fs-10 ms	-
Mechanical	MEM Varactor	< 50 V	> 10 μs	Excellent
	Piezo-transduce	> 100V	> 100 μs	Good

Based on the data listed in this table, it can be conclude that implementing the reconfiguration structure by means of MEM technology proposes better performances in terms of loss, speed, power consumption, and more important IMD level. It can be observed form this table that ferroelectric materials may ranks as the second approaches to implement a high speed, low loss reconfigurable structure with low IMD level. However, the practical

limitations, operating frequencies, and technology constraints restrict the designer to choose a specific reconfiguration mechanism for the desired applications.

3.4 Agile antennas and their practical issues

The technical advantages offered by agile antennas have introduced them as potential candidates for multi-function or smart communication systems. Therefore, they have found a myriad of applications in different areas including satellite communications, base stations, wireless sensors, and medical areas. Moreover, by growing different technologies to develop agile materials, for instance, high frequency semi-conductor switches and capacitors, micro electromechanical systems (MEMS) [95], ferroelectric materials [84],[98], liquid crystals [96], and most recently plasma materials [97], they are getting more interest for the future modem communication systems.

However, there are still some practical issues that may limit or pose some constraints on the applications of these antennas. In many cases, the selected antenna topology and intended applications restrict the choice of reconfiguration mechanism and some tradeoffs need to be considered. Those trade-offs may include, reconfiguration speed, power consumption, actuation requirements (voltage or current), fabrication complexity, durability, device lifetime, complexity of control and bias networks, weight, size, cost, dynamic range, sensitivity, and, of course, overall performance of antenna system.

3.5 Agile and programmable metamaterial

In this section, we design an agile planar metamaterial which can be controlled by an external command system. This agile unit cell is composed of a cross type conductor of width *w* and metallic thickness *t* printed on a dielectric slab of thickness *d*. The ends of the cross type conductor are all interrupted with a small gap as shown in figure 3-8. The cross type conductor of each unit cell is connected to its four neighbors by four switches. If the switches are in the ON state the metamaterial behavior like a connected cross type metamaterial, and like a disconnected cross type metamaterial otherwise (switch OFF).

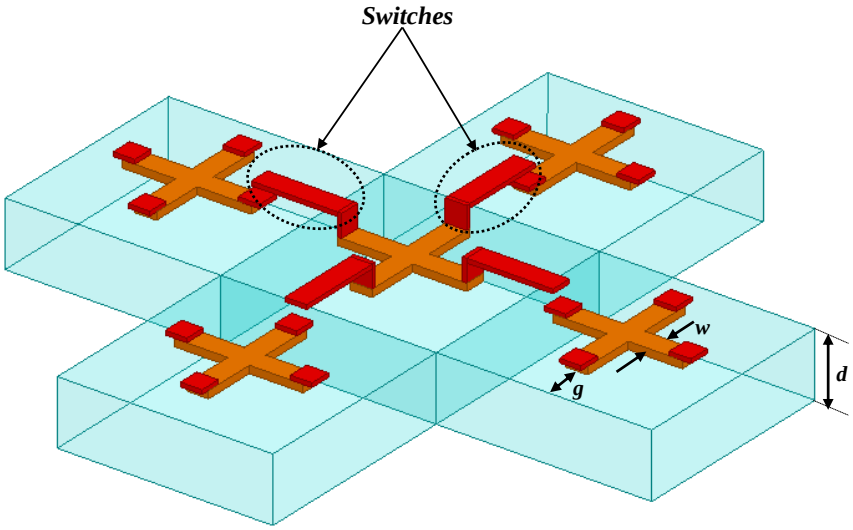

Figure 3-8: Agile unit cell.

We have designed a metamaterial unit cell which has two different behaviors according to the switch state (ON or OFF). This agile metamaterial unit cell allows us to obtain an agile planar metamaterial surface, where each unit cell can be controlled individually. In this agile metamaterial surface, we can program zones of different shapes and sizes to have the desired refraction index n_1, or n_2, see figure 3-9.

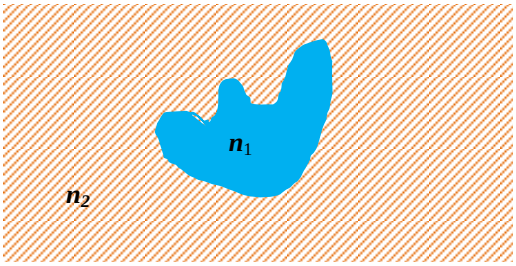

Figure 3-9: Agile lens with two different refraction indexes n_1 and n_2.

Finally we use this agile metamaterial surface to design an agile electromagnetic lens, which can be used as a superstrate above a microstrip antenna to enhance the antenna gain and control the radiation pattern.

3.5.1 The agile metamaterial surface

The elementary cell of our agile metamaterial is sketched in figure 3-10. It is made of disconnected cross-like conducting strips, printed on a dielectric substrate. The disconnected branches of the cross can be joined with switching devices such as diodes, MEMs, etc. According to switch states (ON or OFF), the unit cell has two different commutable behaviors. The first one corresponds to the disconnected cross type (switch OFF) and behaves like an effective medium with a refraction index n_1 higher than unity. The second one

corresponds to the connected cross type (switch ON) and has a positive and close to zero refraction index n_2. The actionable behavior of our unit cell allows us to introduce the metamaterial agility.

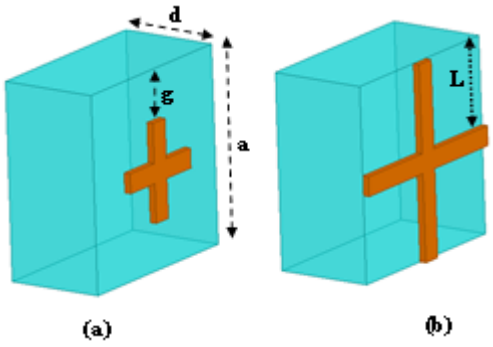

Figure 3-10: Agile metamaterial elementary cell (a) disconnected cross (b) connected cross

The agile metamaterial elementary motifs are printed on a dielectric substrate of permittivity $\varepsilon_r = 2.2$ and with dielectric loss tangent around 0.0027,the metallization thickness is 0.035 mm the operating frequency is 40 GHz hence the corresponding wavelength in free space is 7.5 mm. We have seen in Chapter 2, the greatest dimension of the metamaterial unit cell must be much lower than the operating wavelength, to respect the homogenization conditions, we fixed the period by a = 1 mm.

3.5.2 The agile metamaterial lens

We use the programmable metamaterial to design the grids of the agile lens as shown in figure 3-11. These grids are made up of two regions; the first one forms a focusing zone (FZ) and the second one, the lens body (host medium). The refraction index (n_1 or n_2), the size, shape and position of the FZ can be programmed by acting on the switching devices (state ON or OFF). Modifying the FZ parameters (size, shape, position, and refraction index), allows us to control the antenna radiation pattern properties, main lobe direction (pointing angle) and beam-width in both E- and H-planes.

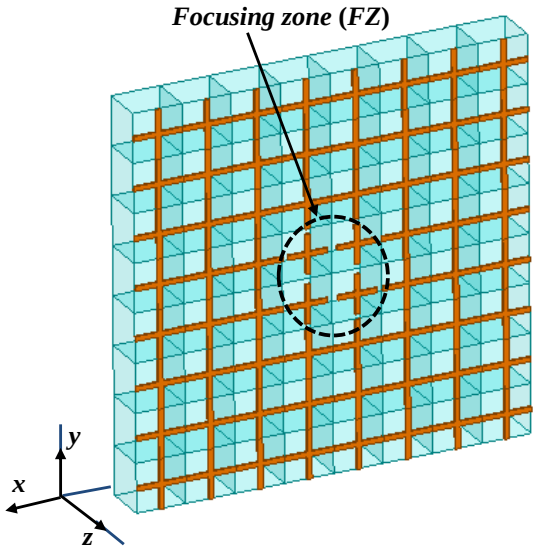

Figure 3-11: Agile lens grid.

The conducting strip width *w*, the gap size *g* and many other factors, such as the metallization thickness *t*, the substrate permittivity ε_r and the thickness *d*, directly govern the agile metamaterial electromagnetic properties. Since we have fixed some of them (t, ε_r, and *a*) we use *w*, *g*, and *d* as the design parameters to tune the agile metamaterial unit cell behaviors.

3.5.3 The influence of the conducting strip width

In this section we investigate the influence of the conducting strip width *w* in the electromagnetic properties of the agile metamaterial based on connected cross. First, from figure 3-10 we fixed the substrate thickness at *d* = 0.914 mm to ensure a plasma frequency of 43 GHz, which is within our antenna operating frequency range. We vary the conductor width *w* from 0.1 mm to 0.4 mm.

The simulations are obtained by a finite element method based commercial simulation code. The results of the magnetoelectric coupling coefficient ζ, permittivity ε, permeability μ, and refractive index *n*, for different values of the conducting strip width *w* are shown in figure 3-12 and 3-13.

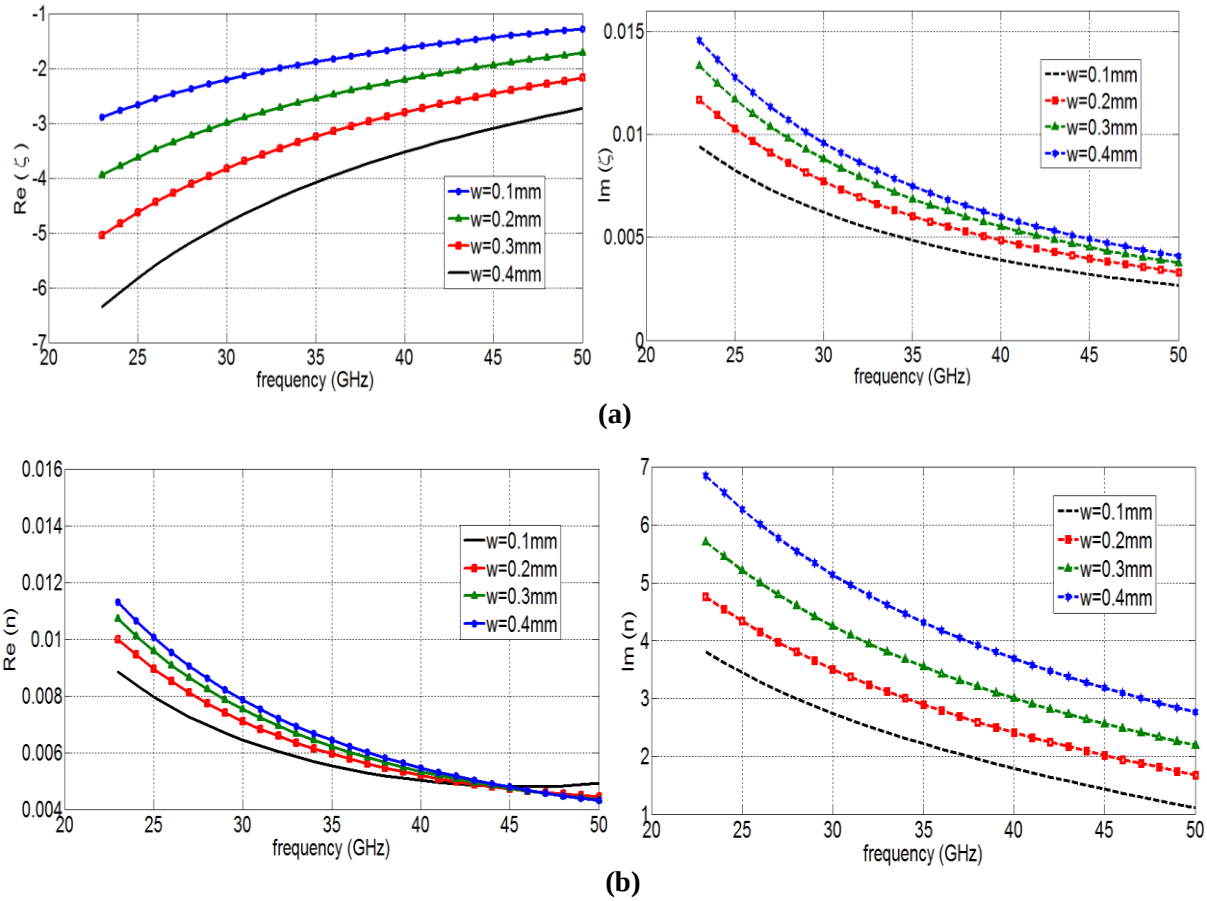

Figure 3-12: Real and imaginary parts of (a)-magnetoelectric coupling coefficient ζ (b)-refractive index *n*, for different values of *w*.

The imaginary part of the magneto-electric coupling coefficients in figure 3-12-(a) shows a different behavior when we increase the width over the 23–50 GHz band, this difference comes from the relative position of the cross-conductor with respect to the orientation of the incoming wave.

It can be seen from figure 3-12-(b) that the real part of the refractive index *n* in the connected cross type metamaterial is positive. The imaginary part of index *n* is greater than zero for almost all analyzed frequencies.

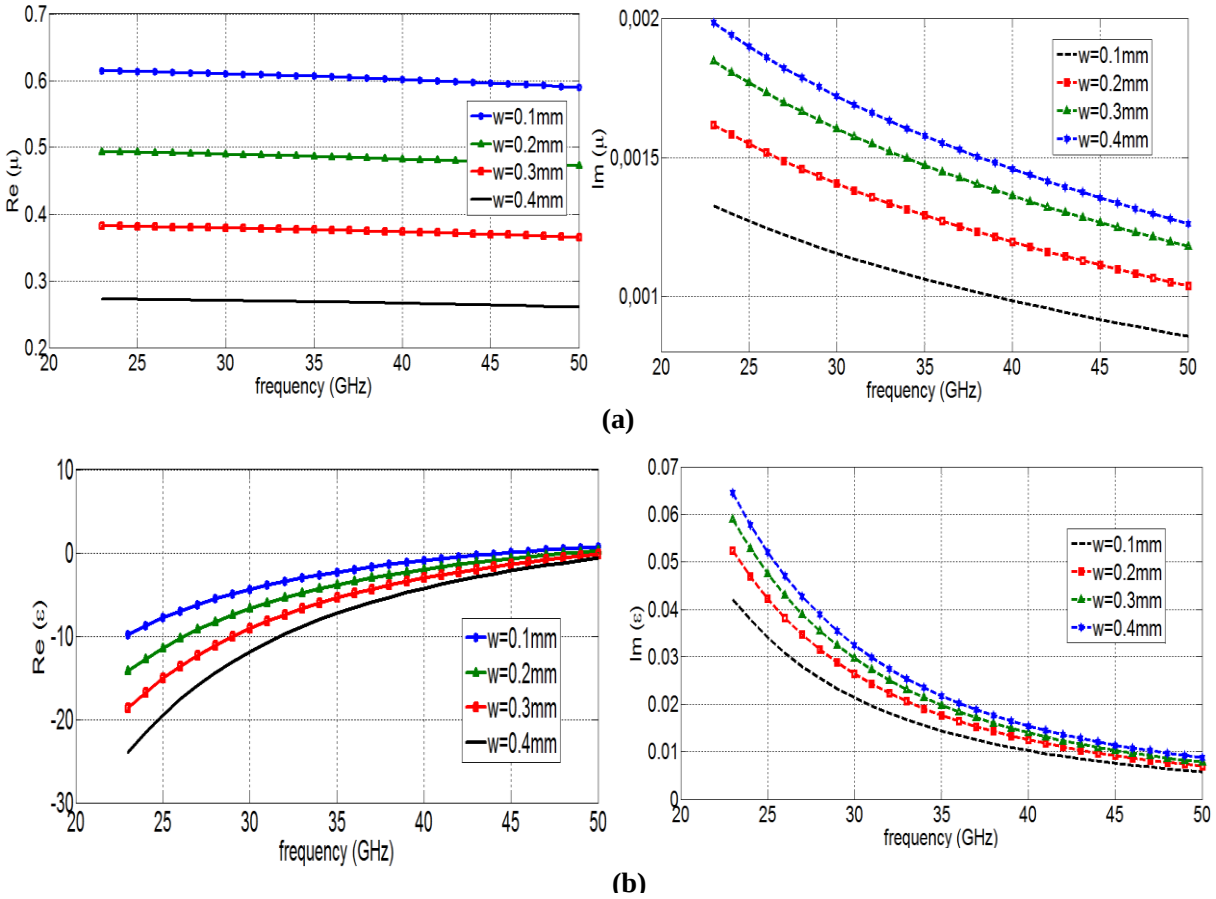

Figure 3-13: Real and imaginary parts of (a)-permittivity ε (b)-permeability μ, for different values of the conductor width *w*.

The plasma frequency in figure 3-13-(b) with the optimized permittivity value, occurs around 42-45 GHz, the relative permittivity stays between 0 and 1 it can be seen also that for w = 0.1 mm the metamaterials present a plasma frequency equal or a little less than 43 GHz and very low real part (close to zero) in the operating frequency range (40-45 GHz).

The imaginary parts of the constitutive parameters (ε and μ) are positive concordance with the Lorentz dispersion model and the uniqueness theorem for a passive medium [99-100-101].

3.5.4 Power analysis

In this section we are concerned with the power properties of the wave propagation in the forward and backward directions in the cross type metamaterial.

Figure 3-14 and 3-16, illustrate the effect of the conductor cross width on the reflected P_r, transmitted P_t, and absorbed P_a powers in the cross based metamaterial.

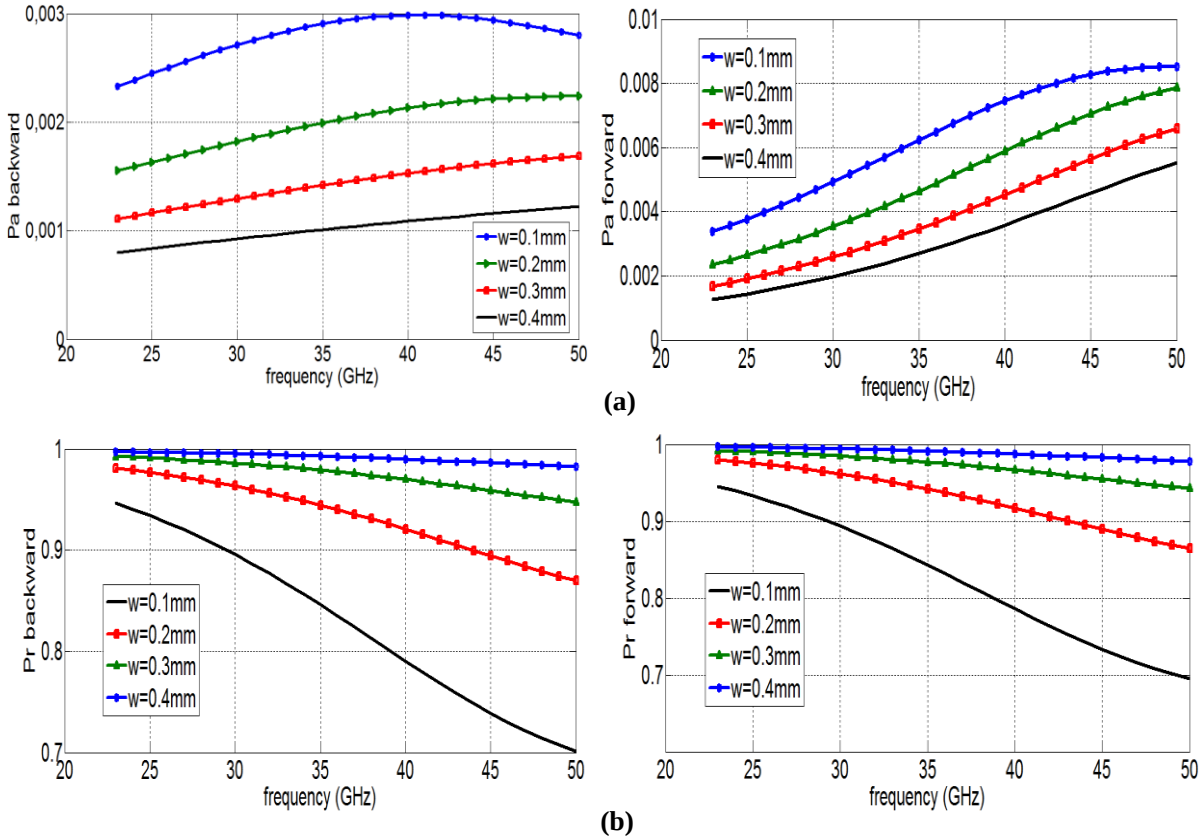

Figure 3-14: (a)-Absorbed powers in the backward P_a^-, and in the forward P_a^+(b)-Reflected powers in the backward P_r^- and in the forward directions P_r^+, for different values of w.

Figure 3-14-(a) shows that the absorbed powers in the metamaterial, corresponding to a wave propagation in the forward and backward directions; are slightly different and decrease when we increase the conducting strip width w. This difference comes from the reflection asymmetry ($S_{11} \neq S_{22}$). For example, in figure 3-14-(a) we observe that the maximum absorbed power in the backward direction, corresponding to w = 0.1 mm, is in the order of 0.3 %, while it is about 0.8 % in the forward direction. The absorbed power in the forward direction is always greater than in the backward direction. Indeed, for the asymmetric unit cell, the path of the reflected waves (the waves are almost reflected by the conductor strip) in the dielectric medium in the backward direction is longer than in the forward direction, as shown in figure 3-15.

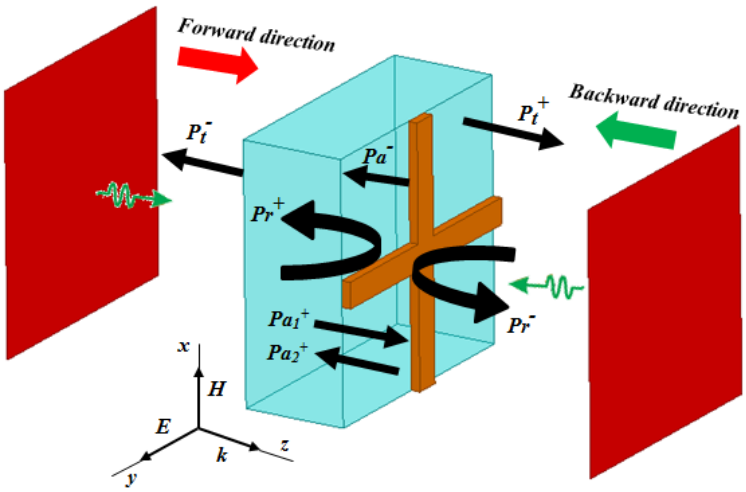

Figure 3-15: Powers in the backward and forward directions.

As expected, the reflected powers in both forward and backward directions increase when the conducting cross width increase, due to the increasing of the reflection surface. The reflected power is great then 90 % for $w > 0.2$ mm and less than 90 % for $w < 0.2$ mm.

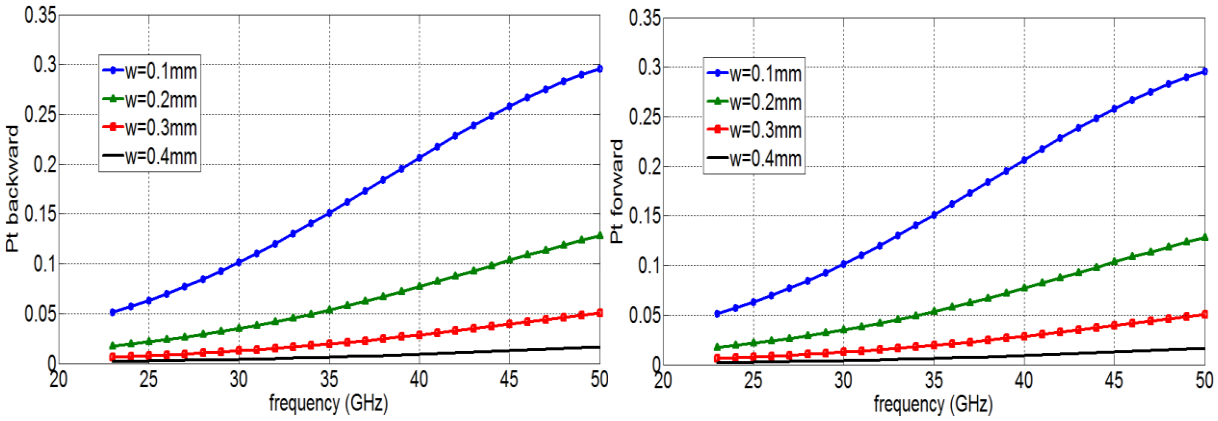

(a) **(b)**

Figure 3-16: Transmitted powers P_t (a)-backward direction (b)-forward direction, for different values of w.

The transmitted powers are the same in the two directions (forward and backward) as it can be seen in figure 3-16. Note also that for $w = 0.1$ mm, the transmitted power is maximum because the reflection surface and the reflected power are both minimum.

In our agile metamaterial lens design, we used to control the antenna radiation pattern we need to maximize the transmitted power. The conductor cross width is hence fixed to $w = 0.1$ mm.

Once the conductor strip width w is fixed, all the connected cross unit cell dimensions are known: dielectric permittivity $\varepsilon = 2.2$, substrate thickens $d = 0.914$ mm, and conductor width

w = 0.1 mm. The disconnected cross unit cell is identical to the connected cross except for the gap g which remains to be determined. To do this, g is varied in the simulation, to obtain the desired effective permeability and refraction index profiles.

3.5.5 The influence of the gap *g*

In this section we study the influence of the gap g on the disconnected cross type metamaterials. The choice of the gap g depends upon three conditions: The effective permeability must present a profile close to unity (no magnetic behavior) and the refraction index should present a profile as flat as possible corresponding to a low dispersive behavior and large contrast between the connected and disconnected cross type metamaterials, and finally a very low reflected power corresponding to a maximum transmitted power.

The simulation results of the electromagnetic properties of the disconnected cross for different values of the gap g are shown in figure 3-17 and 3-18.

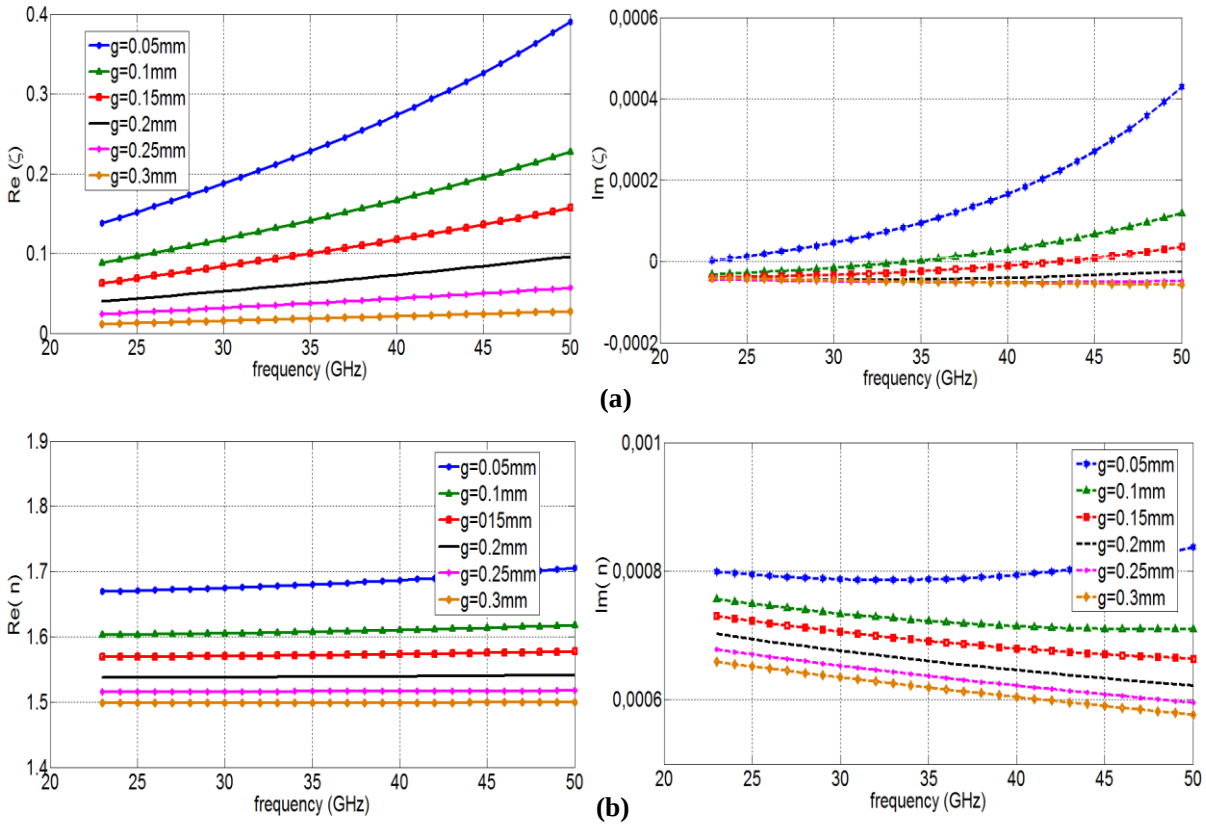

Figure 3-17: Simulation results of real and imaginary parts of (a)-magnetoelectric coupling coefficient ζ (b)-refractive index n, for different values of the gap g.

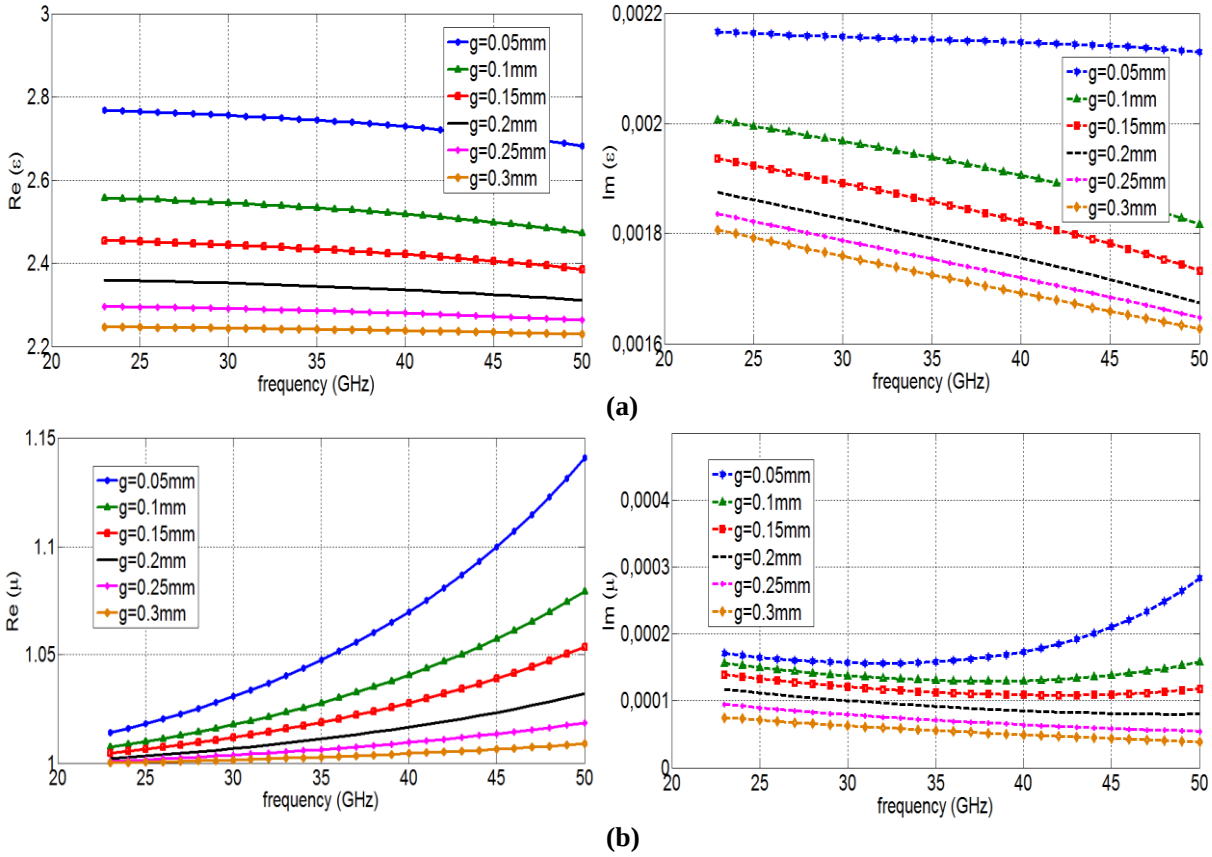

Figure 3-18: Real and imaginary parts of (a) permittivity ε (b)-permeability μ, for different values of g.

Figure 3-17 and 3-18 present the constitutive parameters and the refraction index of the disconnected ($g \neq 0$ mm) cross based metamaterial. We observe that the constitutive parameters and the refractive index decrease when the values of the gap increase. The maximum value of the refractive index is about 1.69 for $g = 0.05$ mm over the operating frequency range (40-50 GHz).

Figure 3-18-(a-b), shows that the constitutive parameters ε and μ have positive imaginary parts which account for losses in the effective medium. It can be seen also that the imaginary part of the permittivity is rather small for the connected cross type metamaterial compared with that of the disconnected cross type. This attests to the low loss nature of the disconnected cross type metamaterial.

Figure 3-19 and 3-20, illustrate the dependencies of reflected (P_r), absorbed (P_a), and transmitted (P_t) powers for different values of g.

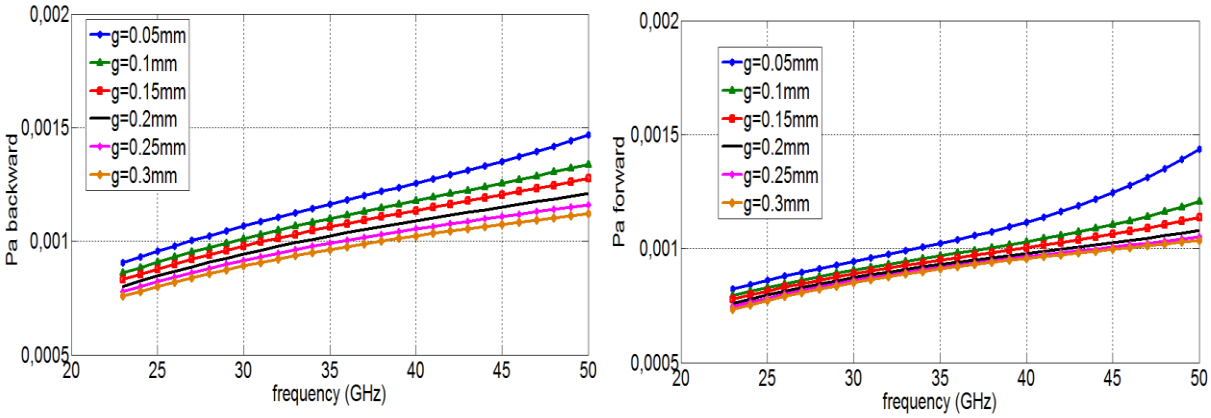

(a)

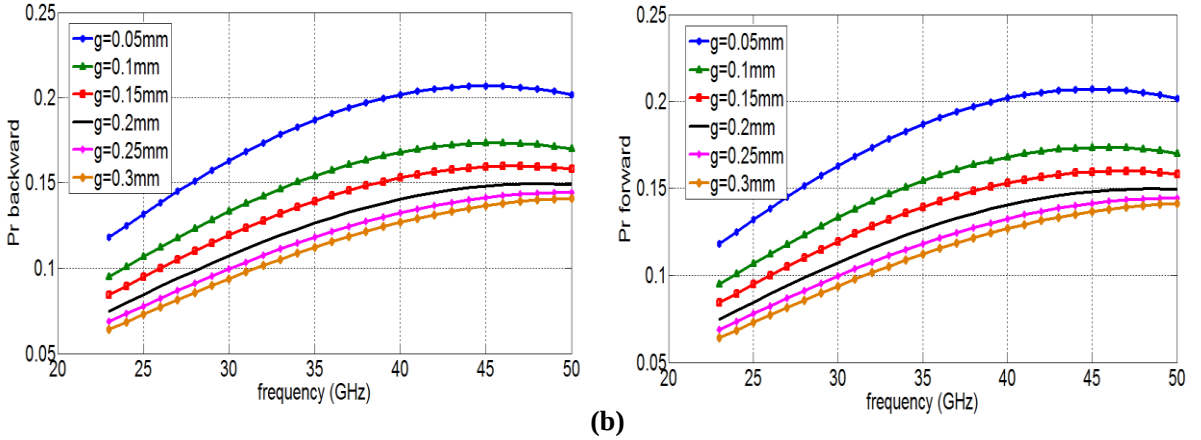

(b)

Figure 3-19: (a)-Absorbed powers in the backward P_a^- and in the forward P_a^+(b)-Reflected powers in the backward $P_r^-$and the forward P_r^+ directions, for different values of g.

We note from figure 3-19, that the maximal absorbed power is 0.15 % in the backward and 0.14 % in the forward for g = 0.05 mm. The reflected power decreases for g = 0.3 mm.

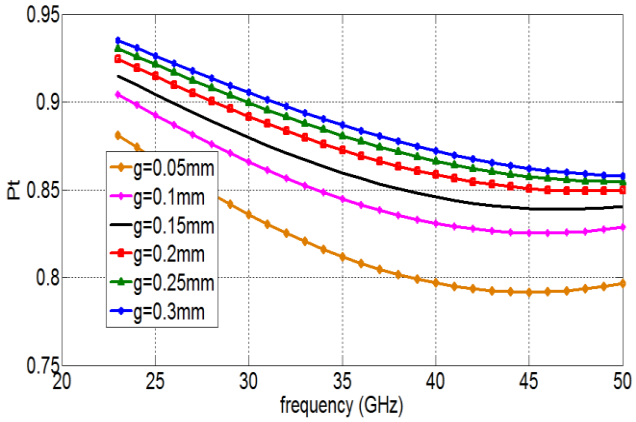

Figure 3-20: Transmitted power for different values of the gap g.

We observe from figure 3-20, that the maximum transmitted power corresponds to g = 0.3 mm is 88 % over 40-45 GHz. So we can fix the gap at g = 0.3 mm.

3.6 Conclusion

The research survey on the topic of agile antenna demonstrates that still this topic is in the developing period and more multi-disciplinary research considering both hardware and software level of the antenna system is demanded.

Agility technical such as localized elements like PIN diodes, varactor diodes or MEMS and agile materials like ferromagnetics, ferroelectrics, or liquid crystals (LC) enables to vary the medium index of the metamaterial within an interesting range.

The design and the characterization of agile metamaterial (programmable) type cross unit cell are proposed in order to create a superstrate for beam steering applications in small antennas.

4. Microstrip Antenna radiation pattern control using an agile metamaterial lens

4.1 Introduction

Among the most important metamaterial applications in the antenna field we can mention the antenna performance enhancement and size reduction [102-103]. However, the control of antenna characteristics remains a major challenge of metamaterial use in this domain.

The goal of this chapter is to control and steer the radiation pattern of a microstrip patch antennas using agile metamaterial lens. As presented in chapter 3, the agile metamaterial lens is constituted of two regions: the first one forms the lens body and the second one a focusing zone (FZ), the characteristics of which it is possible to change using an external control system.

The metamaterial lens is placed on the top of a microstrip antenna at a distance *h* from the patch. Two types of metamaterial lenses we will use to control the radiation pattern of the antenna: i) the first one is a planar lens formed by one or two agile metamateial planes, and ii) the second one is a spherical cap shape formed by the agile metamaterial surface. For each lenses type, there are two key factors to optimize to obtain better antenna gain and more radiation pattern steering. These are the radius *r* of the spherical cap shape, and the grids spacing in the *z*-axis direction for the planar one (the heights h_1 *and* h_2).

By modifying the FZ parameters one can control the patch antenna's radiation-pattern main-lobe beamwidth and direction (pointing angle) in E- and H-planes.

4.2 The agile metamaterial lenses configurations

The agile metamaterial unit cell is used to construct an agile metamaterial lens. As announced in the precedent section, in this work we will design two types of agile metamaterial lens: a planar and a spherical one (figure 4-1).

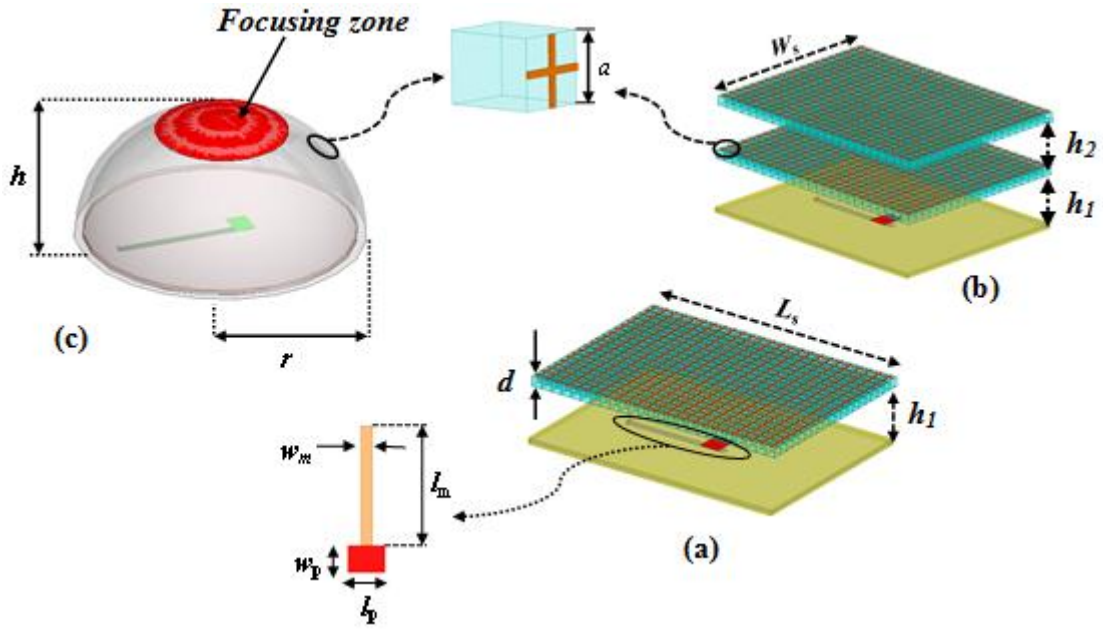

Figure 4-1: Patch antenna with metamaterial lens:(a)-single planar layer lens,(b)-double planar layer lens, (c)-spherical cap lens.

We start our metamaterial agile lens design by using a single or double rectangular planar grid above the antenna. In this configurations the lens has two weaknesses: i) the antenna is not at the same distance to the lens and specially to the focusing zone for all azimuthal angle θ see figure 4-2, and ii) the radiating structure presents a low mechanical stability. To overcome these two weaknesses, we design a new lens which has a shape of a spherical cap for which the lens is at the same distance to the antenna for all observation angles θ and presents a better mechanical stability.

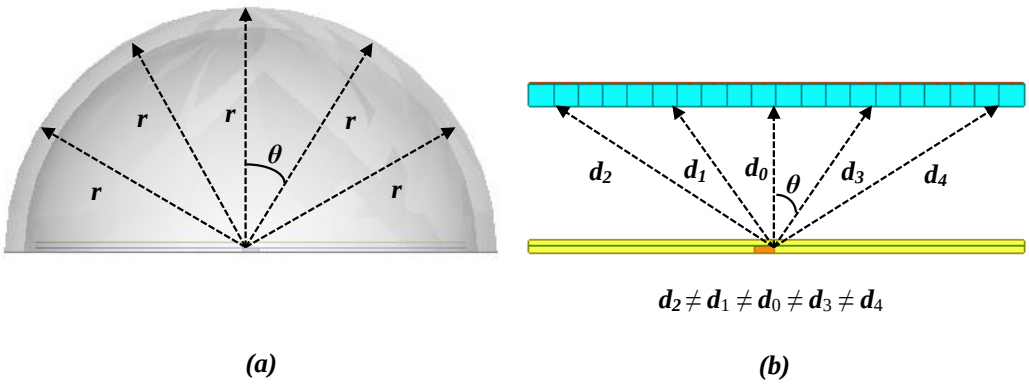

Figure 4-2: Distances between the antenna and the lens: (a)-spherical cap, (b)-planar layer.

4.3 Double Layer Superstrate (DLS) Metamaterial Lens

We have already use a double layer metamaterial superstrate (DLS) to enhance a microstrip antenna gain and directivity [104-105]. The metamaterial layer superstrate is composed of a

periodic arrangement of cross type unit cells and behaves as a zero refractive index medium. The zero index metamaterial (ZIM) based superstrate focuses the radiated waves in the direction normal to the superstrate and thereby enhances the antenna gain and directivity. Based on these results we will design double layer superstrate agile metamaterial lens using the agile cross type using cell. The perspective view of the proposed antenna with double layer superstrate is shown in figure 4-1 (b). The spacing from the patch to the bottom of the first layer of the superstrate is h_1 and from the top of the first layer to the bottom of the second layer is h_2. These two parameters (h_1 and h_2) have to be optimized to get the best gain and directivity. In this study we seek after the better combinations of metamaterials type constituting lens body. Table 4-1 and figure 4-3, summarizes the different possible combinations of materials for forming the lens body.

Table 4-1: The different combinations of the materials lens constitution.

lens grid	Metamaterials type	Cases
grid 1 and 2	Connected cross	Case 1
grid 1 and 2	Disconnected cross	Case2
grid 1	Connected cross	Case 3
grid 2	Disconnected cross	
grid 1	Disconnected cross	Case 4
grid 2	Connected cross	

The simulations are obtained by a finite element method based commercial simulation code. The results of all possible combinations for different values of h_1 and h_2 are shown in table 4-2. We can see from table 4-2, that the best antenna gain is obtained using the lens with a first layer based on a connected cross type metamaterial and a second layer based on a disconnected cross type metamaterial, which correspond to the case 3, and with the following spacing parameters h_1 = 2 mm and h_2 = 1.6 mm. The return loss S_{11} of the antenna with and without metamaterial superstrate (the four cases cited in table 4-1) are shown in figure 4-4.

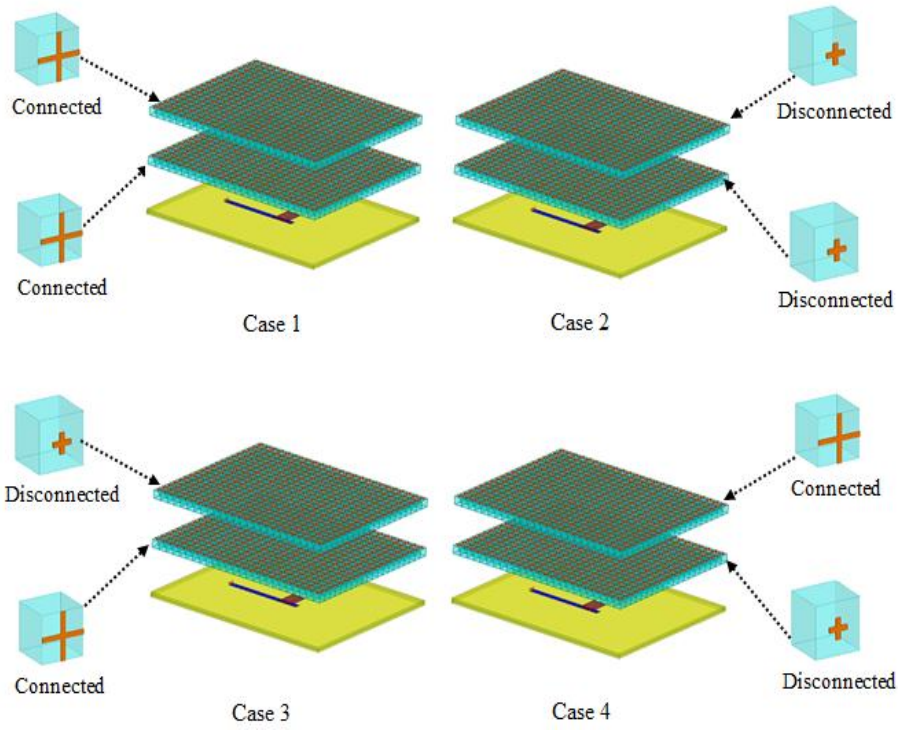

Figure 4-3: Different possible combinations of metamaterials.

Table 4-2: Characteristics of the antenna with DLS lens for the four possible combinations and for different values of h_1 and h_2.

			HPBW in E-plane			HPBW in H-plane				
h_1 (mm)	h_2 (mm)	Realized gain (dB)	θ_i	θ_s	θ_{-3dB}	φ_i	φ_s	φ_{-3dB}	B (%)	cases
1.8	1.2	11.62	-16.34	16.27	32.61	-29.09	31.62	60.71	4.05	Case 1
1.7	0.8	11.73	-15.88	16.47	32.35	-31.23	32.01	63.24	3.16	
2	1.2	11.51	-16.44	15.18	31.62	-24.91	29.48	54.39	3.24	
1.6	1.6	11.2	-19.95	19.26	39.21	-21.02	20.72	41.74	3.44	
2.4	2.4	6.004	-24.03	25.16	49.19	-36.2	34.15	70.35	3.05	Case 2
2.4	2	5.65	-26.2	27.3	53.5	-35.4	35.7	71.1	4.21	
2.4	0.8	5.12	-26.3	25.4	51.7	-36.4	36.8	73.2	3.12	
2.2	2.4	5.02	-24.7	24.9	49.6	-36.12	35.14	71.26	2.25	
1.6.	2	12.53	-16.34	15.27	28.87	-21.11	19.36	40.47	1.39	Case 3
1.8	2	13.25	-15.08	15.27	30.35	-22.77	24.03	46.8	3.37	
2	1.6	13.57	-15.18	13.91	29.09	-19.75	18.19	37.94	4.42	
2	1.2	12.54	-13.62	14.20	27.82	-22.28	21.99	44.27	2.38	
2.4	2.2	10.11	-19.96	19.26	39.22	-33.86	29.39	63.25	4.6	Case 4
2.4	2	9.94	-19.95	19.26	39.21	-30.94	27.24	58.18	2.5	
2.4	2.4	8.96	-21.41	21.60	43.01	-37.56	33.28	70.84	5.60	
2.2	2	8.6	-20.24	20.24	40.48	-31.53	27.93	59.46	1.75	

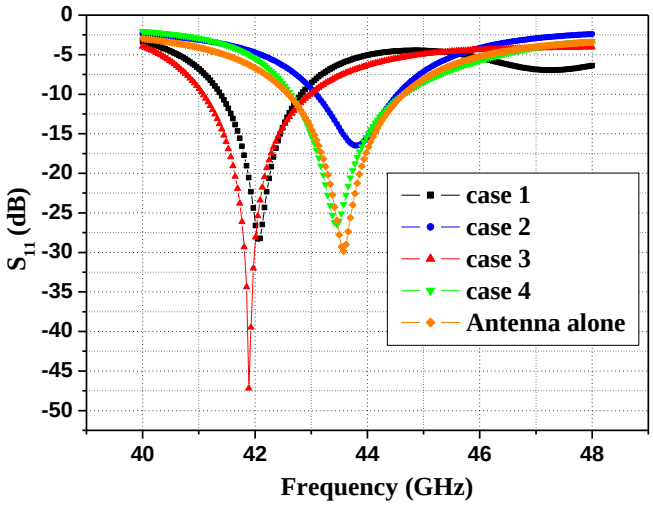

Figure 4-4: Return loss (S_{11}), for the conventional patch antenna and the metamaterial DLS patch antenna.

It is observed from figure 4-4,that the resonance frequency of the antenna is slightly shifted to lower frequencies (about 3 %)when it is loaded with the metamaterial DLS corresponding to the cases 1 and 3 (table 4-1), in other words, when the superstrate first layer is mad of connected cross type metamaterial. Note that for case 2 and 4, when the superstrate first layer is mad of disconnected cross type metamaterial, there is no shift in the antenna resonance frequency. Indeed, in these cases the wave power reflected by the first layer is less than 20 % and the transmitted power is greater than 80 %. Almost all the incident EM waves are transmitted by the metamaterial layer. So, this later do not constitute with the antenna ground plane a Fabri-Peirrot resonant cavity, as does the first layer, mad of connected cross type metamaterial, in cases 1 and 3, where the reflected power is greater than 70 % and the transmitted power is less than 30 %. In these cases the first metamaterial layer constitutes with antenna ground plane a Fabry-Pierrot resonant cavity which influence the overall radiation structure resonance frequency.

The radiation pattern, in the -E and -H plane, of the proposed antenna for the case 1 and case 3 are shown in figure 4-5.It is clear from the plots that the antenna is more directional with a DLS corresponding to case 3. The maximum realized gain obtained is 13.57 dB. The main lobe beam-width in both E and H plane are 29.09 º and 37.94º, respectively.

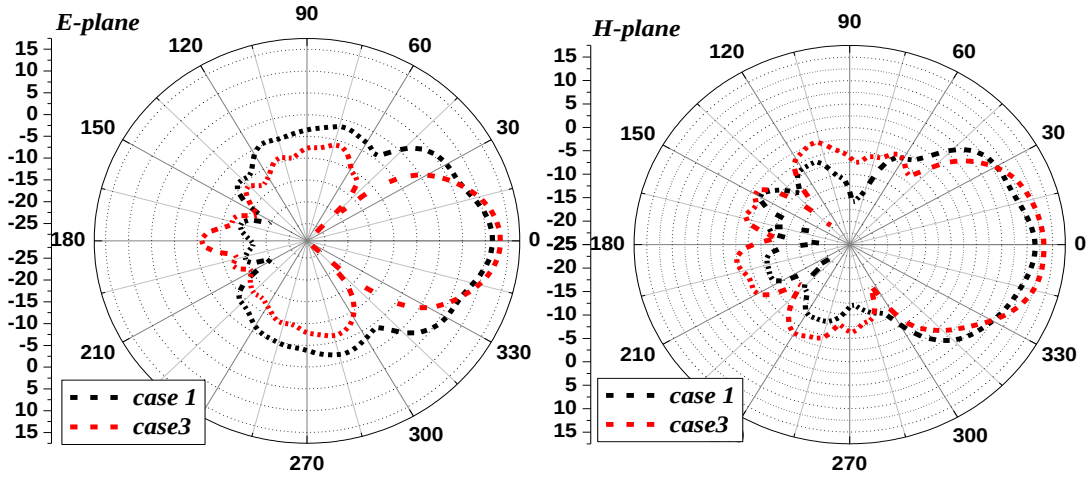

Figure 4-5: Radiation pattern of MPA loaded with MDLS for cases 1 and 3(table 4-1).

4.3.1 Focusing zone influences

To investigate the control of the radiation pattern, we will in the first step, search for the optimal size of the focusing zone when it is placed on the middle position P_0 (see figure 4-7), for each case cited in table 4-1. The optimal dimension of the focusing zone a_Z, is that for which antenna realized gain is maximum. In a second step we explore how the positions of the focusing zone impact the radiation pattern. We have done many simulations to get the optimum focusing zone characteristics. We have tried all possible material (connected cross type and disconnected cross type metamaterial) combinations for the focusing zones and grids body constituting the agile metamaterial lens. The best obtained results correspond to the case 1 (table 4-3) where both focusing zones are based on disconnected cross type metamaterial. The optimization of the focusing zone size a_Z in the center position P_0 for the case 1 is described in table 4-4 and shown in figure 4-6. From table 4-4, it can be seen that the maximum realized gain is 12.90 dB and is obtained for a_z = 0.6 cm.

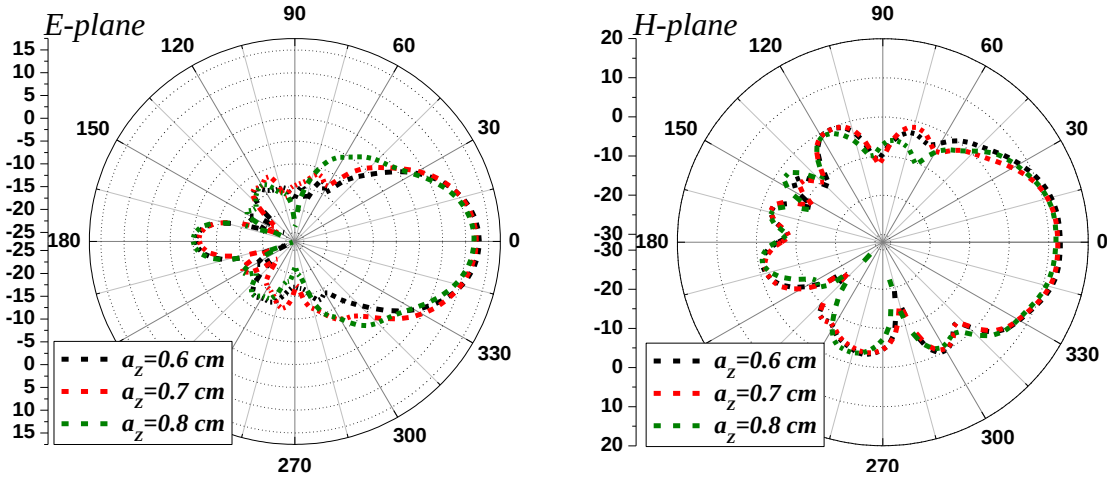

Figure 4-6: Radiation patterns of metamaterial patch antenna for different values of FZ size a_Z.

Table 4-3: The possible combinations of the focusing zone.

Cases	Focusing zone (FZ) type
Case 1	Disconnected Cross
Case 2	Connected Cross
Case 3	FZ 1 :Disconnected Cross
	FZ 2: Connected Cross
Case 4	FZ 1 : Connected Cross
	FZ 2: Disconnected Cross

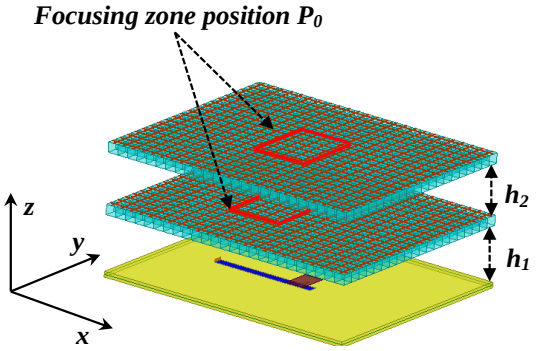

Figure 4-7: Focusing zone in the position P_0.

Table 4-4: Focusing zone size optimization for the case 1 for h_1 = 1.7 mm, h_2 = 0.8 mm.

		HPBW in E-plane			HPBW in H-plane		
a_z (cm)	Realized gain (dB)	θ_i	θ_s	θ_{-3dB}	φ_i	φ_s	φ_{-3dB}
0.2	9.43	-17.49	15.74	33.23	-22.96	23.84	46.8
0.3	8.94	-19.17	17.51	36.68	-24.23	26.38	50.61
0.4	10.10	-18.21	18.53	36.74	-26.76	27.63	54.39
0.5	9.74	-19.36	18.58	37.94	-23.74	23.06	46.8
0.6	12.90	-16.03	16.15	32.18	-23.06	23.74	46.53
0.7	12.38	-19.22	18.78	38	-16.15	15.74	31.9
0.8	11.34	-17.9	17.51	35.41	-18.68	18.06	36.74

The best results in the case 1, are obtained using focusing zones with a_z = 0.6 cm, and grids spacing h_1 = 1.7 mm, and h_2 = 0.8 mm. The radiation pattern half-power beam width, at the operating frequency, in E and H-plane respectively, is observed to be 66.5º and 80.1º for the antenna alone, while it is 32.35º and 63.24º, for the antenna with a double layer superstrate, and 32.18º and 46.53º, for the antenna with a double layer substrate in the presence of focusing zones, are shown in figure 4-8 and table 4-5. The half power beam width reduction is about 21.72 %, with DLS in the H-plan and 48.64 %, in the E-plane, while it is about 60 % in the case of a DLS loaded with FZs in both H-and E-plane.

Table 4-5: Half power beam width θ_{-3dB}(deg) and realized gain of the patch antenna with and without metamaterial DLS

	$\theta_{-3dB}\,(deg)$		Realized gain	B (%)
	E-Plan	H-Plan		
Antenna alone	66.5	80.1	7.2	4.6
Antenna with-DLS	32.18	46.53	12.90	4.2

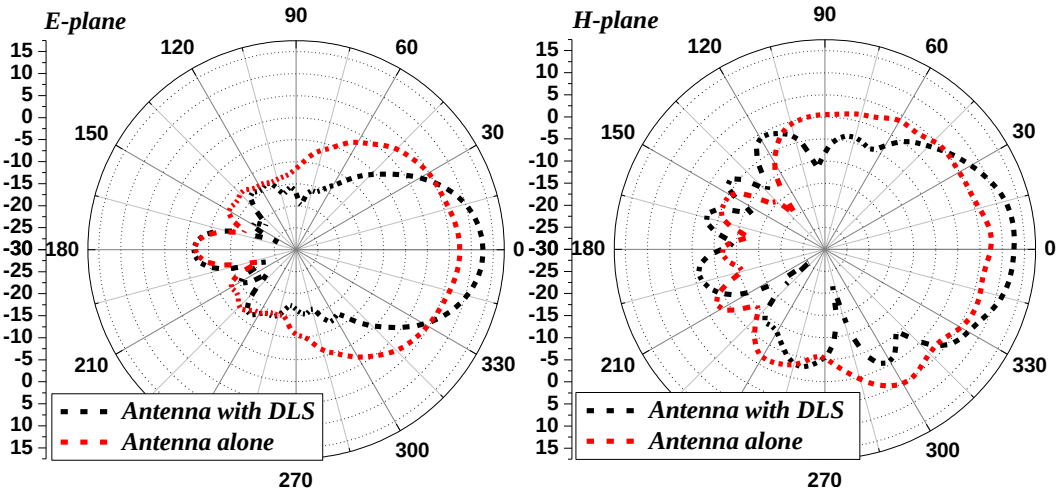

Figure 4-8: Radiation pattern of the patch antenna with and without metamaterial DLS.

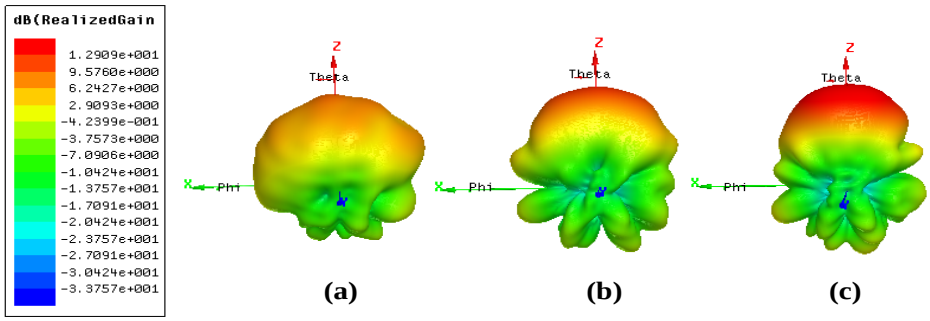

Figure 4-9: 3D Radiation pattern at f = 43 GHz: (a)-patch antenna alone, (b)- antenna with metamaterial DLS, (c)- antenna with metamaterial DLS in the presence of FZs:h_1 = 1.7 mm, h_2 = 0.8 mm, a_Z = 0.6 cm.

We observe from figure 4-9 that, when the metamaterial DLS is placed upon the patch antenna it will collimate the incident electromagnetic waves and therefore improves the gain of the antenna. The peak value of the realized gain is 12.90 dB for the DLS in presence of the FZs.

4.3.2 Radiation pattern control for metamaterial DLS

Once the size of the focusing zone is determined, we will see the effect of the focusing zone positions on the radiation pattern. We chose several positions on the x and y axes as shown in figure 4-10.

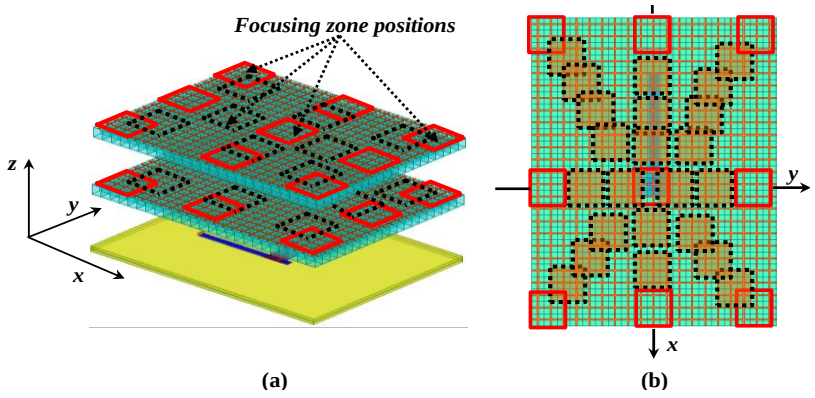

Figure 4-10: Scanning of the focusing zone (a)-Side view (b)-top View.

The simulation results for the different focusing zone positions in the *x* and *y* axes are described in table 4-6.

Table 4-6: Radiation Patter steering by the focusing zone positioning.

	FZ Position		E-plane			H-plane			Realized gain
	x_p (cm)	y_p (cm)	θ_{max}	θ_{-3dB}		φ_{max}	φ_{-3dB}		
				θ_i	θ_s		φ_i	φ_s	
Position P_0	0	0	0	-16.73	16.15	0	-23.06	23.74	12.90
	0	-0.1	-4.72	-21.89	12.26	0	-23.06	22.48	11.95
	0	-0.2	-28.7	-62.86	9.27	0	-23.04	23.74	8.67
Position P_1	0	-0.3	-46.71	-69.48	20.14	0	-23.25	22.28	9.42
	0	-0.4	-25.14	-65.33	11.57	0	-25.23	24.86	8.16
	0	0.1	4.86	12.84	21.31	0	-23.05	23.74	11.94
	0	0.2	28.22	8.46	62.38	0	-23.06	23.74	8.83
Position P_2	0	0.3	46.22	20.92	70.26	0	-23.84	24.23	9.37
	0	0.4	26.24	11.46	65.21	0	-24.32	25.18	8.03
	0.1	0	0	-16.83	16.05	16.64	3.6	36.88	10.09
	0.2	0	0	-16.73	17.41	24.32	9.14	47.10	11.93
Position P_3	0.3	0	0	-19.17	18.78	30.75	13.04	50.99	11.79
	0.4	0	0	-21.79	22.48	25.69	16.83	49.72	9.23
	-0.1	0	0	-16.73	16.15	-16.45	-23.27	-5.74	10.89
	-0.2	0	0	-15.43	16.15	-24.81	-46.32	-5.83	11.74
Position P_4	-0.3	0	0	-18.25	19.16	-30.74	-49.24	-14.34	11.95
	-0.4	0	0	-22.18	21.41	-25.33	-48.12	16.29	9.18
	0.1	-0.1	-2.13	-18.58	15.39	6.20	-17.86	27.57	12.52
	0.2	-0.2	-6.08	-26.29	9.18	19.34	-2.24	33.35	11.48
Position P_5	0.3	-0.3	-38.54	-67.57	-8.25	32.25	13.75	48.12	9.19
	0.4	-0.4	11.63	-9.23	27.21	19.18	1.36	32.08	7.26
	0.1	0.1	2.43	-15.27	17.61	6.13	-17.90	27.59	12.56
	0.2	0.2	6.02	-9.24	22.38	19.36	-2.14	33.28	11.56
Position P_6	0.3	0.3	38.53	8.17	68.16	32.26	13.81	48.03	9.21
	0.4	0.4	11.46	9.34	27.34	19.26	1.42	32.15	7.12
	-0.1	-0.1	-2.23	-18.68	15.47	-6.03	-26.17	20.63	12.73
	-0.2	-0.2	-6.03	-26.27	9.14	-19.36	-43.40	-4.18	11.61
Position P_7	-0.3	-0.3	-38.53	-67.63	-8.17	-32.03	-48.95	-13.52	9.11
	-0.4	-0.4	-11.87	-27.05	9.1	-19.26	-32.60	1.55	7.25
	-0.1	0.1	2.13	-15.18	17.61	-6.23	-26.28	20.54	12.65

	-0.2	0.2	6.25	-9.28	22.38	-19.25	-43.34	-4.27	11.58
Position P_8	-0.3	0.3	38.17	8.19	68.26	-32.11	-48.87	-13.36	9.12
	-0.4	0.4	11.16	9.37	27.31	-19.28	-32.53	1.35	7.17

The focusing zone must cover the patch antenna to observe maximum steering; this is what we observe in table 4-6. The extreme positions which confers the maximum control are: three positions (P_1, P_5 and P_7) in the right of the central position (P_0), three positions (P_2, P_6 and P_8) in the left of P_0, three positions (P_3, P_5 and P_6) in the direction of positive x (forward), and three positions (P_4, P_7 and P_8) in the in the direction of negative x (backward) as shown in figure 4-11.

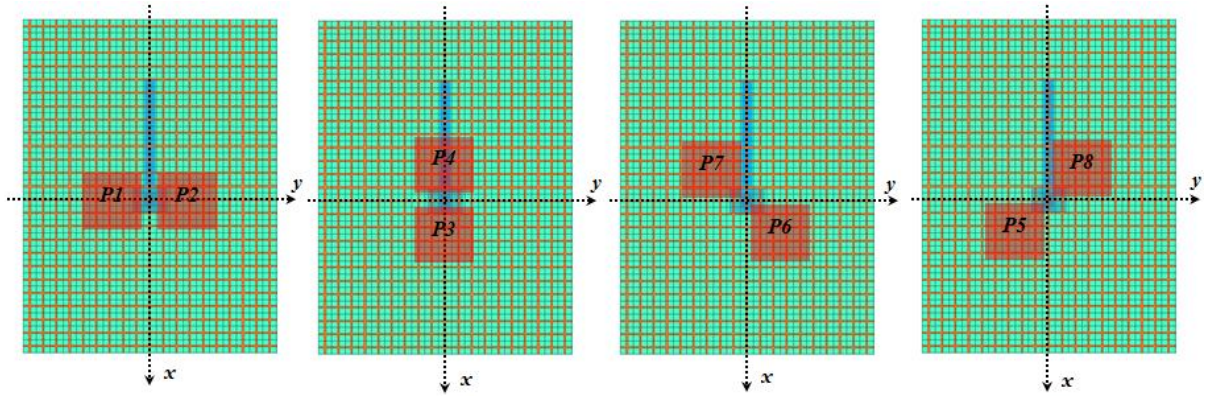

Figure 4-11: Focusing zone positions.

It is observed from table 4-6, that the main beam direction remains at 0° in the position P_0, and is rotated from 46° and -46°,in the E-plane, if focusing zones move from position P_1 to P_2, as illustrated also in figure 4-12.

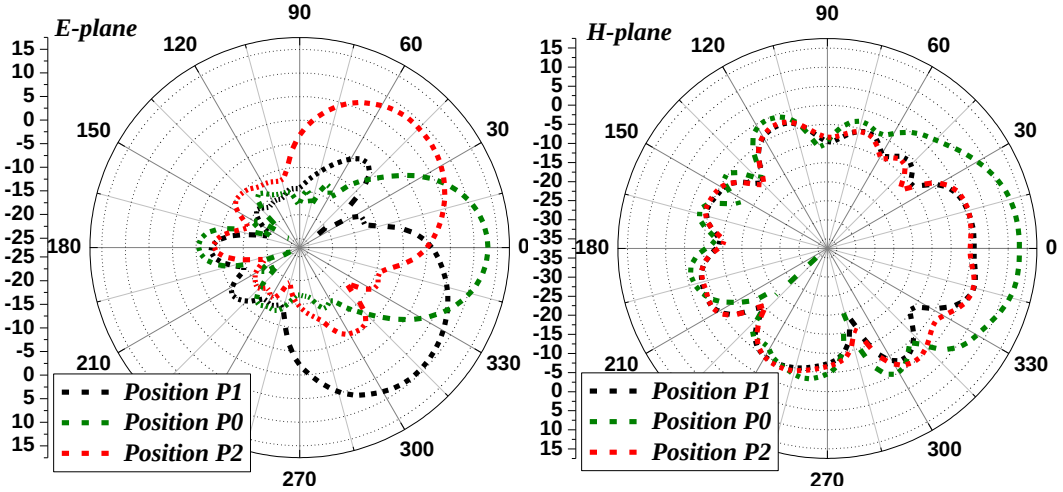

Figure 4-12: Radiation pattern steering in E and H plane: FZ in positionsP_1, P_0, and P_2.

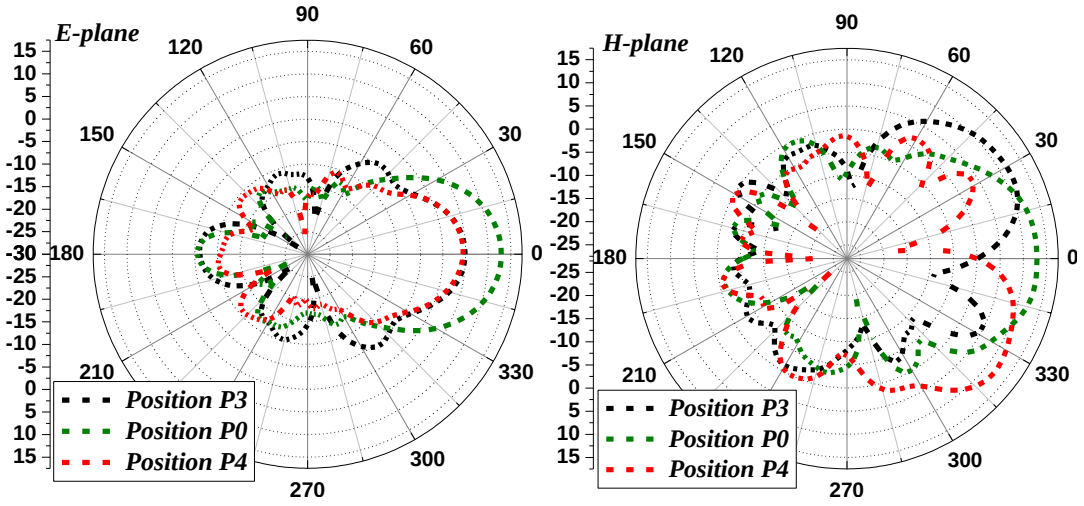

Figure 4-13: Radiation pattern steering in E and H plane: FZ in positionsP_3, P_0, and P_4.

Similarly, the beam direction is rotated from 30^0 and -30^0, in H-plane, if focusing zones are moved from positions P_3 to P_4 (figure 4-13). It is can be seen from figure 4-13 and 4-12, that the realized gain in E plane, for the positions P_3 and P_4, and in H plane, for the positions P_1 and P_2, is lower than in position P_0. This is due to the fact that focusing zones cover a small portion of the patch antenna, in these positions (P_1, P_2, P_3, and P_4) compared to the position P_0.

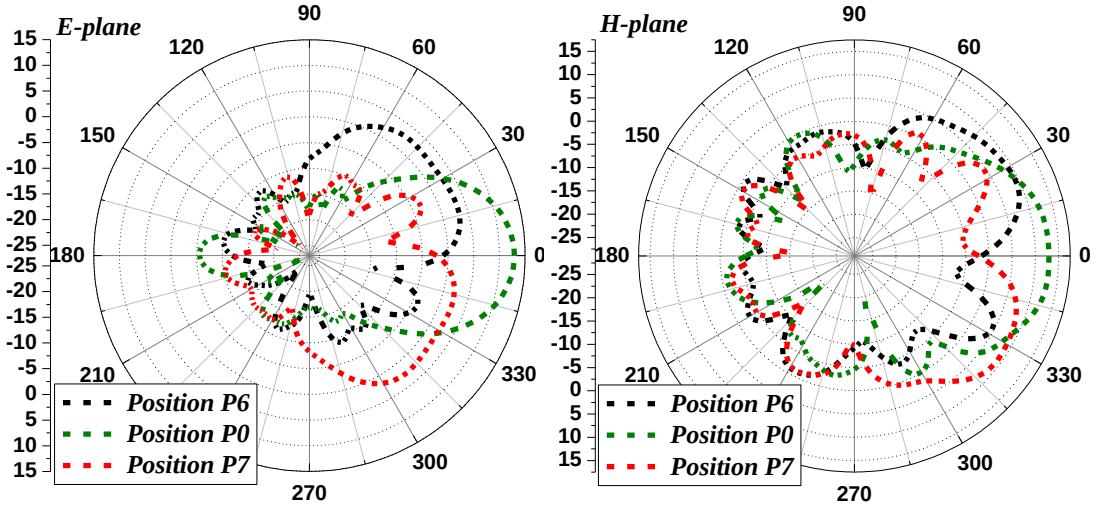

Figure 4-14: Radiation pattern steering in E and H plane: FZ in positionsP_6, P_0, and P_7.

However, the focusing zone act on the radiation pattern E-plane when it moved from P_1, to P_2 passing by P_0 and H-plane when it moved from P_3, to P_4 passing by P_0. While it acts on both E- and H-planes when it moved from position P_6 to P_7, and from P_5 to P_8. The main beam is rotated by 38^0 and -38^0 in E-plane and 32^0, -32^0 in H plane for the positions P_5 and P_8, respectively, and rotated by 38^0 and -38^0 in E-plane and 32^0, -32^0 in H plane for the positions P_6 and P_7, respectively.

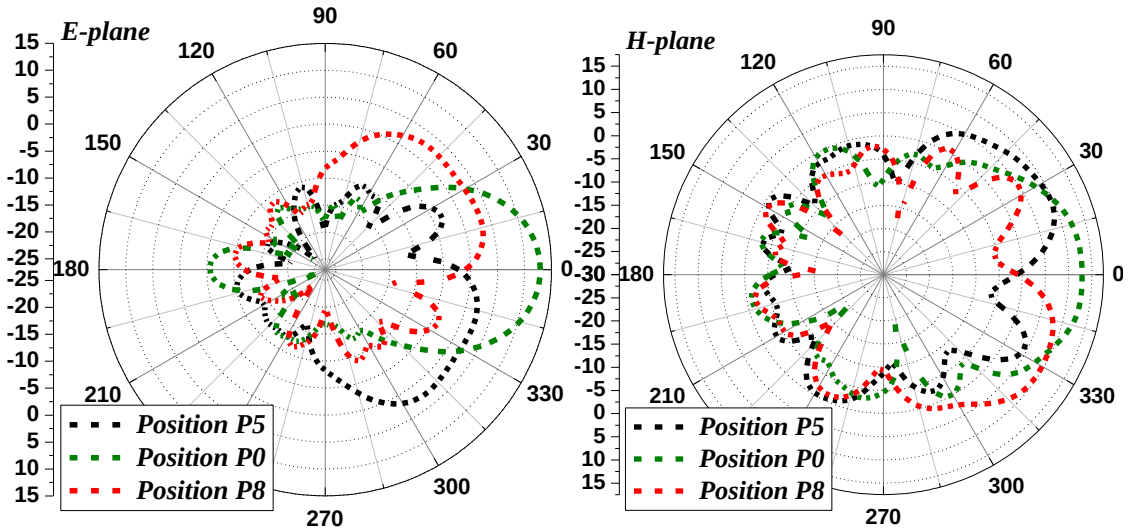

Figure 4-15: Radiation pattern steering in E and H plane: FZ in positionsP_5, P_0, and P_8.

We can also note that the FZ in P_5 rotates the main beam pattern by -38.54° in E-plane and by 32.25° in H-plane, while it rotates by 38.17° in E-plane and -32.11° in H-plane if it is positioned in P_8.Notethat the radiation pattern main-lobe, in the H-plane, is rotated toward the positive direction and have the same amplitude when FZ is in positions P_5 and P_6. On the contrary, always for H-plane, the main lobe is rotated toward the negative direction if the FZ is positioned in P_7 and P_8, as shown in figure 4-16. Similarly, from the same figure we observe that the radiation pattern main-lobe, in the E-plane, are rotated toward the positive direction and have the same amplitude, when FZ is in positions P_6 and $P_{8,}$ and it is rotated toward the negative direction if the FZ is positioned in P_5 and P_7, as shown in figure 4-16.

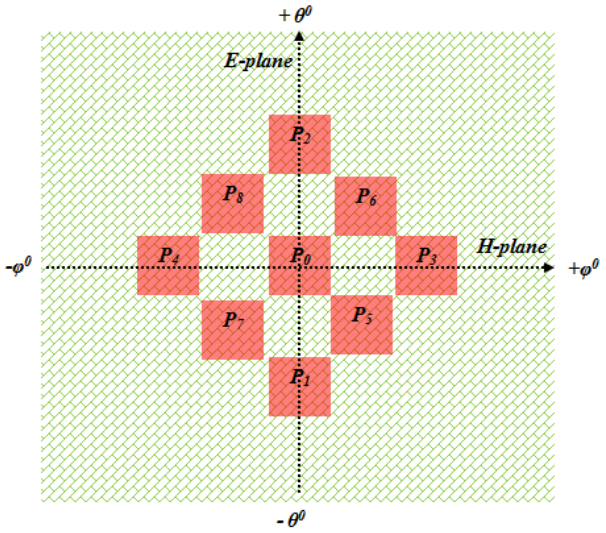

Figure 4-16: Focusing zone positions in E and H-planes.

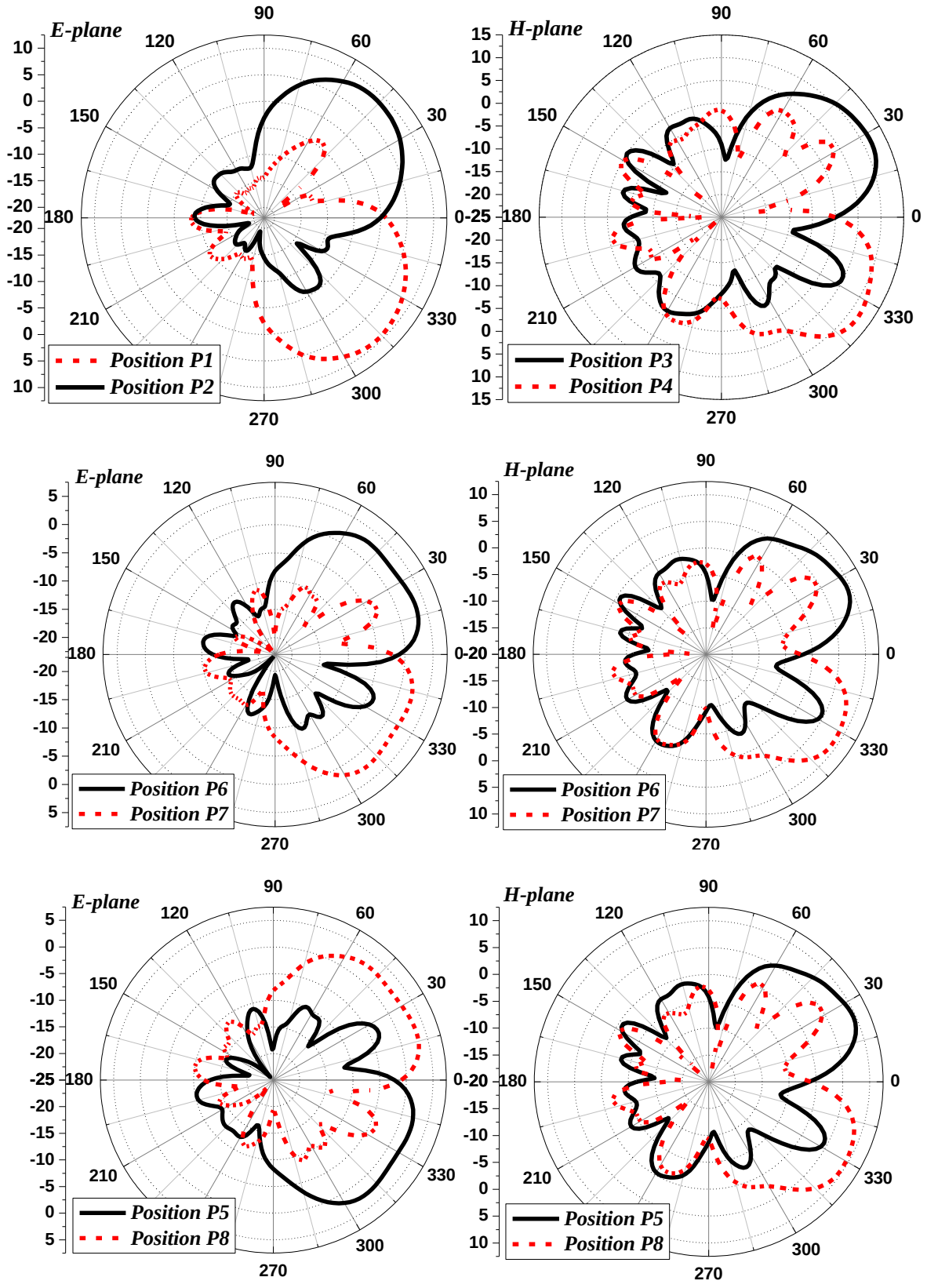

Figure 4-17: Radiation pattern steering for different positions of FZ.

Figure 4-17, gives a summary and illustrates the previous results of the radiation pattern beam steering for different positions in E and H planes. Finally we conclude that positions

between P_1 and P_2 act only on the E-plane, while positions between P_3 and P_4 act only on the H-plane. The positions between P_5 and P_8 and between P_6 and P_7 act in both E and H-planes of the radiation pattern.

As we mentioned earlier, the DLS metamaterial lens has a dark point and it is not mechanically stable and is more prone to fractures. So to satisfy this stability requirement, we think about a more compact and mechanically stable metamaterial lens, compared to the DLS one, based on a single-layer superstrate (SLS). This feature will be discussed in the next section.

4.4 Metamaterial lens with Single Layer Superstrate (SLS)

4.4.1 Single Layer Superstrate lens based on connected cross type metamaterial

In this section, the connected cross type agile metamaterial is used to form a planar single-layer metamaterial lens, as shown in figure 4-18. As already states, this lens is utilized for gain enhancement and the radiation pattern control of a patch antenna. The proposed metamaterial lens consists of 20 x 25 cross unit cells, and is positioned above the patch antenna. The simulation was done on varying the distance between the single layer and the antenna h_1 to observe the gain enhancement.

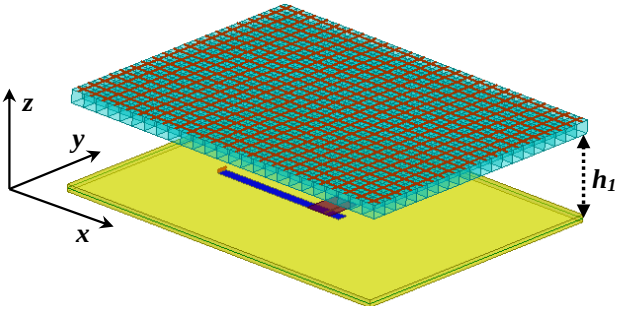

Figure 4-18: Antenna with metamaterial single layer superstrate.

Table 4-7: Characteristics of the patch antenna with SLS based on connected cross metamaterial.

		HPBW in E-plane			HPBW in H-plane			
h_1 (mm)	Realized gain (dB)	θ_i	θ_s	θ_{-3dB}	φ_i	φ_s	φ_{3dB}	Bandwidth (%)
1.1	9.57	-22.28	22.02	43.3	-24.13	25.20	49.15	3.45
1.15	10.12	-22.09	22.18	44.27	-23.74	24.32	47.49	2.57
1.2	9.05	-22.86	22.67	45.53	-22.86	23.94	50.36	2.48
1.4	8.83	-20.29	20.72	41.01	-25.28	26.73	52.01	2.5
1.5	8.34	-19.69	19.89	39.58	-26.28	28.88	55.16	2.65

The simulation results of the spacing parameter optimization h_1, for antenna with the connected cross type metamaterial SLS is presented in table 4-7. From table 4-7, we observe

that the spacing between the patch antenna and the superstrate layer is a key parameter in the antenna gain improvement. It can be optimized to obtain better antenna realized gain enhancement. A parametric study shows that the optimal value for the spacing is h_1 = 1.15 mm as also shown in figure 4-19.

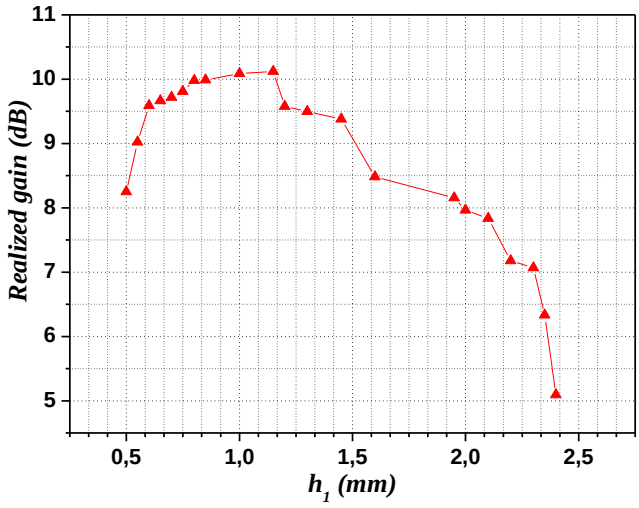

Figure 4-19: Realized gain of the patch antenna with SLS based on connected cross metamaterial for different spacing h_1.

The half-power beam width of the antennas at the operating frequency, in E and H-planes are 44.27º and 47.49º, respectively, for the antenna with SLS lens (with h_1 = 1.15 mm), as shown in figure 4-20 and 4-21.

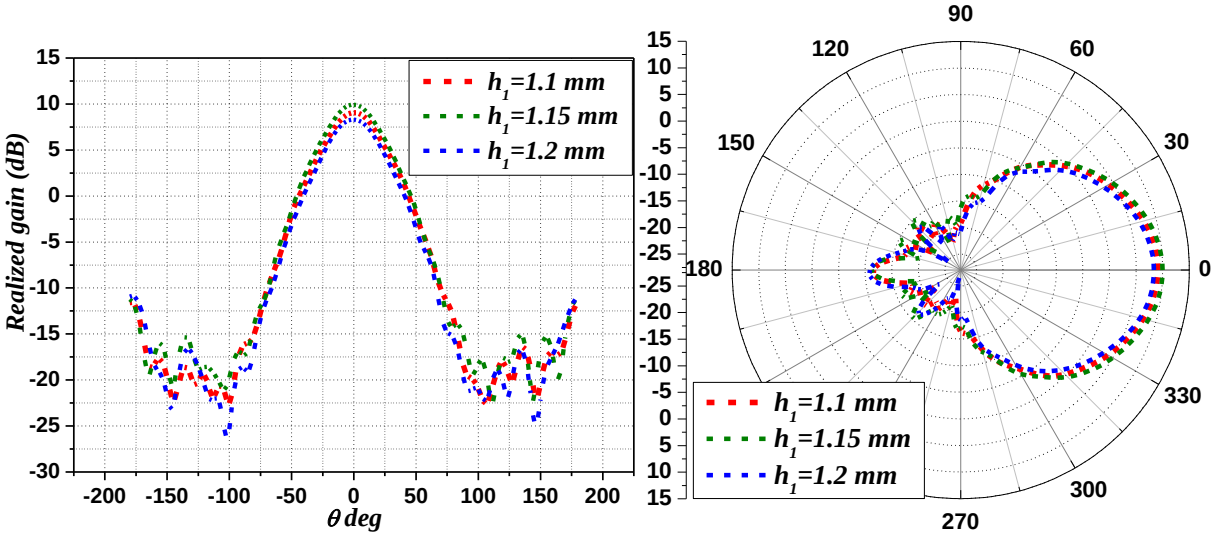

Figure 4-20: Radiation pattern of the antenna with SLS based on connected cross metamaterial for different values of h_1 in E plane.

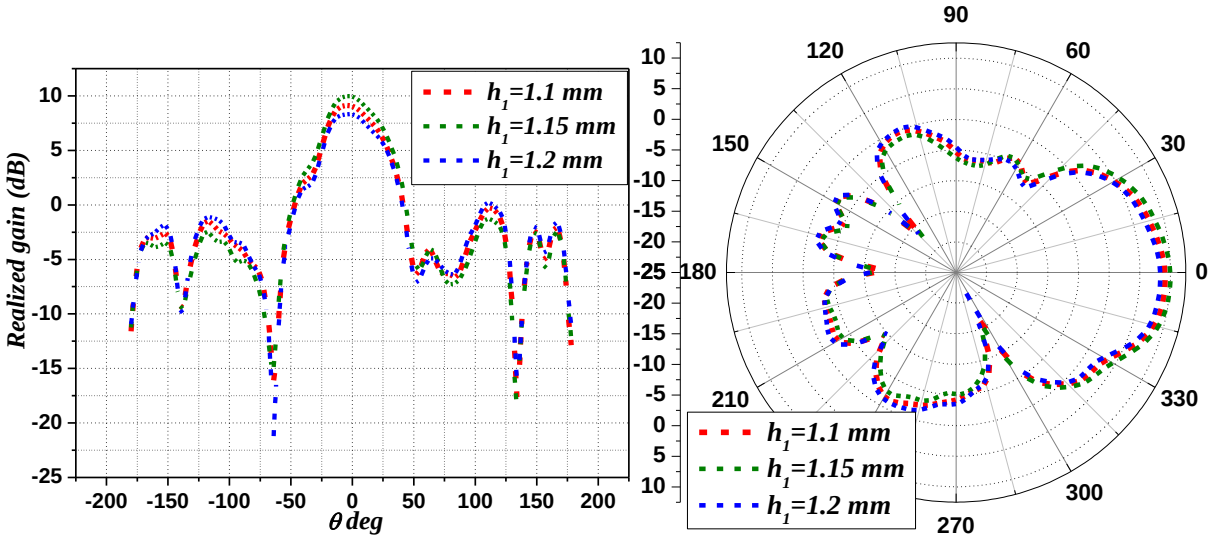

Figure 4-21: Radiation pattern of the antenna with SLS based on connected cross metamaterial for different values ofh_1 in H-plane.

The presence of the SLS lens, based on connected cross type metamaterial, increases the antenna gain from 7.55 dB to 10.12 dB for h_1 = 1.15 mm witch corresponds to an enhancement of 2.57 dB.

Figure 4-23 shows the simulated return loss as a function of frequency for different values of the spacing parameter h_1. The S_{11} holds the importance parameter in any antenna design as it depicts how well the signal could be transmitted from the antenna. The simulated antenna presents a bandwidth of 2.57 % (40.25 - 41.3 GHz) it decreases compared to the 4.42 %, for antenna with a DLS lens (case 3 h_1 = 2 mm h_2 = 1.6 mm see table 4-8 and figure 4-22).

Table 4-8: Half power beam width θ_{-3dB}(deg) and realized gain of the patch antenna with and without metamaterial DLS and SLS.

	$\theta_{-3dB}\,(deg)$		Realized gain	B (%)
	E-Plan	H-Plan		
Antenna alone	66.5	80.1	7.2	4.6
Antenna with-DLS case 3	29.09	37.94	13.57	4.42
Antenna with-SLS	44.27	47.49	10.12	2.57

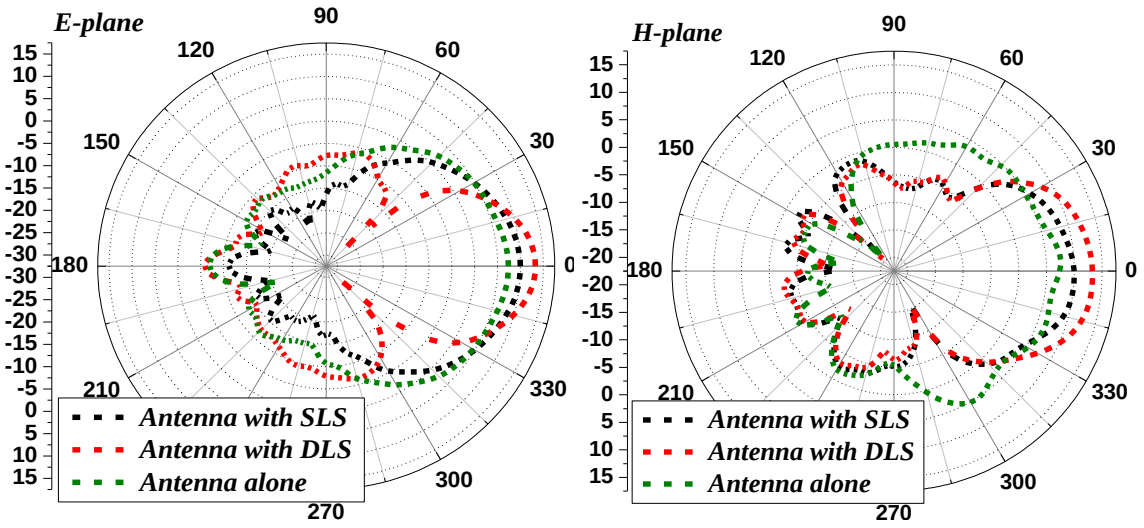

Figure 4-22 : Radiation pattern of the patch antenna with and without metamaterial SLS and DLS

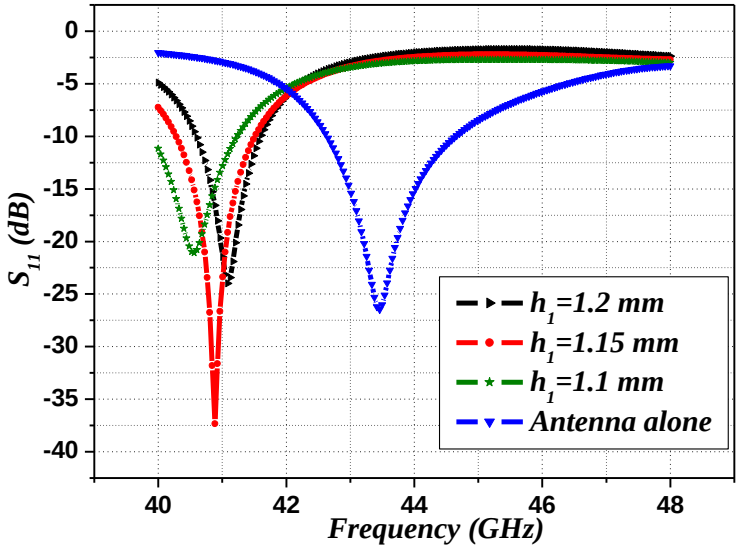

Figure 4-23: Return loss (S_{11}) of the conventional patch antenna and the metamaterial SLS patch antenna for different values of h_1.

4.4.2 Single Layer Superstrate lens based on disconnected cross type metamaterial

In this section we investigate how a single layer superstrate metamaterial lens, based on disconnected cross type metamaterial, affects the antenna gain. Table 4-7 and Table 4-9 show that the SLS lens based on disconnected cross type metamaterial does not provide any enhancement in the antenna gain. This is due to the fact that the disconnected cross type metamaterial behaves like an effective medium having a refractive index slightly above the unity. This disconnected cross type metamaterial does not focuses the waves as the zero index metamaterial (connected cross type) does. The realized gain obtained by this disconnected cross type metamaterial SLS lens is comparable to that of the antenna alone (table 4-9).

Table 4-9: Characteristics of the patch antenna with SLS based on disconnected cross type metamaterial.

		HPBW in E-plane			HPBW in H-plane		
h_1 (mm)	Realized gain (dB)	θ_i	θ_s	$\theta_{\text{-3dB}}$	φ_i	φ_s	$\varphi_{\text{-3dB}}$
2	5.24	-29.77	29.68	59.45	-32.47	32.22	64.69
2.3	5.56	-30.46	29.08	59.54	-32.40	32.11	64.5
2.5	6.01	-28.31	28.61	56.92	-32.51	32.6	65.11
2.7	7.46	-27.14	27.26	54.4	32.26	32.21	64.47

4.4.3 Focusing zone effect

In this section we investigate the effect of the agile lens with SLS based on connected cross type metamaterial in the presence of the focusing zone based on disconnected cross type metamaterial. Table 4-10 shows the radio electric characteristics of the antenna with agile SLS metamaterial lens (the realized gain, the half power beam-width, and the bandwidth) for different focusing zone sizes when placed in the position P_0. The radiation patterns of a microstrip patch antenna with SLS are shown in figure 4-24 and 4-25. It is clear from these plots that loading a microstrip antenna with the single layer superstrate and focusing zone metamaterial, focuses the waves radiated by the antenna and thereby enhances the antenna gain. The half-power beam width of the antennas, at the operating frequency, in E and H-planes respectively, is observed to be 49.76º and 56.1º for FZ with $a_Z = 0.5$ cm. The half power beam width is reduced by about 25.17 % in the E-plane and 29.97 % in the H-plane. Figure 4-26 shows the 3D representation of the radiation patterns of the three studied antennas: the patch antenna alone, the patch antenna with SLS, and the patch antenna with SLS in the presence of FZ.

Table 4-10: Characteristics of the patch antenna with SLS based on connected cross metamaterial and FZ: Focusing zone size effect.

			HPBW in E-plane			HPBW in H-plane			
h_1(mm)	a_z (cm)	Realized gain (dB)	θ_i	θ_s	$\theta_{\text{-3dB}}$	φ_i	φ_s	$\varphi_{\text{-3dB}}$	Bandwidth (%)
1.15	0.2	8.95	-21.89	21.29	43.18	-25.08	26.48	51.56	2.93
1.15	0.3	8.20	-22.88	22.68	45.56	-23.88	26.48	50.36	2.29
1.15	0.4	9.05	-24.68	24.48	49.16	-22.68	24.08	46.76	2.7
1.15	0.5	10.27	-24.68	25.08	49.76	-27.8	28.3	56.1	1.63
1.15	0.6	9.86	-26.48	23.88	50.36	-21.69	22.68	44.37	2.8
1.15	0.7	9.29	-29.08	29.68	58.76	-20.29	21.69	41.98	2.5

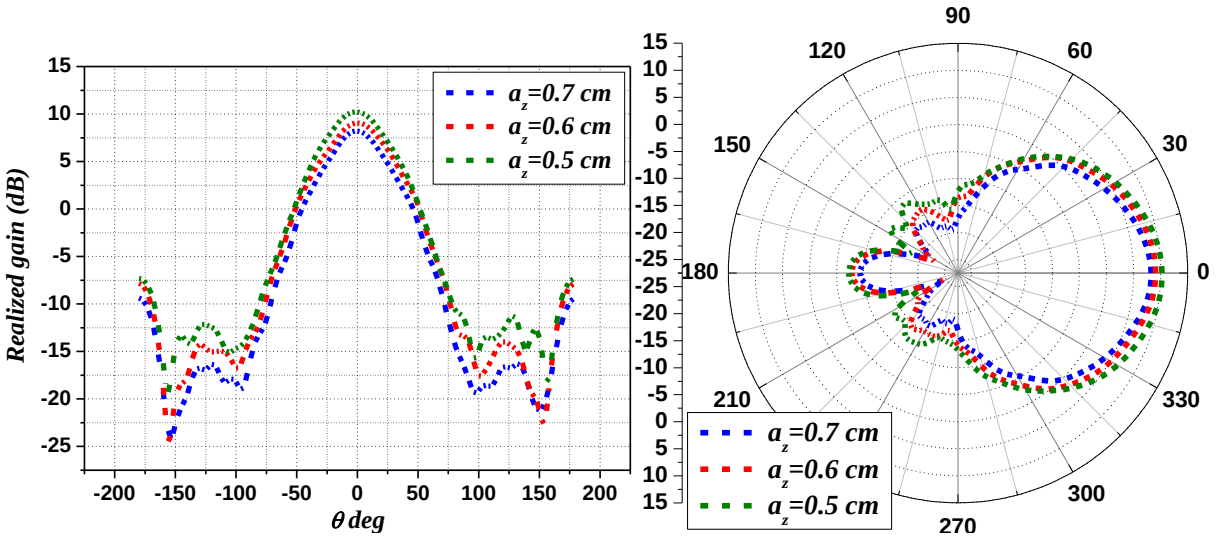

Figure 4-24: Radiation pattern of the antenna with SLS based on connected cross metamaterial with FZ for different values of focusing zone size in E plane.

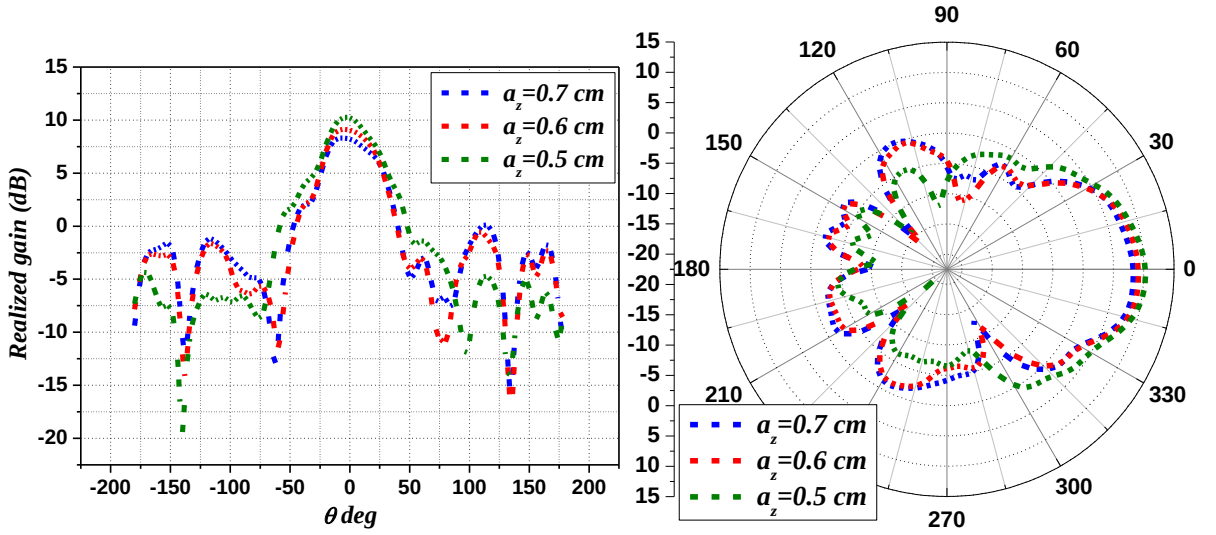

Figure 4-25: Radiation pattern of the antenna with SLS based on connected cross metamaterial with FZ for different values of focusing zone size in H-plane.

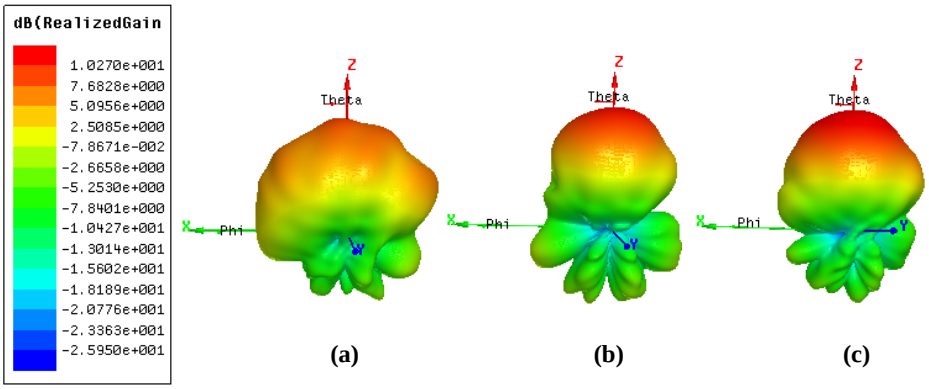

Figure 4-26:The 3D radiation pattern of:(a) patch antenna alone, (b) antenna with metamaterial SLS,(c) antenna with metamaterial SLS in the presence of FZ for a_Z = 0.5 cm.

The maximum realized gain of the patch antenna with SLS and a focusing zone is found to be 10.27 dB when we use a focusing zone based on disconnected cross type metamaterial with a_Z = 0.5 cm. This design enhances the antenna gain by 2.72 dB, which corresponds to about 36.5 %, compared to the MPA antenna alone.

4.4.4 Wave propagation through a zero refraction index material

Our lens used as a superstrate above the patch antenna is based on connected cross type metamaterial. This metamaterial behaves as a zero refraction index medium (ZIM) under the homogenization criterion. This metamaterial lens collimates the waves in the direction normal to the interface. The physics behind this collimation effect is the zero refraction index. In such medium, with zero refraction index, when a wave travels throw a distance *d*, the wave propagation phase is given by $\Delta\varphi = nk_0 d \approx 0$. So according to Snells law, at the ZIM medium and free space interface, the wave will experience an angle of refraction close to zero and thus the refracted wave will be focused in the direction perpendicular to the medium interface as shown in figure 4-27. In ZIM, the propagation phase is independent of the propagation distance*d*. It is expected that the propagation phase will be the same at the interface between the medium and the free space for a plane or a spherical wave. Hence, the form of the electromagnetic wave front depends on the curvature of the emergent surface when the electromagnetic wave travels through the ZIM.

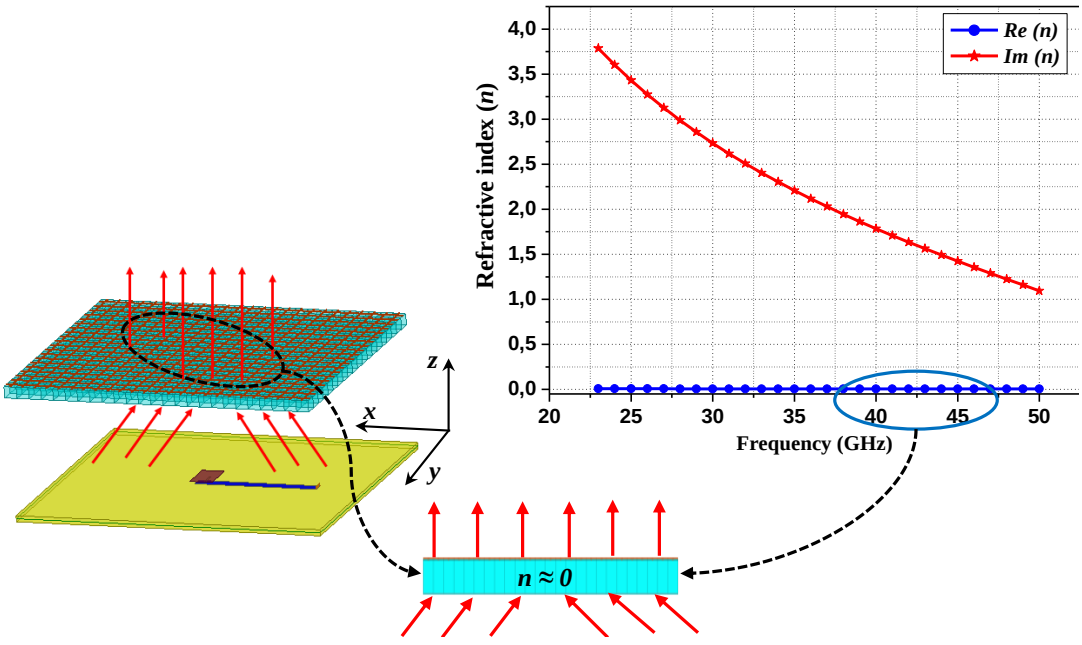

Figure 4-27: Wave propagation inside a zero-index metamaterial.

We conclude that the energy radiated by the connected cross type metamaterial surface covering the antenna becomes more concentrated. As a result, the antenna becomes more directive and presents higher gain.

4.4.5 Effect of the metamaterial lens number of layers

In this section we examine the effect of the number of layers constituting the metamaterial superstrate.

Figure 4-28 shows a 3D radiation pattern for the conventional patch antenna and the metamaterial antennas with different layer numbers of the cover. We can see that the main lobe of the radiation pattern becomes more directive as the number of layers of the cover increases. The metamaterial superstrate collimation effect is intensified with the numbers layers. The maximum realized gain of patch antenna is found to be 10.27 dB with a single a single layer superstrate, while it is 12.90 dB with double layer superstrate.

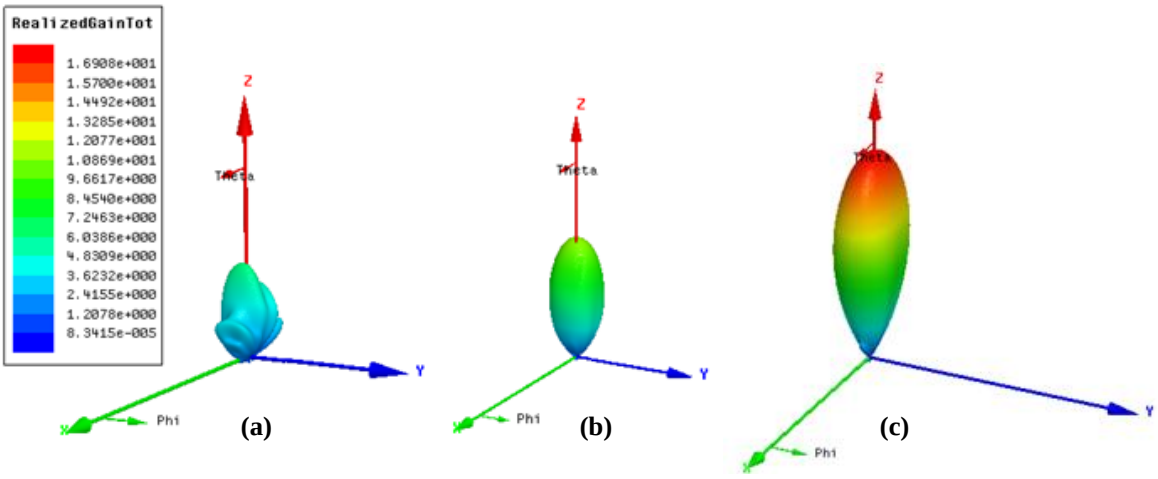

Figure 4-28: Radiation pattern in spherical coordinates (a) Conventional patch antenna (b) single layer patch antenna (c) double layers patch antenna.

4.4.6 Radiation pattern control using the metamaterial SLS lens

In this section we will use the same procedure used with the metamaterial DLS lens to examine the control of the antenna radiation pattern by the FZ positioning. The position of the FZ is determined by the coordinates of its center (x_p, y_p) in the (x, y) plane. The results are summarized in table 4-11, where is reported the main lobe pointing direction, the half-power beam-width and the antenna gain.

Table 4-11: Radiation pattern steering by focusing zone positioning.

	FZ Position		E-plane			H-plane			Realized gain (dB)
	x_p (cm)	y_p (cm)	θ_{max}	θ_{-3dB}		φ_{max}	φ_{-3dB}		
				θ_i	θ_S		φ_i	φ_s	
Position P_0	0	0	0	-24.68	25.08	0	-27.8	28.3	10.27
	0	-0.2	-21.79	-44.79	-5.81	-0.97	-17.23	15.65	9.91
Position P_1	0	-0.3	-28.12	-49.63	-6.61	-0.85	-19.95	19.26	9.87
	0	-0.4	-25.30	-44.27	-10.12	-0.92	-21.21	23.06	9.74
	0	0.2	21.99	5.83	44.76	-0.97	-17.12	15.73	9.93
Position P_2	0	0.3	28.08	6.22	49.24	-0.97	-19.95	20.53	9.8
	0	0.4	25.49	10.31	44.47	-0.86	-21.11	23.16	9.73
	0.2	0	-0.97	-30.26	29.19	10.12	-8.46	26.56	9.60
Position P_3	0.3	0	-0.97	-26.27	25.59	27.54	7.29	43.98	11.25
	0.4	0	0.38	-21.11	20.63	21.38	7.3	37.46	8.89
	-0.2	0	-0.87	-29.97	29.48	-10.18	26.85	8.56	9.2
Position P_4	-0.3	0	0.38	-24.71	23.35	-27.63	-45.41	-6.86	11.30
	-0.4	0	0.38	-22.38	21.89	-21.89	-37.35	-7.42	8.76
	0.2	-0.2	-8.58	-30.26	21.62	5.15	-13.72	17.36	7.13
Position P_5	0.3	-0.3	-25.26	-50.57	2.63	15.16	-4.18	32.78	9.31
	0.4	-0.4	-6.85	-21.46	17.73	7.15	-12.13	19.26	7.14
	0.2	0.2	8.04	-21.99	29.87	5.04	-15.66	17.22	7.04
Position P_6	0.3	0.3	25.01	-2.82	50.31	15.02	-3.99	32.69	9.26
	0.4	0.4	7.68	-12.18	19.54	6.14	-15.42	21.54	7.02
	-0.2	-0.2	-8.43	-30.26	22.86	-5.43	20.17	15.27	7.08
Position P_7	-0.3	-0.3	-25.07	-50.41	2.72	-15.08	-31.33	2.82	9.27
	-0.4	-0.4	-6.55	-20.41	17.80	-7.24	-19.35	12.14	8.15
	-0.2	0.2	8.12	-22.3	30.07	-5.56	20.22	15.31	7.11
Position P_8	-0.3	0.3	25.16	-2.91	50.46	-15.17	-31.46	2.76	9.32
	-0.4	0.4	7.53	-12.25	19.63	-7.23	-19.38	12.28	8.24

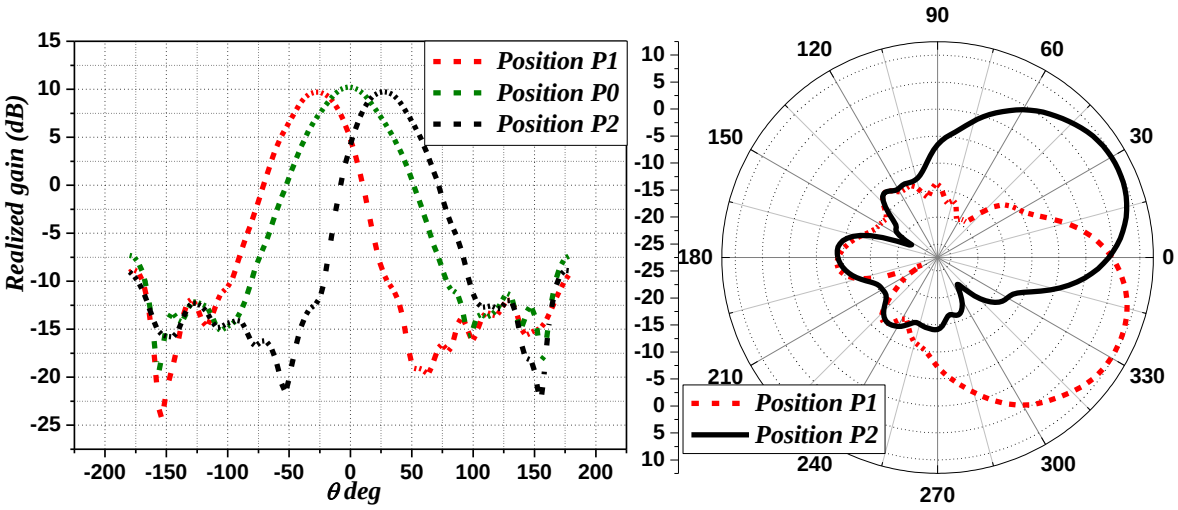

Figure 4-29: Radiation pattern steering in E-plane: FZ in position P_1 and P_2.

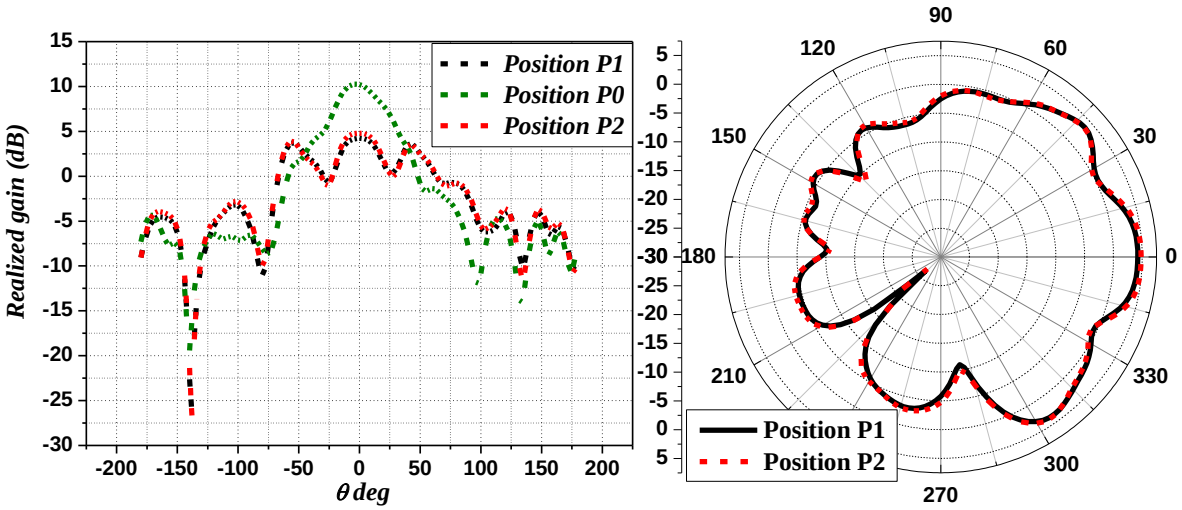

Figure 4-30: Radiation pattern steering in H-plane: FZ in position P_1 and P_2.

The FZ should cover part of the antenna to observe the control; this is what explains our table. This result supports our conclusion that we have acquired with metamaterial DLS.

Figure 4-29 and 4-30 illustrate very clearly the antenna radiation pattern control, when the focusing zone placed in P_1 and P_2.The main lobe is rotated on both sides of the direction $\theta = 0°$. The amplitude of the rotation angle is about 28° in E-plane. However, there is no effect of the focusing zone in the H-plane.

Similarly, the focusing zone acts only on the H-plane of the radiation pattern when it is placed between positions P_3 and P_4 as shown in figure 4-31 and 4-32. The FZ positioned in P_3 rotates the main beam pattern by 27.54° and by -27.63° if it is positioned in P_4. This corresponds to a rotation angle amplitude of about 28° similar to that found in E-plan.

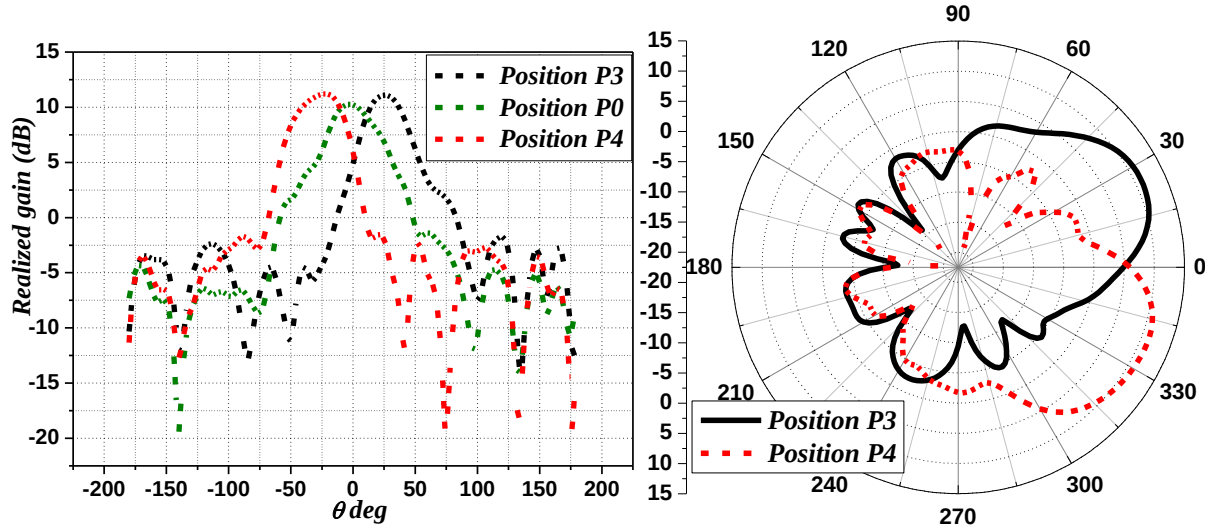

Figure 4-31: Radiation pattern steering in H-plane: FZ in position P3 and P4.

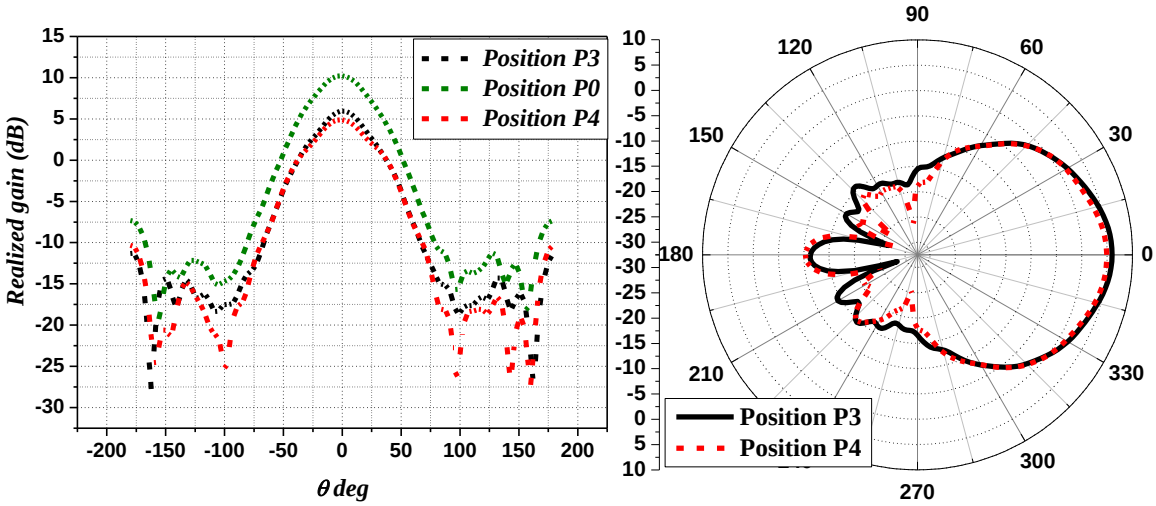

Figure 4-32: Radiation pattern steering in E-plane: FZ in position P3 and P4.

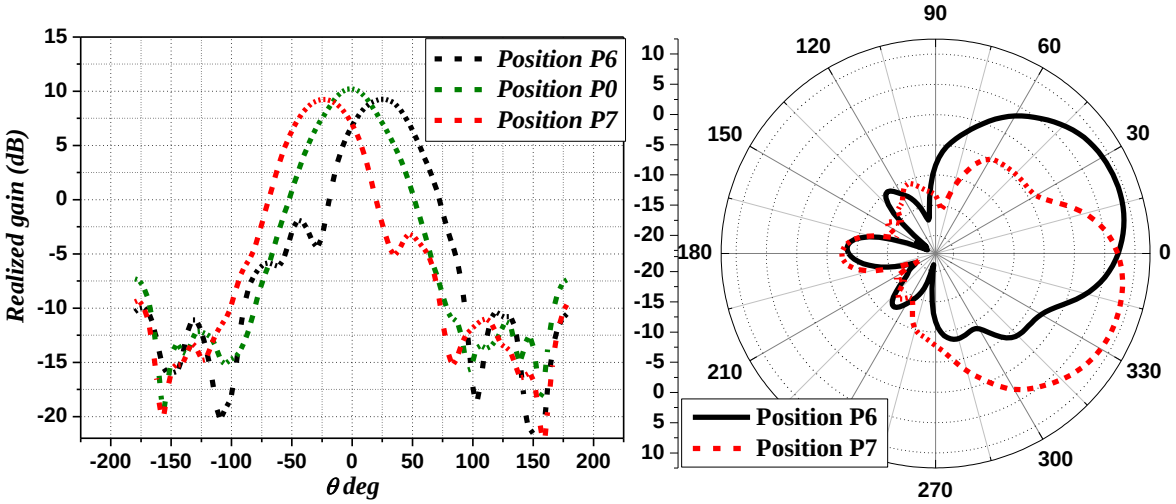

Figure 4-33: Radiation pattern steering: FZ in position P_6 and P_7, E-plane.

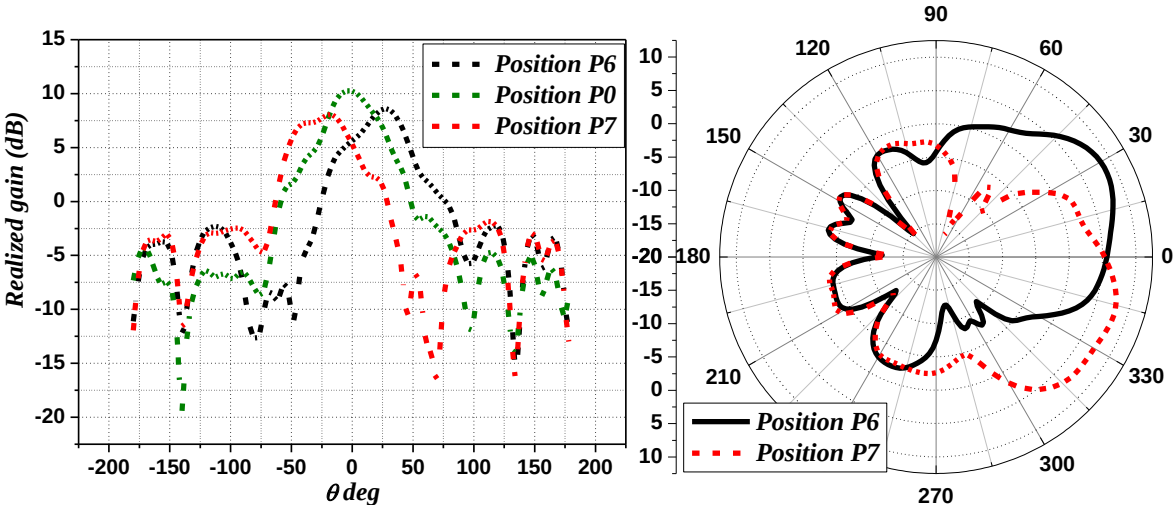

Figure 4-34: Radiation pattern steering: FZ in position P_6 and P_7, H-plane.

When the FZ is moved from P_6 to P_7 or between P_5 and P_8 it acts on both E and H planes of the radiation pattern. Figure 4-33 and 4-34 show that between P_6 and P_7 the radiation patter is rotated from 25° to -25° clockwise in the E-plane and from 15° to -15°counterclockwise in the H-plane. Similarly, Between P_5 and P_8 the radiation patter is rotated from -25° to 25° counterclockwise in the E-plane and from 15° to -15° clockwise in the H-plane, as it can be seen in figure 4-35and 4-36.

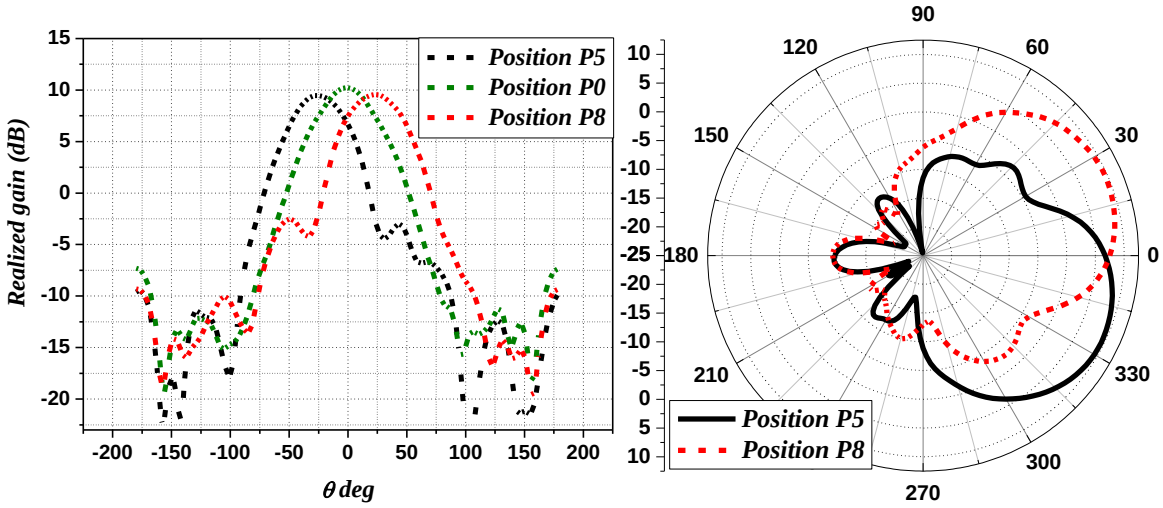

Figure 4-35: Radiation pattern steering: FZ in position P_5 and $P_8$for E-plane.

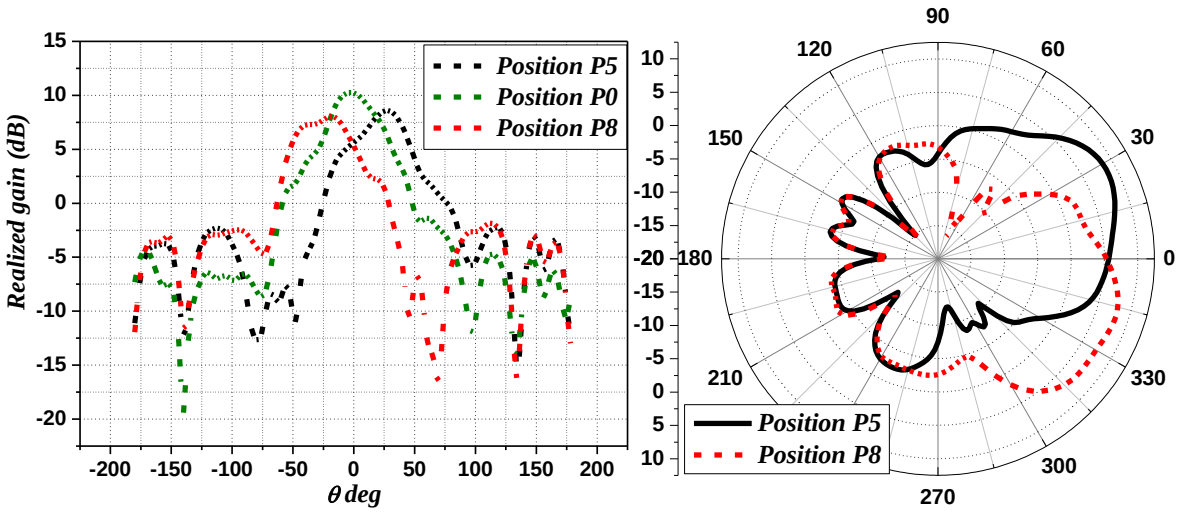

Figure 4-36: Radiation pattern steering: FZ in position P_5 and P_8forH-plane.

4.5 The spherical cap shape metamaterial lens

The weakness of the metamaterial DLS and SLS lenses they are aerodynamically and mechanically not very stable. For this reason, we design a new metamaterial lens based on a spherical cap cover it depicted in figure 4-37. This new lens is more aerodynamically and mechanically stable, compared to the SLS and DLS.

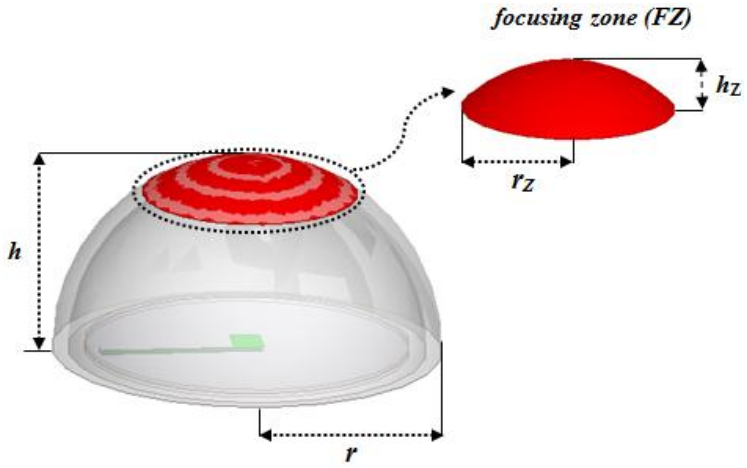

Figure 4-37: Spherical cap lens

There are two key factors to adjust in the cap lens characterization: the radius of the cap, and the grid's spacing in the *z*-axis direction (the height of the cap *h*), they can be optimized to obtain high-gain patch antenna.

In the following sections we will examine the two cases where the spherical lens is made of disconnected and connected cross type metamaterials.

4.5.1 Spherical cap shape lens based on connected cross type metamaterial

The simulation results of the optimizations of the spacing parameter *h* and the radius *r*, for the spherical cap shape lens based on connected cross type metamaterial is described in table 4-12.The realized gain of the antenna with spherical cap based on connected cross type metamaterial for different values of *r* and *h* are shown in figure 4-38.

Table 4-12: Characteristics of the patch antenna with the spherical cap shape lens based on connected cross type metamaterial for different values of *r* and *h*.

			HPBW in E-plane			HPBW in H-plane		
h (cm)	*r* (cm)	Realized gain (dB)	θ_i	θ_s	θ_{-3dB}	φ_i	φ_s	φ_{-3dB}
0.8	1.1	9,47483	-28.38	28.58	53.96	-23.22	18.42	41.64
0.8	1.2	10,29874	-24.03	24.03	48.06	-24.49	19.68	44.17
0.8	1.4	11,09983	-25.40	25.20	50.6	-27.02	24.62	51.64
1.2	1.1	8,41106	-30.23	30.52	60.75	-29.26	25.17	54.43
1.2	1.2	8,72157	-35.20	34.42	69.62	-18.74	26.82	45.56
1.2	1.3	8,67937	-30.82	29.64	60.46	-28.58	28.25	56.83
1.2	1.4	8,88579	-30.13	29.36	59.49	-22.08	20.95	43.04

From table 4-12 and figure 4-38 it can be seen that the gain enhancement of the patch is slightly influenced by the distance *h*, the optimum placement of the metamaterial lens is *h* = 0.8 cm away from the source. For that value of *h*, figure 4-38 shows that the better

antenna gain is obtained for a spherical cap radius r = 1.4 cm. However, for that value of r, figure 4-39 shows that the antenna radiation pattern in H-plan is more altered compared to that for r = 1.2 cm. For this reason we choose for the spherical metamaterial lens a height h = 0.8 cm and a cap radius r = 1.2 cm. The spherical metamaterial lens introduces a realized gain of 10.29 dB identical to that introduced by the SL lens (10.27 dB) and a little less than that introduced by the DLS lens (12.9 dB). Compared to the patch antenna alone, we have a realized gain improvement of more than 45% and a compared to the antenna with a DLS lens we have a gain reduction of 20%.

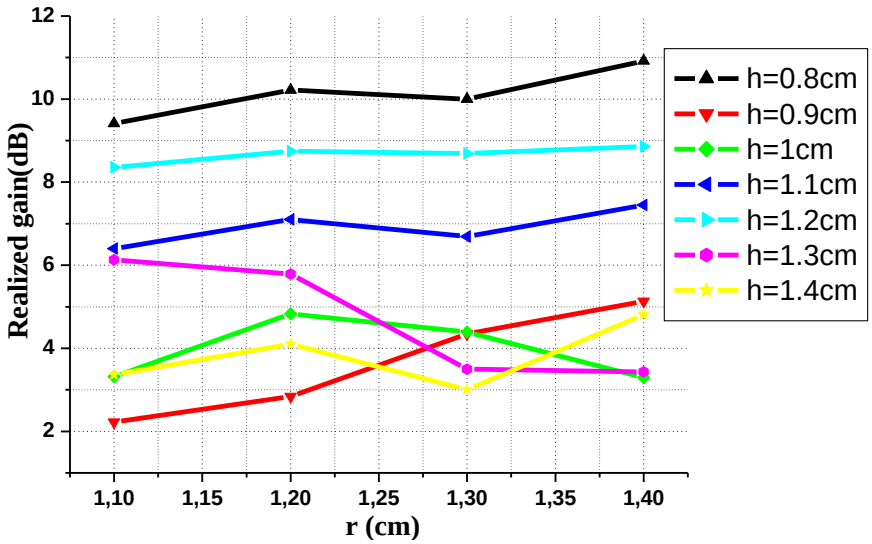

Figure 4-38: Realized gain of the antenna with spherical cap metamaterial lens for different values of h and r.

For r = 1.4 cm and h = 0.8 cm, the half-power beam width of the antennas, at the operating frequency, in E and H-plane respectively, is observed to be 50.6º and 51.64º. However, the half-power beam width of the antennas in E and H-plane respectively, for r = 1.2 cm and h = 0.8 cm, is observed to be 48.06º and 44.16º.

The return loss (S_{11}) for the conventional patch antenna and the antenna with the spherical metamaterial lens, are shown in figure 4-40. We observe that the antenna resonance frequency shifts slightly to low frequencies in the presence of the metamaterial cover. The antenna resonance frequency increases with the cap radius r, as it can be clearly seen from figure 4-40. It is about 43.14 Ghz for the antenna alone 42.6 Ghz for $r = 12$ mm and 42.72 Ghz for $r = 14$ mm.

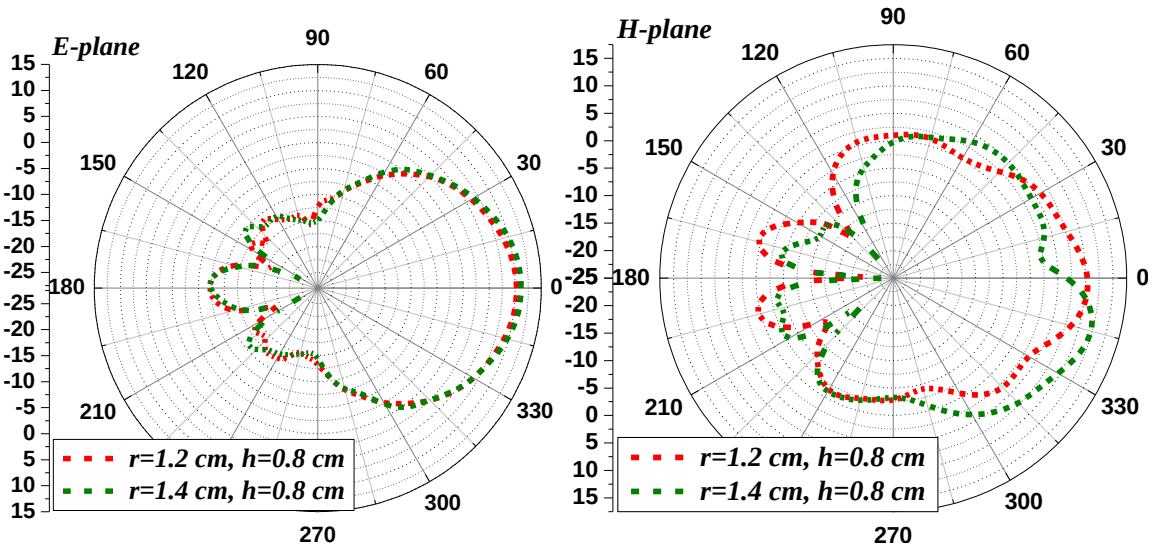

Figure 4-39: Radiation patterns, in the E and H-planes, of the patch with connected cross type metamaterial spherical cap lens for different spacing values *h* and *r*.

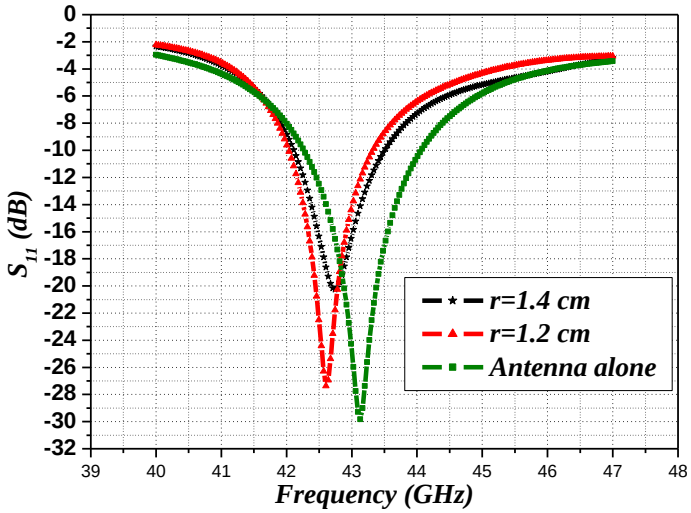

Figure 4-40: The Return loss (S_{11}) of the antenna with connected cross type metamaterial spherical cap lens.

4.5.2 Spherical cap shape lens based on disconnected cross type metamaterial

The characterization results of the spherical cap shape lens based on a disconnected cross type metamaterial are described in table 4-13.

Table 4-13: Characteristics of the patch antenna loaded with a cap lens based on disconnected cross metamaterial for different values of *r* and *h*.

			HPBW in E-plane			HPBW in H-plane		
h (cm)	*r* (cm)	Realized gain (dB)	θ_i	θ_s	θ_{-3dB}	φ_i	φ_s	φ_{-3dB}
0.9	1.1	10,31183	-26.21	27.21	53.52	-18.16	16.01	34.17
0.9	1.2	9,51867	-22.64	22.93	45.57	-21.18	19.33	40.51
0.9	1.3	9,45706	-22.15	19.62	41.77	-25.95	23.2	4915
0.9	1.4	9,73199	-23.22	21.08	44.3	-28.14	23.22	51.3
1.3	1.2	8,42368	-36.5	28.67	64.17	-23.03	22.54	45.58
1.3	1.3	8,84824	-38.02	39.19	77.21	-29.07	30.04	59.47
1.3	1.4	8,95996	-34.61	33.74	68.35	-24.68	26.5	51.18

The simulation results indicate that the gain of the proposed antenna increases significantly in comparison to the antenna alone.

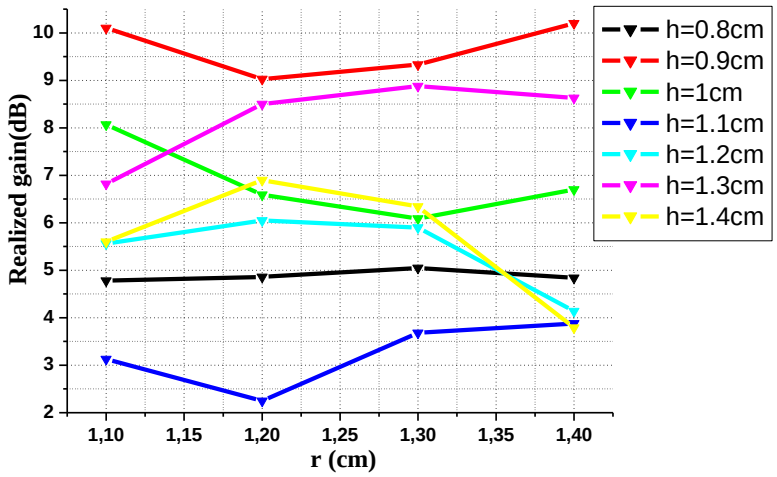

Figure 4-41: Realized gain of metamaterial of the antenna with a spherical cap lens based on a disconnected cross type metamaterial for different spacing *h*.

It is clear from figure 4-41 and table 4-13, that the maximum realized gain is found at $h = 0.9$ cm and $r = 1.1$ cm for the spherical cap lens with disconnected cross type metamaterial. However the main lobe is more directional of the antenna with a lens based on the connected cross type metamaterial compared to that of the antenna with a lens based on the disconnected cross type metamaterial.

4.5.3 Influence of the focusing zone

We recall that the focusing zone is based on disconnected cross type metamaterial, while the lens body is based on connected cross type metamaterial. In order to choose the optimal size of the focusing zone, we changed h_z the height of the latter in the middle position P_0. The results obtained are summarized in table 4-14. The simulation results of the radiation pattern for different values of the FZ height h_Z are shown in figure 4-42 and 4-43.

Table 4-14: Characteristics of the patch antenna loaded with spherical lens based on connected cross type metamaterial with FZ for different values of h_z.

		HPBW in E-plane			HPBW in H-plane			
h_Z (cm)	Realized gain (dB)	θ_i	θ_s	θ_{-3dB}	φ_i	φ_s	φ_{-3dB}	Bandwidth (%)
0.4	12,37902	-11.44	11.34	22.78	-10.17	8.81	18.98	3.2
0.35	12,6975	-11.43	11.36	22.79	-10.14	8.89	19.03	3.06
0.3	12,60421	-12.07	11.38	23.45	-9.88	9.10	18.98	2.88
0.25	12,52767	-11.63	11.15	22.78	-10.14	8.83	18.97	2.53
0.2	12,21248	-14.16	13.68	27.84	-10.15	10.07	20.22	2.21
0.15	11,04075	-15.43	14.94	30.37	-12.51	11.53	24.04	2.1
0.1	8,36214	-18.84	19.13	37.97	-15.25	15.14	30.39	2.18

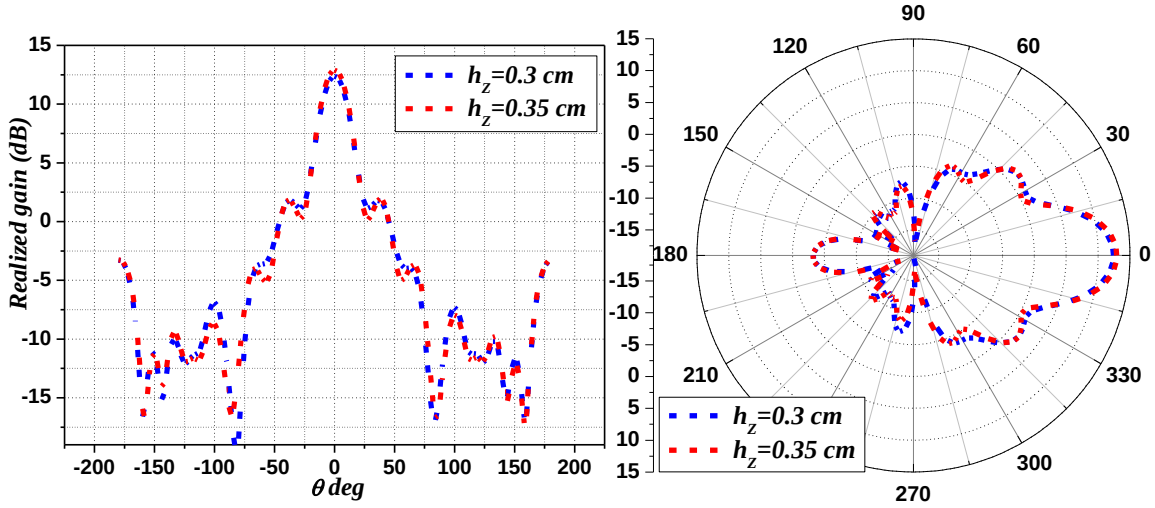

Figure 4-42: Radiation pattern in the E-plane for the antenna with a spherical metamaterial lens and focusing zone for different values of h_Z.

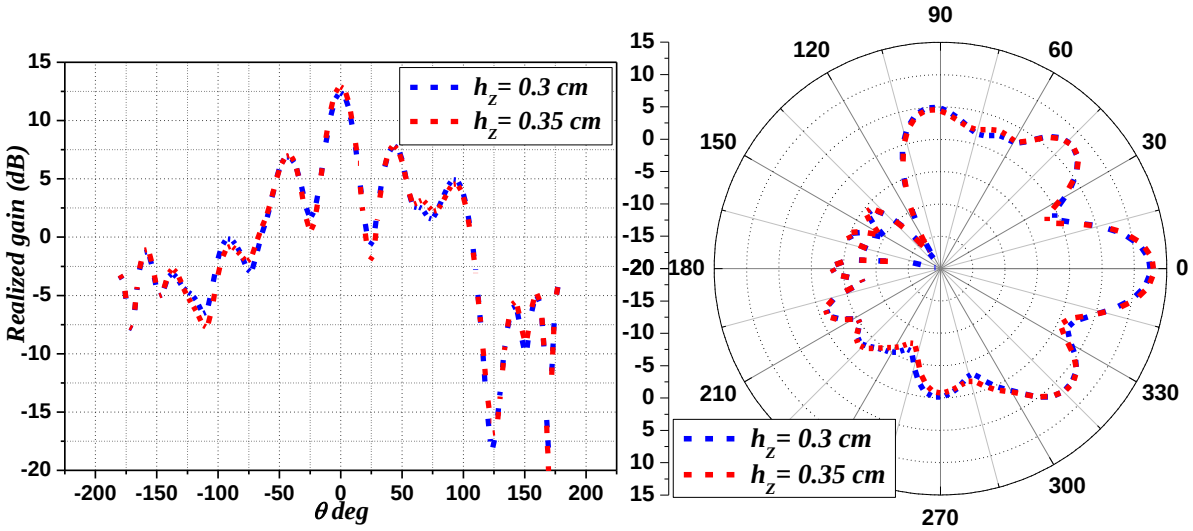

Figure 4-43: Radiation pattern in the H-plane for the antenna with a spherical metamaterial lens and focusing zone for different values of h_Z.

We note from table 4-14, figure 4-42, and 4-43, that the main lobe is more directional and the maximum realized gain is 12.69 dB for h_Z = 0.35 cm.

The 3D radiation pattern of the antenna alone and the antenna with SLS, DLS, and spherical cap metamaterial are shown in figure 4-44.

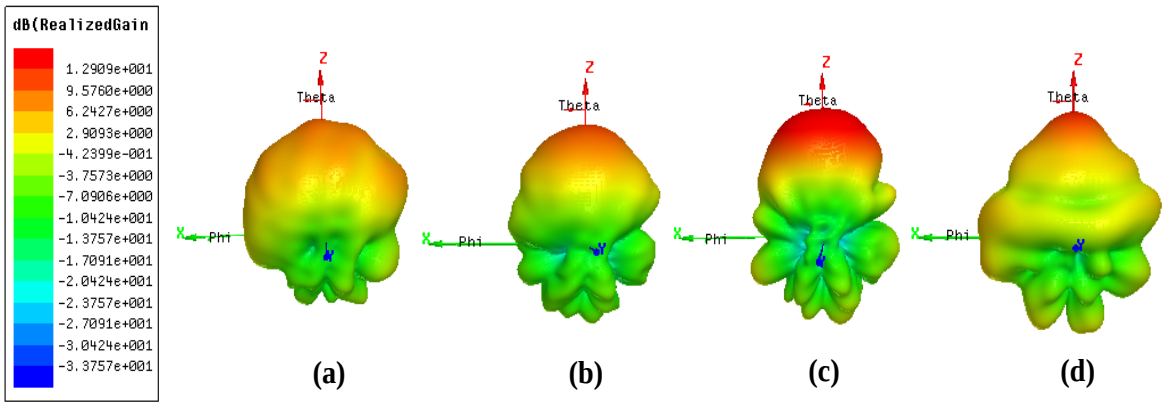

Figure 4-44: 3D radiation pattern of: (a)-antenna alone, (b)-antenna with metamaterial SLS, (c)-antenna with DLS, (d)- antenna with metamaterial spherical lens.

4.5.4 Antenna radiation pattern control with a spherical cap metamaterial

For the spherical cap it suitable to locate the focusing zone FZ using the spherical coordinate. Since the focusing zone is always at distance *r* from the patch antenna, its position is determined by two angle θ_{FZ}, the angle between the *z*-axis and the line connecting the origin (center of the patch antenna) and the center of the focusing zone, and φ_{FZ}, the polar angle (see figure 4-45). The spherical coordinates (θ_{FZ}, φ_{FZ}) for the different FZ positions are reported in table 4-15.

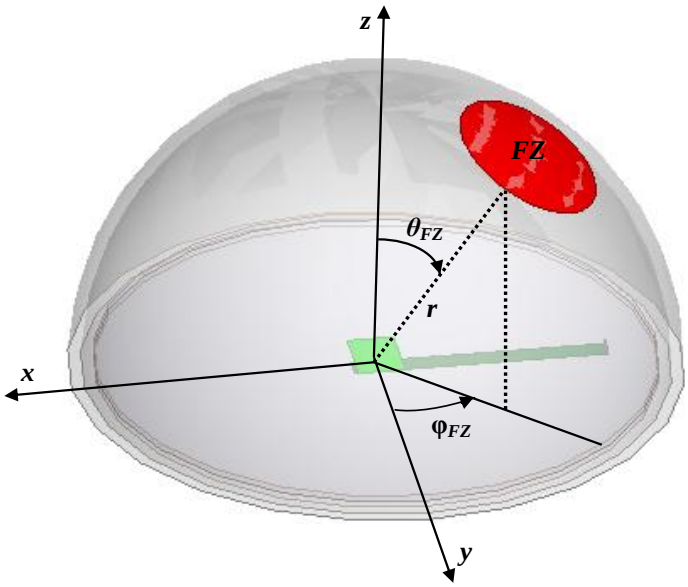

Figure 4-45: Focusing zone position in the spherical coordinates.

Table 4-15: Characteristics of the spherical lens antenna for the different focusing zone positions.

	FZ Position		E-plane			H-plane			Realized gain (dB)
	φ_{FZ}^{0}	θ_{FZ}^{0}	θ_{max}	θ_{-3dB}		φ_{max}	φ_{-3dB}		
				θ_i	θ_r		φ_i	φ_r	
Position P_0	0	0	0.19	11.44	11.34	0.19	10.17	8.81	12,69
	0	15	-15.18	-32.89	2.53	-1.07	-11.19	11.58	10.08
Position P_1	0	30	-30.55	-47.05	-11.58	-1.07	-24.56	23.36	9.62
	0	45	-10.02	-29.07	6.42	-1.07	-11.17	10.31	9.49
	0	-15	15.57	-2.14	33.28	0.19	-11.19	11.58	10.07
Position P_2	0	-30	30.94	11.97	47.39	0.19	-24.62	23.45	9.61
	0	-45	10.41	-6.03	29.39	1.07	-11.19	10.31	9.39
	90	15	0.19	-20.24	20.72	20.72	6.81	35.91	10.52
Position P_3	90	30	0.19	-21.19	20.56	36.18	22.18	50.02	10.99
	90	45	0.19	-18.78	19.17	13.04	-2.14	33.28	10.11
	90	-15	0.19	-24.13	25.78	-35.61	-50.80	-21.70	10.95
Position P_4	90	-30	0.19	-21.11	20.63	-36.78	-20.39	-50.15	10.42
	90	-45	0.19	-18.78	19.9	-12.55	-30.26	-1.16	10.12
	-45	15	-18.85	-42.73	7.76	18.12	1.64	37.23	8.84
Position P_5	-45	30	-33.11	-49.56	-1.52	34.68	19.55	49.84	8.57
	-45	45	-7.27	-26.39	10.28	10.46	-2.23	30.61	7.41
	45	15	18.17	-7.1	42.23	18.19	1.75	37.17	8.96
Position P_6	45	30	33.47	-1.94	49.92	34.74	19.56	49.92	8.68
	45	45	7.88	-9.82	26.85	10.51	-2.14	30.75	7.33
	45	-15	-18.97	-42.82	7.85	-17.71	-37.95	-1.26	8.48
Position P_7	45	-30	-33.08	-49.53	-1.45	-34.35	-49.63	-19.26	8.56
	45	-45	-7.36	-26.37	10.31	-10.02	-30.26	1.36	7.22
	-45	-15	18.21	-7.24	42.17	-17.84	-37.88	-1.27	8.51
Position P_8	-45	-30	33.44	-1.96	49.56	-34.44	-49.74	-19.31	8.64
	-45	-45	7.79	-9.78	26.71	-10.11	-30.31	1.41	7.35

Figure 4-46 and 4-47, illustrate the radiation pattern steering of the metamaterial patch antenna for different positions of the focusing zone in E and H-planes.

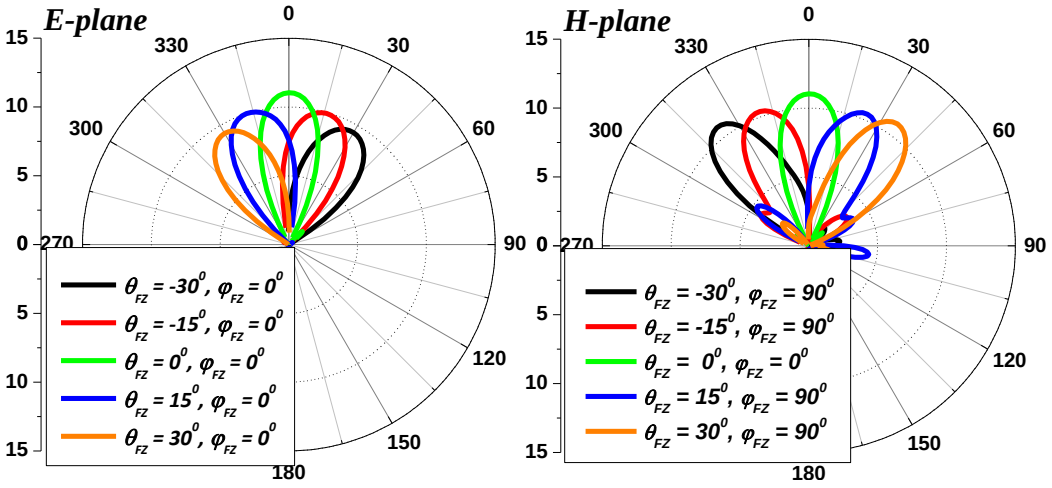

Figure 4-46: Radiation pattern steering for φ=0° and φ=90°.

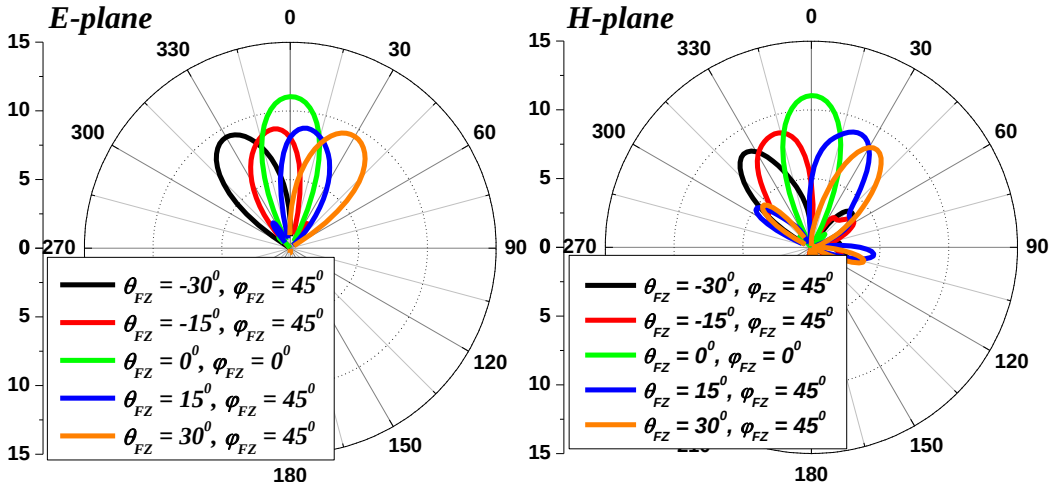

Figure 4-47: Radiation pattern steering for φ=45°.

As it can be seen from figure 4-46 and 4-47, that the maximum rotation angle for the radiation pattern is ±30° in E-plane, obtained for FZ at (θ_{FZ} = ±30°, φ_{FZ} = 0°), and±36° in H-plane obtained for and FZ at (θ_{FZ} = ±30°, φ_{FZ} = 90°). The different FZ positions for which the radiation patter main lobe rotation angle is maximal, are represented in figure 4-48.

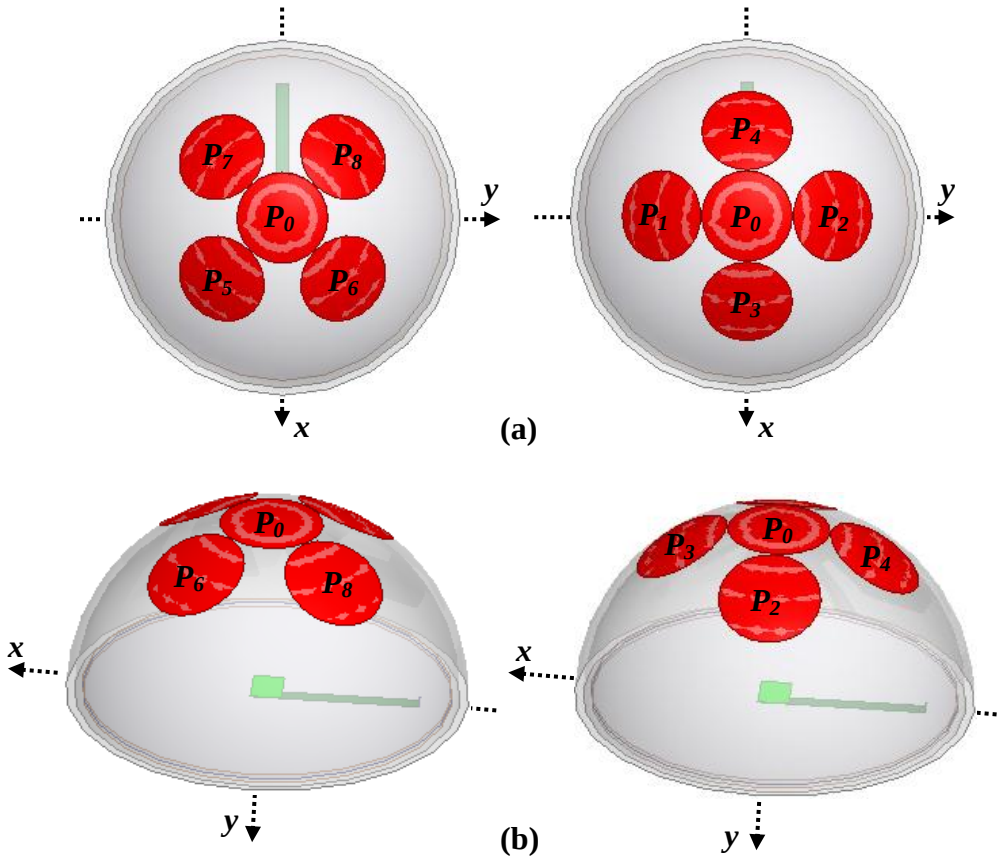

Figure 4-48: The different positions of the FZ: (a)-top Views, (b)-Side views

Figure 4-49 and 4-50, shows the radiation pattern steering, obtained by positioning the FZ when placed between positions P_1 and P_2.

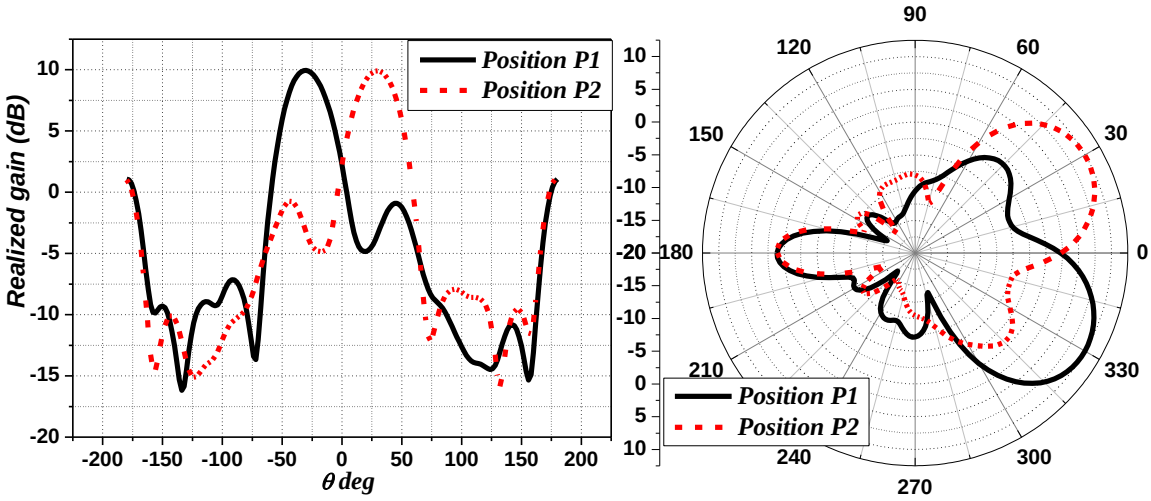

Figure 4-49: Radiation pattern steering in the E-plane by positioning the FZ (P1 and P2).

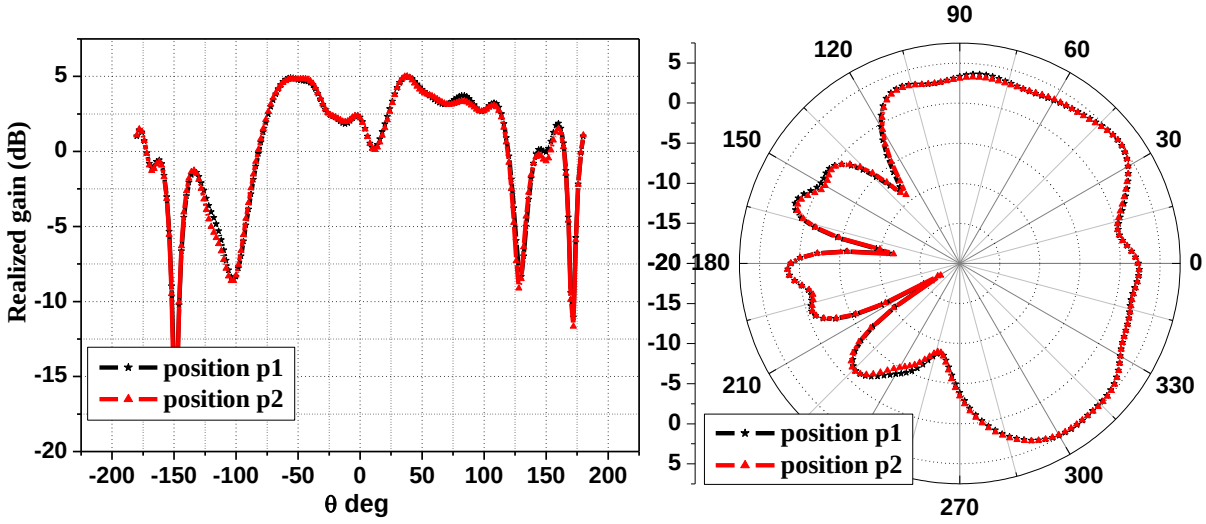

Figure 4-50: Radiation pattern steering in the H-plane by positioning the FZ (P_1 and P_2).

When the FZ is positioned between P_1 and P_2, it acts only on the E-plane of the radiation pattern. The main lobe is rotated on both sides of the direction $\theta = 0°$. The amplitude of the rotation angle is about 30°, as shown in figure 4-49 and 4-50. However, when the FZ is placed between P_3 and P_4, it acts only on the H-plane of the radiation pattern, as it can be seen in figure 4-51 and 4-52. The radiation pattern main lobe is rotated on both sides of the mid-position with a rotation angle amplitude of about 36°. As for the planar metamaterial lens (SLS and DLS lens), figure 4-53 to 4-56 show that the FZ acts on both E- and H-plane of the radiation pattern, when it is placed between P_6 and P_7 and between P_5 and P_8. The rotation angle amplitude of the main-lobe pointing angle is about 33° in both E- and H-planes. The spherical shape metamaterial lens radiation pattern control is recapitulated in table4-16 where are reported the FZ positions and the amplitude of the main lobe rotation angle.

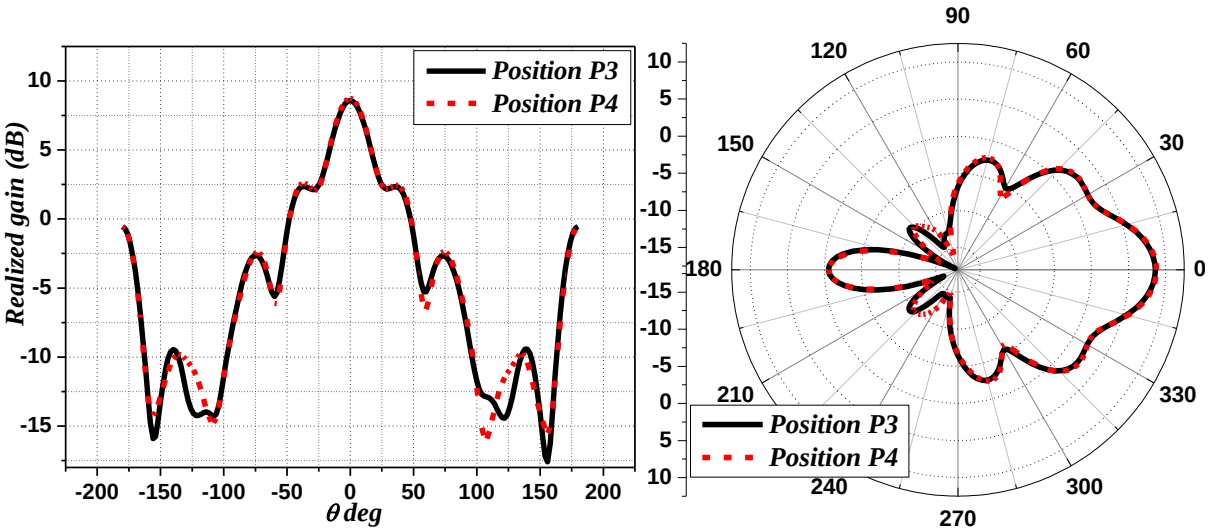

Figure 4-51: Radiation pattern steering in the E-plane by positioning the FZ (P_3 and P_4).

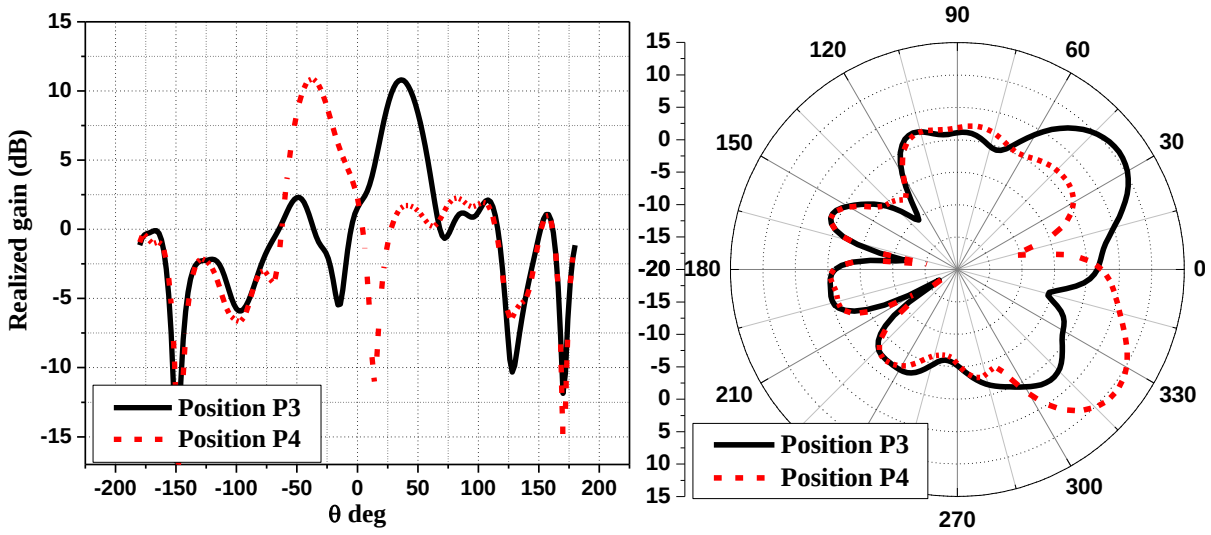

Figure 4-52: Radiation pattern steering in the H-plane by positioning the FZ (P_3 and P_4).

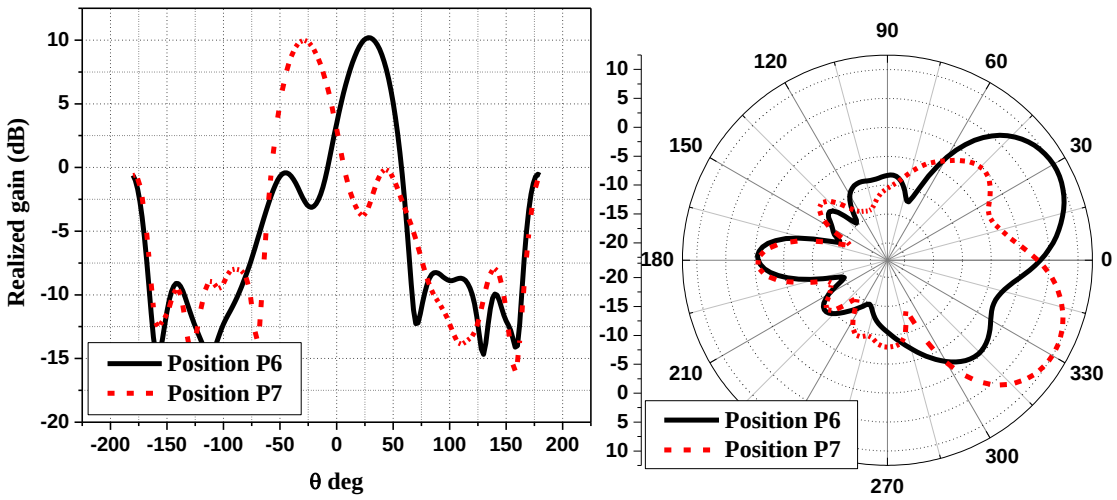

Figure 4-53: Radiation pattern steering in the E-plane by positioning the FZ (P_6 and P_7).

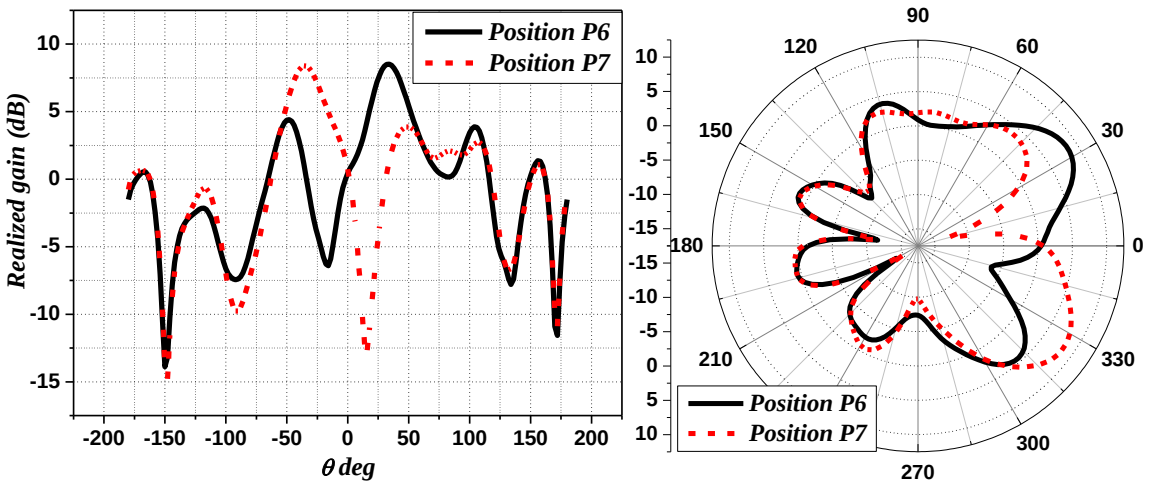

Figure 4-54: Radiation pattern steering in the H-plane by positioning the FZ (P6 and P7).

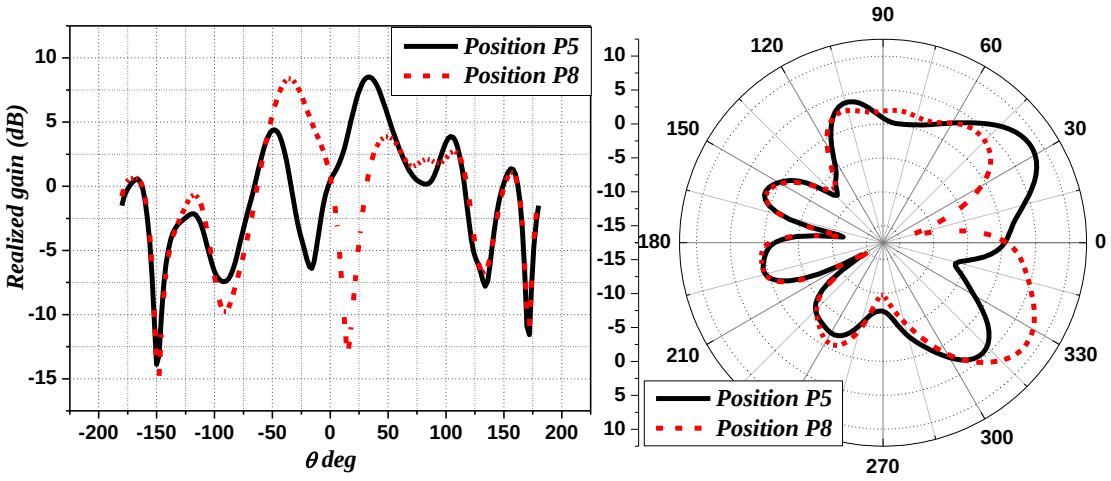

Figure 4-55: Radiation pattern steering in the H-plane by positioning the FZ (P_5 and P_8).

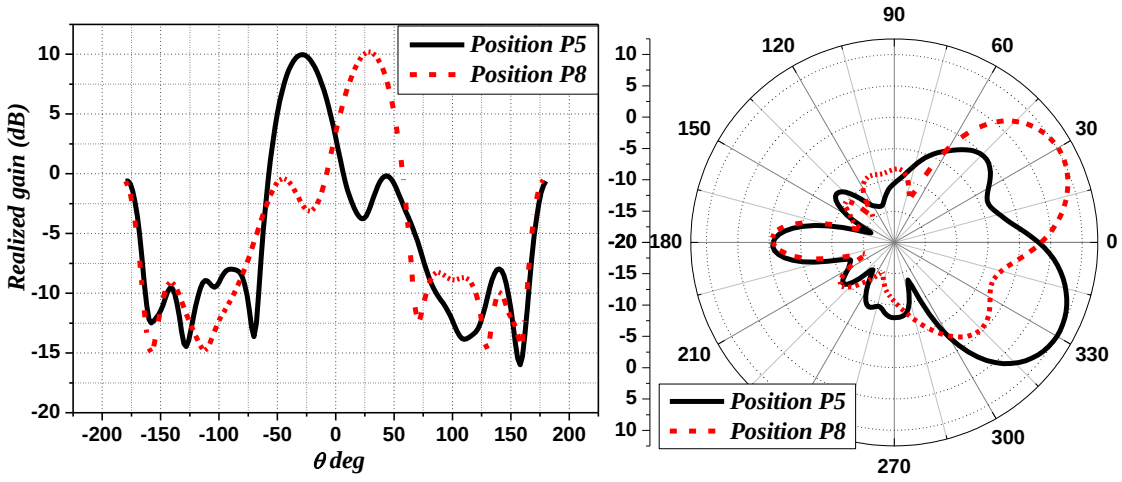

Figure 4-56: Radiation pattern steering in the E-plane by positioning the FZ (P_5 and P_8).

Table4-16: Radiation pattern main lobe direction angle versus FZ positions.

FZ positions	E-Plane θ_{max} (deg)	H-Plane φ_{max} (deg)
P_1	-30	0
P_2	30	0
P_3	0	36
P_4	0	-36
P_5	-33	33
P_6	33	33
P_7	-33	-33
P_8	33	-33

4.6 Conclusion

In this chapter we have examined and demonstrated the possibility of controlling the antenna radiation pattern using an agile metamaterial lens. The lens enables, also, to enhance the antenna gain compared to the antenna alone. The obtained results show that:

i) The near zero refraction index metamaterial based on connected cross unit cell (switch ON) concentrate the radiated waves produced by the patch antenna and consequently, increases the antenna gain,

ii) The maximum antenna realized gain obtained is 10.27 dB with an SLS, while it reaches 12.90 dB with a DLS, and 12.69 dB with spherical cap lens in the presence of the FZ.

iii) The antenna gain and the amplitude of main-lobe pointing angle depend on the geometry of the metamaterial lens placed above the patch antenna (planar lens and spherical cap lens),

iv) The antenna radiation pattern is controlled by positioning the metamaterial lens focusing zone.

Conclusion

Our goal in this work is to exploit the potential offered by the metamaterials to design an agile radiation pattern antenna. These metamaterials are artificial periodic structures which it is possible to tailor their electromagnetic response. Using this agile metamaterial we design an agile lens to enhance a microstrip patch antenna gain and control its radiation pattern. The agile metamaterial lens is made up of two regions; the first one forms a focusing zone and the second one, the lens body (host medium). By changing the parameters of the focusing zone (size, position) we control the patch antenna's radiation-pattern main-lobe beam width and direction (pointing angle) in E- and H-planes.

We have design an agile metamaterial lens which has two different behaviors and they can be controlled through external command system. This agile metamaterial lens is obtained by a periodic structure based on agile cross unit cells. The agility of this metamaterial unit cell is achieved by disconnecting or connecting the wires of the cross type conductor forming the unit cell. The metamaterial based on connected and disconnected cross unit cells behaves, respectively, as an effective medium with an refraction index close to zero (n_1) and greater than unity (n_2). With this agile unit cell we have design a layer metamaterial in which each pixel can be programmed individually and independently from the others. It is thus possible to program in the planar metamaterial different zones where the refractive index can be set (selected) to the desired value n_1 or n_2. This programmable metamaterial surface forms an agile lens composed of a host matrix with refractive index n_2, and a focusing zone with refraction index n_1, whose shape and size are programmable.

We have "tailored" the agile elementary unit cell to meet the requested metamaterial electromagnetic behavior in the operating frequency band: i) as an effective medium having a refractive index close to zero for the connected cross type metamaterial, ii) as an effective medium having a refractive index greater than unity ($n = 1.7$) for the disconnected cross type metamaterial. The desired metamaterial electromagnetic behavior is obtained by varying the different unit cell parameters (the period *a*, the dielectric thickness *d*, the conductor strip width *w*, the metallization thickness *t*, and the cross disconnection *g* (the gap). Once the metamaterial tailored to the desired behavior, we used it to design the agile lens used to enhance a microstrip antenna gain and control its radiation-pattern. The agile metamaterial lens optimization consists to determine its shape (planar or spherical), the numbers of layers (single or double), the spacing between the lens and the source, and between the layers and the size and position of the focusing zone.

Finally we have demonstrated the possibility of steer and control the antenna radiation pattern by modifying the focusing zone parameters. The obtained results show that:

i) For the antenna with DLS metamaterial lens, the maximum realized gain obtained is 12.9 dB. The half power beam width in E and H planes, respectively are about 47º and 32. The main lobe can be rotated by about 47º, in both side of the central direction, in E-plane and 32º, in both side of the central direction, in H-plane.

ii) For the antenna with SLS metamaterial lens, the maximum realized gain is found to be 10.27 dB. The half power beamwidth of the antenna at the operating frequency in E and H planes is observed to be about 50° and 56°, respectively. In both E and H planes, the mean lobes can be rotated by about 28º, in both side of the central direction.

iii)For the antenna with spherical cap shape lens, the maximum realized gain is 12.69 dB. The half power beamwidth of the antenna in E and H plane is about 23º and 19º, respectively. The mean lobes can be rotated by 33º in E-plane and 37º in H-plane, in both side of the central direction.

From the comparison we found that the realized gain obtained of the antenna with spherical cap shape lens is nearly the same as of which in the antenna with DLS. As it can be see that there is a contrast of 14º in the beam steering between the antenna with spherical cap shape lens and the antenna with DLS lens in E-plane. However, the antenna with spherical cap shape lens is directional and has a narrow main lobe and is more aerodynamically and mechanically stable, compared to the antenna with SLS and DLS. For this reason, we prefer to use the antenna with spherical cap shape lens.

Abbreviations List

$\vec{E}$:	Electric filed
$\vec{H}$:	Magnetic field
$\vec{D}$:	Dielectric displacement
$\vec{B}$:	Magnetic defacement
n :	Refractive index
ε :	Electric permittivity
μ :	Magnetic permeability
ζ_0 :	Magneto-electric coupling coefficient
$\vec{n}$:	Director
α :	Attenuation
β :	Propagation constant
Z :	Impedance
z :	Normalized impedance
z_0 :	Impedance in vacuum
z^+ :	Forward wave impedance
z^- :	Backward wave impedance
k :	The wavenumber
ω_{pe} :	The electric plasma frequency
Γ_e :	Damping constant electric
c_0	Speed of light in vacuum ≈ 3 x 10^8 m/s
ω_{pm} :	The magnetic plasma frequency
ω_{0m} :	Magnetic resonance frequency
Γ_m :	Damping constant magnetic
δ :	Radial spacing between the rings
$P(x)$:	Polarization
$M(x)$:	Magnetization
ε_c :	Uniform permittivity

μ_c : Uniform permeability

Γ_A : Reflection coefficient in the reference planes Z=A

Γ_B : Reflection coefficient in the reference planes Z=B

Γ_C : Reflection coefficient in the reference planes Z=C

Γ_D : Reflection coefficient in the reference planes Z=D

T : Transmission coefficient

m : Branch index

References

[1] Veselago, V.G, ‘‘Electrodynamics of substances with simultaneously negative values of sigma and mu,’’ Sov Phys Usp 10, 509–514 (1968).

[2] Smith DR, Padilla WJ, Vier DC, Nemat-Nasser SC, Schultz S, ”Composite medium with simultaneously negative permeability and permittivity, ” Phys Rev Lett 84:4184–4187.

[3] Pendry, ”Negative refraction makes a perfect lens, ” Phys Rev Lett 85:3966–3969.

[4] Von Hippel, and R. Arthur, “Dielectrics and Waves,” Cambridge, MA: MIT Press, 1954.

[5] Balanis, C, “Advanced Engineering Electromagnetics,” New York: John Wiley & Sons,1989, pp. 44--60.

[6] Engheta, N., and R. Ziolkowski, (eds.), “Metamaterials Physics and Engineering Explorations,” New York: John Wiley & Sons, 2006.

[7] Wiltshire, M. C. K., ‘‘Bending of Light in the Wrong Way,’’ Science, 292, 2001, p.60-61

[8] www.wave-scattering.com/negative.html.

[9] Lamb, H., ‘‘On Group-Velocity,’’ Proc. London Math.Soc. 1, 1904, pp. 473--479.

[10] Veselago, V. G., and E. E. Narimanov, ‘‘The Left Hand of Brightness: Past, Present andFuture of Negative Index Materials,’’ Nature Materials 5, 2006, pp. 759--762.

[11] Sihvola, A., ‘‘Metamaterials in Electromagnetics,’’ Metamaterials, Vol. 1, Issue 1, 2007,pp. 2--11.

[12] Shamonina, E., and L. Solymar, ‘‘Metamaterials: How the Subject Started,’’ Metamaterials, Vol. 1, Issue 1, 2007, pp. 12--18.

[13] Yang Hao, Raj Mittra, ‘‘FDTD Modeling of Metamaterials Theory and Applications, ’’ British Library, ISBN-13: 978-1-59693-160-2.

[14] Kock, W, ‘‘Metallic delay lenses,’’ Bell Syst. Tech. J., Vol. 27, 1948, pp. 58--82.

[15] Rudge, A. W., et al, ‘‘The Handbook of Antenna Design,’’ Volume II, London,U.K.: Peter Peregrinus Ltd., 1983.

[16] Brown, J., ‘‘Artificial Dielectrics,’’ Progress in Dielectrics, Vol. 2, 1960, pp. 195-225.

[17] Rotman, W, ‘‘Plasma Simulations by Artificial Dielectrics and Parallel-Plate Media,’’ IRETrans. Ant. Propag., Vol. 10, 1962, pp. 82--95.

[18] J. B. Pendry, A. J. Holden, W. J. Stewart, and I. Youngs.Extremely low frequency plasmons in metallic mesostructures.PhysicalReviewLetters, vol. 76, no. 25, pp. 4773–4776, 1996.

[19] J. B. Pendry, A. J. Holden, D. J. Robbins, and W. J. Stewart,’’Magnetism from conductors and enhanced nonlinear phenomena,’’ IEEE Transactions on Microwave Theory and Techniques, vol. 47, no. 11, pp. 2075–2084, 1999.

[20] J.Pendry, A.Holden, D.Robbins, and W.Stewart, ‘‘Low frequency plasmons in thin-wire structures,’’ Journal of Physics: Condensed Matter, vol. 10, p. 4785, 1998.

[21] H. S. Chen, L. X. Ran, J. T. Huangfu et al, ‘‘Left-handed materials composed of only S-shaped resonators,’’ Physical Review E, vol. 70, no. 5, Article ID 057605, 2004.

[22] C.Caloz, T.Itoh, ‘‘Electromagnetic metamaterials transmission line theory and microwave applications,’’ The Engineering approach, a john wiley & Sons, INC. 2006.

[23] N. Engheta, R. W. Ziolkowski, ‘‘Metamaterials Physics and engineering explorations,’’IEEE.2006.

[24] Schelkunoff, S., and H. Friis, ‘‘Antennas Theory and Practice,’’ New York: John Wiley &Sons, 1952.

[25] Schneider, H. J., and P. Dullenkopf, ‘‘Slotted Tube Resonator: A New NMR Probe Headat High Observing Frequencies,’’ Rev. Sci. Instrum., Vol. 48, No. 1, 1977, p. 68-73.

[26] Hardy, W. H., and L. A. Whitehead, ‘‘Split ring resonator for use in magnetic resonance from 200-2000 MHz,’’ Rev. Sci. Instrum, Vol. 52, No. 2, 1981, pp. 213--216.

[27] Kostin, M. V., and V. V. Shevchenko, ‘‘Artificial Magnetics Based on Double Circular Elements,’’ Proc. of Bianisotropics ’94, Perigueux, France, 1994, pp. 49--56.
[28] Marques, R., et al., ‘‘Left-Handed-Media Simulation and Transmission of EM Wavesin Subwavelength Split-Ring-Resonator-Loaded Metallic Waveguides,’’ Phys. Rev. Lett.,Vol. 89, No. 18, 2002, p. 183901.
[29] Hrabar, S., J. Bartolic, and Z. Sipus, ‘‘Waveguide Miniaturization Using Negative Permeability Material,’’ IEEE Trans. Antennas Propagat., Vol. 53, N. 1, 2005, p 110-119.
[30] PrathabanMookiah, and Kapil R. Dandekar “Metamaterial substrate antenna array for MIMO communication system,” IEEE transactions on antennas and propagation, vol. 57, no. 10, October 2009
[31] ShridharE.Mendhe and Yogeshwar Prasad Kosta, ‘‘Metamaterial properties and applications,’’ International journal of information technology and knowledge management January-June 2011, Volume 4, No. 1, pp. 85-89
[32] S. Raghavan and V. Rajeshkumar, ‘‘An overview of metamaterials in biomedical applications,’’ Piers Proceedings, Taipei, March 25-28, 2013
[33] T. J.Cui , D.R.S mith, R.Liu, ‘‘Metamaterials Theory Design and Applications,’’ Springer.2010.
[34] N. Engheta, R. W. Ziolkowski, ‘‘Metamaterials Physics and engineering explorations,’’ IEEE.2006.
[35] T. J.Cui , D.R.S mith, R.Liu, ‘‘Metamaterials Theory, Design, and Applications,’’ Springer.2010.
[36] Steven M. Anlage, ‘‘The physics and applications of superconducting metamaterials,’’
[37] Shamonina, E., Solymar, L, ‘‘Properties of magnetically coupled metamaterial elements. ,’’ J.Magn. Magn.Mater. 300, 38–43 (2006).
[38] Syms, R.R.A., Shamonina, E., Kalinin, V., Solymar, L, ‘‘A theory of metamaterials based on periodically loaded transmission lines: interaction between magneto inductive and electromagnetic waves,’’ J. Appl. Phys. 97, 064909 (2005).
[39] Baena, J.D., Jelinek, L., Marques, R., Mock, Gollub, J., Smith, D.R, ‘‘Isotropic frequency selective surfaces made of cubic resonators,’’Appl Phys. Lett. 91, 191105 (2007).
[40] Alu, A., Engheta, N, ‘‘Achieving transparency with plasmonic and metamaterial coatings,’’ Phys. Rev. E 72, 016623 (2005)
[41] Milton, G.W., Nicorovici, N.P, ‘‘On the cloaking effects associated with anomalous localized resonance,’’ Proc. R. Soc. A 462, 3027–3059 (2006).
[42] Leonhardt, U, ‘‘Optical conformal mapping,’’ Science 312, 1777–1780 (2006)
[43] Pendry, J.B., Schurig, D., Smith, D.R, ‘‘Controlling electromagnetic fields,’’ Science 312,1780–1782 (2006).
[44] Greenleaf, A., Lassas, M., Uhlmann, G, ‘‘non-uniqueness for Calder´on’s inverse problem,’’ Math. Res. Lett. 10, 685–693 (2003)
[45] Greenleaf, A., Lassas, M., Uhlmann, G, ‘‘Anisotropic conductivities that cannot be detected by EIT,’’ Physiol. Meas. 24, 413–419 (2003)
[46] Cummer, S.A., Popa, B.-I., Schurig, D., Smith, D.R., Pendry, J, ‘‘Full-wave simulations of electromagnetic cloaking structures,’’ Phys. Rev. E 74, 036621 (2006)
[47] Schurig, D., Mock, J.J., Justice, B.J., Cummer, S.A., Pendry, J.B., Starr, A.F.S., Smith, D.R, ‘‘Metamaterial electromagnetic cloak at microwave frequencies,’’ Science 314, 977–980 (2006)
[48] Liang, Z., Yao, P., Sun, X., Jiang, X, ‘‘The physical picture and the essential elements of the dynamical process for dispersive cloaking structures,’’ Appl. Phys. Lett. 92, 131118 (2008).
[49] Lee, H.-J., Yook, J.-G, ‘‘Biosensing using split-ring resonators at microwave regime,’’ Appl.Phys. Lett. 92, 254103 (2008)

[50] O'Hara, J.F., Singh, R., Brener, I., Smirnova, E., Han, J., Taylor, A.J., Zhang, W, ''Thin-film sensing with planar terahertz metamaterials: sensitivity and limitations,'' Opt. Express 16,1786–1795 (2008)
[51] Chen, C.M., Huang, Y, ''High Accuracy Theory of Finite Element Methods,'' (in Chinese).Hunan Science Press, China (1995)
[52] Cai, W., Shalaev, V, ''Optical Metamaterials Fundamentals and Applications,'' Springer, New York (2009)
[53] Information on frequency selective surfaces http://www.ofcom.org.uk.
[54] B. Hooberman, ''Everything you ever wanted to know about frequency-selective surface filters but were afraid to ask,'' 2005.
[55] Ben A. Munk, ''Frequency Selective Surfaces: Theory and Design,'' 1st ed. (New York: John Wiley & Sons, Inc., 2000.)
[56] John D. Kraus and Ronald J. Marhefka, ''Antennas for all Applications,'' 3rd ed. (New York: McGraw-Hill, 2002.)
[57] Z.Sahraoui, ''Les antennes agiles à base de metamateriaux,'' Universite Amar Telidji Laghouat.Thesis2013.
[58] T. J. Cui, D. R. Smith, and R. Liu, "Metamaterials Theory, Design, and applications," Springer, 2010.
[59] Alireza V. Amirkhizi, and Sia Nemat-Nasser, "Microstructurally based homogenization of electromagnetic properties of periodic media," Science Direct. C. R. Mecanique 336 (2008) 24–33
[60] L. Solymar E and Shamonina, "Waves in Metamaterials," Oxford. 2009
[61] Wenshan Cai and Vladimir Shalaev, "Optical Metamaterials Fundamentals and Applications". Springer. 2010.
[62] S. Arslanagić, T. V. Hansen , N. A. Mortensen, A. H. Gregersen, O. Sigmund, R. W. Ziolkowski , and O. Breinbjerg, "A review of the scattering parameter extraction method with clarification of ambiguity issues in relation to metamaterial homogenization,". The Danish Research Council for Technology and Production Sciences.2012.
[63] U. C. Hasar and J J. Barroso, "Retrieval approach for determination of forward and backward wave impedances of bianisotropic metamaterials," Progress In Electromagnetics Research, Vol. 112, 109-124, 2011
[64] Christine Eliane Kriegler, Michael Stefan Rill, Stefan Linden, and Martin Wegener, "Bianisotropic Photonic Metamaterials, " IEEE JOURNAL OF SELECTED TOPICS IN QUANTUM ELECTRONICS, VOL. 16, NO. 2, MARCH/APRIL 2010.
[65] Zhenya Lei, Rui Yang, Xiaowei Shi, and Jiawei Zhang, "Determining the effective electromagnetic parameters of bianisotropic metamaterials with periodic structures," Progress In Electromagnetics Research M, Vol. 29, 79-93, 2013.
[66] Li, Z., K. Aydin, and E. Ozbay, "Determination of the effective constitutive parameters of bianisotropic metamaterials from reflection and transmission coeffcients, " Phys. Rev. E, Vol.79, 026610-1-7, 2009.
[67] Constantine, A. B, "Advanced Engineering Electromagnetics," John Wiley & Sons, 1989.
[68] Grzegorczyk, T. M., X. Chen, J. Pacheco, J. Chen, B.-I. Wu, and J. A. Kong, "Reflection coeffcients and Goos-Hanchen shifts in anisotropic and bianisotropic left-handed metamaterials, " Progress In Electromagnetics Research, Vol. 51, 83-113, 2005.
[69] Barroso, J. J. and U. C. Hasar, "Resolving phase ambiguity in the inverse problem of transmission/reflection measurement methods," Int. J. Infrared Milli. Waves, Vol. 32, 857-866, 2011.
[70] D. R. Smith, "Electromagnetic parameter retrieval from inhomogeneous metamaterials," Department of Electrical and Computer Engineering, Duke University, Box 90291, Durham, North Carolina 27708, USA, Physical review E 71, 036617 s2005d

[71] C.croenne, J.Mlerat, N.Malléjac, O.Acher,D.Lippens,"Extraction ab-initio effectifs parameters of metamaterial, " journal of microonde
[72] L. Chen, Z. Lei, R. Yang, X. Shi, and J. Zhang, "Determining the effective electromagnetic parameters of bianisotropic metamaterials with periodic structures," Prog. Electromagn. Res. 29, 79–93 (2013).
[73] E. Erfani, J. Nourinia, C. Ghobad, M. Niroo-Jazi and T. A. Denidni, "Design and Implementation of an Integrated /Reconfigurable-Slot Antenna for Cognitive Radio Applications," IEEE on Anf. and Wireless Propag. Lett., Vol. 11, p. 77-80, March 2012.
[74] K. Boyon, P. Bo, S. Nikolaou, K. Young-Sik, et al., "A Novel Single-Feed Circular Microstrip Antenna With Reconfigurable Polarization Capability," IEEE Trasn. On Anf. and Propag., Vol. 56 (No. 3), p. p. 630-638, 2008.
[75] A. G. Besoli and F. D. Flaviis, "A Multifunctional Reconfigurable Pixeled Antenna Using MEMS Technology on Printed Circuit Board," IEEE Trasn. on Ant. And Propag., Vol. 59 (No. 12), p. p. 4413-4424, 2011.
[76] M. K. Fries, M. Grani and R. Vahldieck, "A Reconfigurable Slot Antenna with Switchable Polarization, " Mic. and Wireless Componenfs Lett., Vol. 13 (No. Il), p. p. 490-492, 2003.
[77] S. Lim and H. Ling, "Design of Electrically Small, Pattern Reconfigurable Yagi Antenna," Elec. Lett., Vol. 43 (No. 24), p. p. 1326-1327,2007.
[78] W. Sung-Jung and M. Tzyh-Ghuang, "A Wideband Slotted Bow-Tie Antenna With Reconfigurable CPW-to-Slotline Transition for Pattern Diversity," IEEE Trasn. On Ant. and Propag., Vol. 56 (No. 2), p. p. 327-334,2008.
[79] J. T. Bernhard, "Reconfigurable Antennas," Morgan & Claypool publications series, 2007.
[80] J. T. Bernhard, "Reconfigurable Multifunction Antennas: Next Steps fot the Future," in Inf. Sym. on Mic., Anf., Propag. and EMC Tech. for Wireless Comm., 2007.
[81] L. N. Pringle, P. H. Harms, S. P. Blalock, G. N. Kiesel, et al., "A Reconfigurable Aperture Antenna Based on Switched Links Between Electrically Small Metallic Patches," IEEE Trasn. on Ant. and Propag., Vol. 52 (No. 6), p. p. 1434-1445,2004.
[82] H. Chen, B.-I. Wu, L. Ran, T. M. Grzegorczyk, J. A. Kong, "Controllable left-handed metamaterial and its application to a steerable antenna," Applied physics letters, Vol. 89, 053509, 2006.
[83] G. H. Huff and J. T. Bernhard, "Integration of Packaged RF MEMS Switches with Radiation Pattern Reconfigurable Square Spiral Microstrip Antennas," IEEE Trasn. on Ant. and Propag., Vol. 54 (No. 2), p. p. 464-469,2006.
[84] W. Kim, M. F. Iskander and W. D. Palmer, "An Integrated Phased Array Antenna Design Using Ferroelectric Materials and the Continuous Transverse Stub Technology," IEEE Trasn. on Ant. and Propag., Vol. 54 (No. Il), p. p. 3095-3105, 2006.
[85] J. Taeksoo, H. Yoon, J. K. Abraham and V. K. Varadan, "Ku-Band Antenna Array Feed Distribution Network with Ferroelectric Phase Shifters on Silicon," IEEE Trasn. on Mic. The. and Tech., Vol. 54 (No. 3), p. p. 1131-1138,2006.
[86] S. L. Preston, D. V. Thiel, J. W. Lu, S. G. O'Keefe and T. S. Bird, "Electronic Bearn Steering Using Switched Parasitic Patch Elements," Elec. Lett., Vol. 33 (No. 1), p. p. 7-8, 1997.
[87] R. Schlub, D. V. Thiel, J. W. Lu and S. W. O'Keefe, "Dual-Band Six-Element Switched Parasitic Array for Smart Antenna Cellular Communications Systems," Elec. LeU., Vol. 36 (No. 16), p. p. 1342-1343,2000.
[88] B. Schaer, K. Rambabu, J. Bornemann and R. Vahldieck, "Design of Reactive Parasitic Elements in Electronic Bearn Steering Arrays," IEEE Trans. on Ant. And Propag., Vol. 53 (No. 6), p. p. 1998-2003,2005.

[89] R. Jakoby, P. Scheele, S. Muller and C. Weil, “Nonlinear Dielectrics for Tunable Microwave Components,” in 15th Int. Conf. on Mic., Radar and Wireless Comm., 2004.
[90] J. B. Mills, C. J. Stevens and D. J. Edwards, “Composite Materials for Planar Frequency Agile Microwave Devices,” in 16th IEEE High Freq. Postgraduate Student Colloquium, 2001.
[91] D.-E. Yang, S.-T. Wu, “Fundamentals of Liquid Crystal Devices,” Wiley, Chichester, 2006).
[92] F. Goelden, “Liquid Crystal Based Microwave Components with Fast Response Times: Material, Technology, Power Handling Capability,” PhD thesis, Technische Universitaet Darmstadt, 2009.
[93] P.G. de Genne, J. Prost,“The Physics of Liquid Crystals,” Oxford Science Publications, Oxford, 1993)
[94] P.J. Collings,M.Hird, “Introduction to Liquid Crystals: Chemistry and Physics ,” Taylor and Francis Ltd., London, 1997)
[95] G. M. Rebeiz and J. B. Muldavin, “RF MEMS Switches and Switch Circuits,” IEEE Mic. Mag., Vol. 2 (No. 4), p. p. 59-71,2001.
[96] N. Kingsley, G. E. Ponchak and J. Papapolymerou, “Reconfigurable RF MEMS Phased Array Antenna Integrated Within a Liquid Crystal Polymer (LCP) Systemon- Package, ” IEEE Trans. on Ant. and Propag., Vol. 56 (No. 1), p. p. 108-118, 2008.
[97] R. Kumar and D. Bora, “A Reconfigurable Plasma Antenna,” Jour. of App. Phy.,Vol. 107 (No. 5), p. p. 53303-53312,2010.
[98] R. R. Romanofsky, “Advances in Scanning Reflect array Antennas Based on Ferroelectric Thin-Film Phase Shifters for Deep-Space Communications, ” IEEE Proceedings, Vol. 95 (No. 10), p. p. 1968-1975,2007.
[99] G. Lubkowski, B. Bandlow, R. Schuhmann, and T. Weiland, “Effective modeling of double negative metamaterial macrostructures,” IEEE Trans. Microw. Theory Tech. 57, 1136–1146 (2009).
[100] F. Bilotti and L. Sevgi, “Metamaterials: definitions, properties, applications, and FDTD-based modeling and simulation (invited paper),” Int. J. RF Microw. CAE 22, 422–438 (2012).
[101] C. A. Balanis, “Advanced Engineering Electromagnetics,” Wiley, 1989.
[102] F. Bilotti and L. Sevgi, “Metamaterials: definitions, properties, applications, and FDTD-based modeling and simulation (invited paper),” Int. J. RF Microw. CAE 22, 422–438 (2012).
[103] C. A. Balanis, Advanced Engineering Electromagnetics second edition (Wiley,2012).
[104] S.M. Chaker M. Bouzouad “Metamaterial patch antenna radiation pattern agility” ApplPhys ADOI 10.1007/s00339-013-8037-0 (5 October 2013)
[105] S.M. Chaker, D.Bensafieddine, E. M. Laamari, and M. Bouzouad, “A Zero –Index Metamaterial Superstrate for Patch Antenna Gain Enhancement,” The 3rd Advanced Electromagnetics Symposium, AES 2014 Hangzhou - China.